On the Taylor column driven motion of a buoyant sphere in a free-surface vortex core

Christian van Nieuwenhuizen

On the Taylor column driven motion of a buoyant sphere in a free-surface vortex core

by

C. van Nieuwenhuizen

Department of Hydraulic Engineering
Section: Environmental Fluid Mechanics

In partial fulfilment of the requirements for the degree of

Master of Science
in Civil Engineering

at the Delft University of Technology,
to be defended publicly on 17-03-2022

Thesis Committee members:

Committee chair:	Dr. Ir. B. Hofland	TU Delft (Coastal Structures)
Committee member:	Prof. Dr. Ir. W.S.J. Uijttewaal	TU Delft (Environmental Fluid Mech.)
Daily supervisor:	Ir. W. Bakker	Deltares (Hydraulic Eng.)
Advisor:	Prof. Dr. Ir. F.H.L.R. Clemens	Deltares (Hydraulic Eng.) / TU Delft
External advisor:	Dr. Ir. S.P.A. Duinmeijer	Eng. Dept. of Municipality of Rotterdam

TU Delft

Front cover page shows a buoyant sphere being transported down a free-surface vortex core

CONTENTS

SUMMARY

The added drag on a buoyant body traveling in a solid-body rotation flow has been rigorously studied over the last century with G.I. Taylor being the first one to describe it in 1922, a hundred years ago. A recent publication by Duinmeijer (2021) investigated the capacity of free-surface vortices to transport solids as a practical application to avoid solids accumulation in wastewater pump sumps. In that research, the assumption was made that a Taylor column exists upstream and downstream of the solids body, aiding the downward motion in the vortex core. This has however never been experimentally confirmed for free-surface vortex flows. The goal of this research is to experimentally check whether or not the Taylor-column induced drag force is the main mechanism for the downward motion of buoyant particles in a free surface vortex core. An experimental set-up consisting of a 600 x 1000mm (diameter x height) Perspex tank is used, in which controlled vortices can be generated. A novel combination of Laser Doppler Velocimetry (LDV) and Particle Tracking Velocimetry (PTV) is deployed simultaneously to obtain synchronised data of both the flow velocities and particle motion. The LDV device measures the tangential and axial flow components in a small measurement volume. Many point-measurements along a horizontal line through the vortex enable us to create the tangential and axial velocity profiles. A deconvolution process is applied on the LDV data to account for the spatial averaging effect of the LDV measurement volume and the wandering of the vortex core. The PTV system is used to determine the particle location over time, from which the velocity is obtained. For simplicity, only one type of particle - a buoyant sphere of 25 mm in diameter - is considered in this study. To obtain repeatability of the experiments, a particle dropping device is introduced to insert the sphere in the vortex core without entrapping air. A PID control system is added to the set-up to keep the discharge through the system constant.

The first part of this research focusses on the performance of the measurement system, where the measurements of the flow characteristics of the free-surface vortex in the absence of a buoyant particle are compared to the results obtained by Duinmeijer (2020), repeating one of the experiments from that thesis without a buoyant particle. The tangential velocities measured with LDV, coincide well with the tangential velocity profiles found during PIV measurements by Duinmeijer. The axial velocity profiles however do not agree. Duinmeijer measured maximum axial velocities around the vortex core radius where in this thesis an axial velocity profile with two maxima is found; one in the vortex centre and one at 60-70% of the vortex core radius. Several additional experiments were performed to rule out possible causes for this difference, from which it is concluded that the axial velocity is non-zero in the vortex centre.

The second part of the thesis focusses on the characteristics of the flow in the vortex core in the presence of a buoyant sphere. With the synchronized deployment of the LDV and PTV-system, the flow mechanics and the motion of the buoyant sphere can be simultaneously characterized. Such that the influence of the sphere's presence on the tangential and axial velocity components is quantified. New findings were obtained from these measurements, with the most striking one being a significant difference that is observed in the tangential velocities of the flow just above and below the buoyant sphere. Although this effect is described in theory e.g. by Moore and Saffman and Maxworthy (1970; 1968), it has not been measured before in any lab experiment before and therefore it was not expected to be observed so clearly during the experiments. The clear tangential velocity discrepancy experimentally confirms the presence of the Taylor column above and below the sphere.

The last part of the thesis is dedicated to quantifying the Taylor column induced drag force, derived from the tangential velocity difference of the flow above and below the particle. This difference in tangential velocities induces a pressure difference over the particle leading to a downward pointing force. The magnitude of this force is shown to be 75±17% of the total drag on the particle, making the Taylor column induced drag the main downward transport mechanism for the buoyant sphere in the free-surface vortex core given the conditions used in this experimental set-up.

It is recommended to investigate further the effect of the vortex core radius/particle characteristic length ratio on the Taylor column induced drag. The axial free-surface vortex flow is not radially uniform, with a region of high axial flow around the core radius. This axial flow being pushed into a Ekman layer on the sphere surface is generating the pressure difference over the particle and thus the downward force. It is therefore suspected that vortex core/particle size ratio strongly influences the Taylor column induced drag magnitude and thus be researched further.

LIST OF SYMBOLS

Symbol	Unit	Description
A_p	m^2	Particle cross-sectional area
A	mV	Constant for potentiometer calibration
a	s^{-1}	Vortex stretching parameter
C_D	-	Drag coefficient
c_i	m	Radial scale for Gaussian fit
d_m	m	LDV measurement volume diameter
D_i	m	Vortex tank water inlet diameter
D_o	m	Vortex tank water outlet diameter
E_k	-	Ekman number
F_B	N	Buoyancy force
F_D	N	Drag force
f	Hz	Frequency
g	ms^{-2}	Gravitational acceleration
l_m	m	LDV measurement volume length
l_0	m	Integral length scale
N	-	Dimensionless parameter, ratio of Coriolis over inertia
N_ε	-	Idem, but in relation to the rotation of the solid body
P	Pa	Pressure
Q	m^3s^{-1}	Total discharge through vortex tank
R	-	Correlation coefficient
R_o	-	Rossby number
r	m	Radial location
r_b	m	LDV beam radius
r_p	m	Particle radius
T_a	-	Taylor number, ratio between Coriolis and viscous forces
U_r	ms^{-1}	Radial particle velocity
U_z	ms^{-1}	Vertical particle velocity
U_{pot}	mV	Potentiometer output voltage
V_0	ms^{-1}	Integral velocity scale (turbulence characteristic)
V_θ	ms^{-1}	Tangential velocity
V_r	ms^{-1}	Radial flow velocity
V_z	ms^{-1}	Axial flow velocity
x	m	Coordinate on x-axis
x_v	m	Deviation from LDV measurement volume centre (x-direction)
x_c	m	Core location deviation from time averaged centre location (x-direction)

y	m	Coordinate on y-axis
y_v	m	Deviation from LDV measurement volume centre (y-direction)
y_c	m	Core location deviation from time averaged centre location (y-direction)
z	m	Coordinate on z-axis
α	Rad	LDV angle between main and reference beam
β	Rad	LDV angle between velocity vector and bisector
Γ	$m^2 s^{-2}$	Flow circulation
ρ_f	$kg\ m^{-3}$	Fluid density
ρ_p	$kg\ m^{-3}$	Particle density
R	s	Correlation time shift
θ_1	Rad	LDV angle between main beam and velocity vector
θ_2	Rad	LDV angle between reference beam and velocity vector
Ω	$Rad\ s^{-1}$	Angular flow velocity
Ω_ε	$Rad\ s^{-1}$	Angular flow velocity perturbation
ω	s^{-1}	Vorticity
χ	m^3	Experimental particle volume

LIST OF ABBREVIATIONS

Abbreviation	**Description**
ADC	Analog to Digital Converter
DRB	Double Reference Beam (LDV)
EOM	Equation of Motion
EP	Experimental Particle
HSV	Hue Saturation Value
LDV	Laser Doppler Velocimetry
PID	Proportionality Integral Derivative control
PIV	Particle Imaging Velocimetry
PLA	Poly Lactose Acid
UV	Ultra Violet

1 INTRODUCTION

Abundant research is available on the topic of free-surface vortices and their dynamics. Most of this research is focussed on how to supress these vortices. Controlled free-surface vortices can however also prove useful as they can transport buoyant, solid particles of varying sizes, e.g. (Voßwinkel, 2017). Previous experimental studies performed by Duinmeijer (2021) looked at the ability of free-surface vortices to transport floating debris in pump sumps towards the pump intake to avoid accumulation of debris in the pump sump basin. In that thesis, an experimental set-up was used to induce a controlled vortex. Particles of various densities, shapes and sizes were introduced and entrained in the vortex. By the means of Particle Tracking Velocimetry (PTV), the motion of these particles in the vortex was determined. Also, Particle Imaging Velocimetry (PIV) was applied to obtain velocity profiles in a horizontal plane through the vortex.

During the previous study by Duinmeijer (2021), the process of downward motion of buoyant particles in the vortex core, the so-called stage two transport (see Figure 1) was studied in some detail. The drag on the particle was calculated using axial (vertical) velocities measured by PIV experiments. It was found that the downward facing drag force based on these axial velocities is of an order of magnitude smaller than the upward facing buoyant force. As the flow in the vortex core is highly rotational, it is expected that a so-called Taylor-Proudman column (Taylor, 1922) exists which prevents the particle from rising. To account for this effect, Duinmeijer used a modified drag coefficient in the calculation of the stage-two downward transport of the buoyant particles to obtain a closed solution. As it could reasonably be expected that the presence of a particle in the vortex centre alters the vortex core flow field, it is not entirely correct to use the undisturbed velocities to calculate the drag force. To the authors knowledge, there is no experimental data available on the axial and tangential velocity profiles in the presence of a particle.

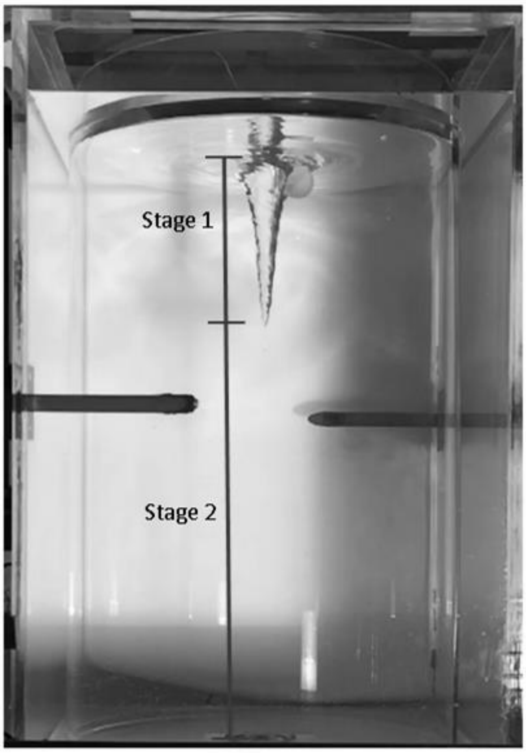

Figure 1 - Definition of the two stages of solids' transport in a free-surface vortex. Stage one comprises the helical motion of the particle down the vortex funnel to the tip of the air core. Stage two transport is the submerged transport of the particle down the vortex core to the outlet.

1.1 PROBLEM DEFINITION

In a previous study on the behaviour of buoyant particles in a free-surface vortex flow (Duinmeijer & Clemens, 2021), the assumption was made that a Taylor-Proudman column causes additional drag on the buoyant particle and is thus mainly responsible for its downward transport. The main problem is the knowledge gap on the flow structure in the presence of a solid particle inside the free-surface vortex core and the lack of simultaneous data of both the motion of the particle and the fluid. Moreover, literature can be found on the drag of solid bodies in a rotational fluid, e.g. (Maxworthy, 1970; Moore & Saffman, 1968, 1969). However, to the author's knowledge, apart from the thesis of Duinmeijer (2020), no literature exists on the drag on a body in a partly rotational/irrotational flow, which a vortex core consists of. Furthermore, as very little experimental data exists on the axial velocity profile in a free-surface vortex with an unsubmerged air core (the air core does not extend to the outlet), detailed measurements of this profile are of great importance to resolve the drag on a buoyant particle.

1.2 RESEARCH OBJECTIVE

Experimental research will be performed to obtain data and verify the presence of a Taylor Proudman column extending above and below a buoyant particle in the free-surface vortex core. An attempt will be made to obtain synchronized data of the flow velocities and the axial particle motion to obtain velocity profiles in the presence of a particle in the vortex centre. A technique that is proposed to measure the flow velocities is Laser Doppler Velocimetry (LDV) as it can precisely measure 2D velocity vectors at high acquisition rates. An improved PTV setup is applied, with which the particle location and its rotation is measured. The research objective can be expressed in the following main and sub-questions:

Does a Taylor-Proudman column contribute to the downward transport of buoyant particles in a free-surface vortex?

> *How are the axial and tangential flow profiles distributed within the vortex core in absence of a solid particle?*
>
> *How are the axial and tangential flow profiles distributed within the vortex core in presence of a solid particle?*
>
> *How do the altered velocity profiles contribute to the drag force on the buoyant particles?*

1.3 RESEARCH STRUCTURE

The required theoretical framework applied is presented in chapter 2. Chapter 3 discusses and explains the (experimental) techniques and methods that were implemented. Chapter 4 gives an overview of the experimental program. The results are presented in chapter 5. Chapter 6 is dedicated to the discussion of the results and the conclusions are presented in chapter 7. Recommendations are given in chapter 8.

2 THEORETICAL FRAMEWORK

2.1 FREE-SURFACE VORTEX FLOW

A free-surface vortex, maybe better known as a 'bathtub vortex' is a vortex that develops when water drains out of a container, for example draining a bathtub. The flow is characterized by a zone of high vorticity, ω (s^{-1}) and thus circulation Γ (m^2s^{-1}) around the axis of the rotation, known as the vortex core characterized by the core radius r_c (m). Outside the vortex core, the flow is found to be irrotational (i.e. $\omega = 0$). It is convenient to describe a free-surface vortex in polar coordinates with r being the radius from the vortex centre, z the vertical coordinate parallel with the vortex axis of rotation and θ the angle in radians.

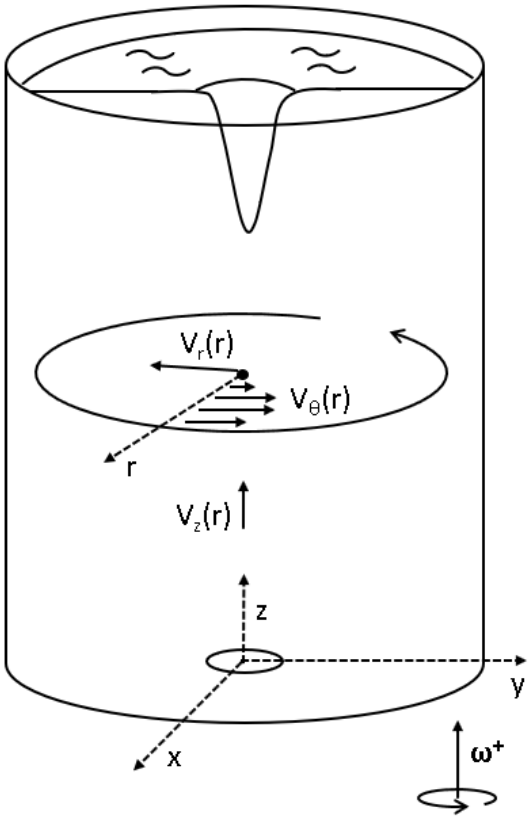

Figure 2 - Reference frame of the free-surface vortex.

2.2 BURGERS FREE-SURFACE VORTEX MODEL

The free-surface vortex can be described by a mathematical model first proposed by Rankine (1921). Rankine's model divides the vortex flow in two parts, a solid-bodied rotating vortex core within an irrotational outer flow field:

$$V_\theta = \frac{\Gamma}{2\pi}\frac{r}{r_c^{\,2}} = \Omega r \quad (r < r_c) \tag{2.1}$$

$$V_\theta = \frac{\Gamma}{2\pi} \quad (r \geq r_c) \tag{2.2}$$

In which V_θ is the tangential velocity in m/s, also known as the 'swirl velocity' and Ω is the angular velocity in rad/s. From the above equations it is clear that a discontinuity exists in the tangential velocity profile of Rankine's model at the core radius ($r = r_c$). Note that this is physically impossible as it implies an infinite gradient of the velocity.

Burgers (Burgers, 1948) proposed a new model with conservation of vorticity at its basis:

$$\frac{D\boldsymbol{\omega}}{Dt} = (\boldsymbol{\omega}\cdot\nabla)\mathbf{V} + \nu\nabla^2\boldsymbol{\omega} \tag{2.3}$$

In which ν is the kinematic viscosity (m^2/s), . $\boldsymbol{\omega} = \left[\omega_x, \omega_y, \omega_z\right]$. is the vorticity vector and $\mathbf{V} = \left[V_x, V_y, V_z\right]$ the fluid velocity vector. As the flow is assumed to be symmetric around the axis of rotation, all terms but the vorticity in the z-direction can be excluded. Furthermore, Burgers assumes a stationary situation, thus time dependent terms can be eliminated as well. This leads to the following vorticity balance:

$$V_r\frac{\partial\omega_z}{\partial r} = \omega_z\frac{\partial V_z}{\partial z} + \nu\frac{1}{r}\frac{\partial}{\partial r}\left(r\frac{\partial\omega_z}{\partial r}\right) \tag{2.4}$$

This equation is an elegant example of the balance between the radial, inward convection of vorticity (left hand side of the equation) with vortex stretching (first term on right-hand side) and viscous diffusion (second term, right-hand side). Simply put, a radial inward flow concentrates vorticity to the vortex core. Conservation of mass implies that the axial velocity must increase in downward direction, leading to vortex stretching causing an even further concentration of vorticity around the core. As vorticity and velocities cannot infinitely increase as they concentrate towards the vortex core, viscous diffusion starts to play an increasing role towards the rotation centre to balance the increase of vorticity. The following axial and radial velocity profiles were proposed by Burgers to solve the equation (2.4):

$$V_z = 2az \tag{2.5}$$

$$V_r = -ar \tag{2.6}$$

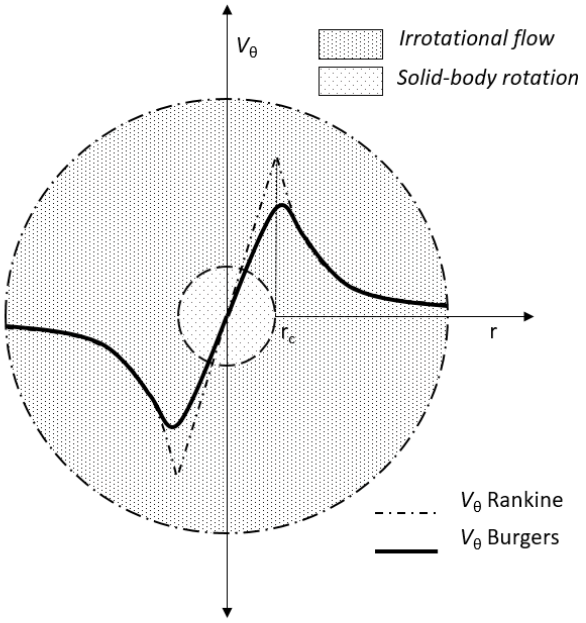

Figure 3 - Distribution of the tangential velocity according to Rankine and Burgers models.

These profiles result from conservation of mass, where $a = \partial V_z / \partial z$, the vortex stretching parameter. Using these profiles, equation (2.4) can be rewritten as:

$$\frac{\partial \omega_z}{\partial r} = -\left(\frac{a}{2\nu}\right) r\omega_z \tag{2.7}$$

Integrating this equation over *r* leads to the vorticity as a function of radial position:

$$\omega_z(r) = \omega_0 \exp\left[-\left(\frac{r}{r_c}\right)^2\right] \tag{2.8}$$

In which $\omega_0 = \Gamma_\infty / \pi r_c^2$ and $r_c = 2\sqrt{\frac{a}{\upsilon}}$

When Stokes' theorem (curl theorem) stating that "the line integral of a vector field over a closed curve is equal to the flux of its curl through the enclosed surface" is applied on equation , one finds the Burgers' tangential velocity profile:

$$V_\theta = \frac{\Gamma_\infty}{2\pi r}\left\{1 - \exp\left[-\left(\frac{r}{r_c}\right)^2\right]\right\} \tag{2.9}$$

2.3 VORTEX-DRIVEN VERTICAL TRANSPORT

2.3.1 Equations of motion

The vortex transport of solids can be split up in two stages that were defined by Duinmeijer (2021):

Stage one

In this stage, the buoyant particle travels from the water surface in a helical path until it centralizes in the tip of the air core, see Figure 4. Not all arbitrary buoyant particles can be transported in this stage, as it depends on their shape, mass and volume. Actually, the dynamics prove to be chaotic under certain conditions (Duinmeijer et al., 2020). Because of this chaotic nature, we have to resort to statistical description such that stage one transport can be determined for engineering applications (Voßwinkel, 2017). For a more detailed description of the transport criteria in this stage, the reader is referred to the thesis of Duinmeijer (2020) as further investigation of the stage one transport is not in the scope of this research.

Stage two

Stage two transport is the transport from the tip of the air core to the bottom. This transport mode is the topic of this thesis. In stage one, many forces act on the particle as the motion shows strong asymmetry, making a description of the motion complicated. In the second stage, forces like the lift force become less significant as the particle is centred in the middle of the vortex and these forces will therefore be symmetric and result in a net zero force (Duinmeijer & Clemens, 2021). In equation (2.10) the simplified equation of motion (EOM) for the particle in the z-direction is given, for a frame of reference moving with the particle.

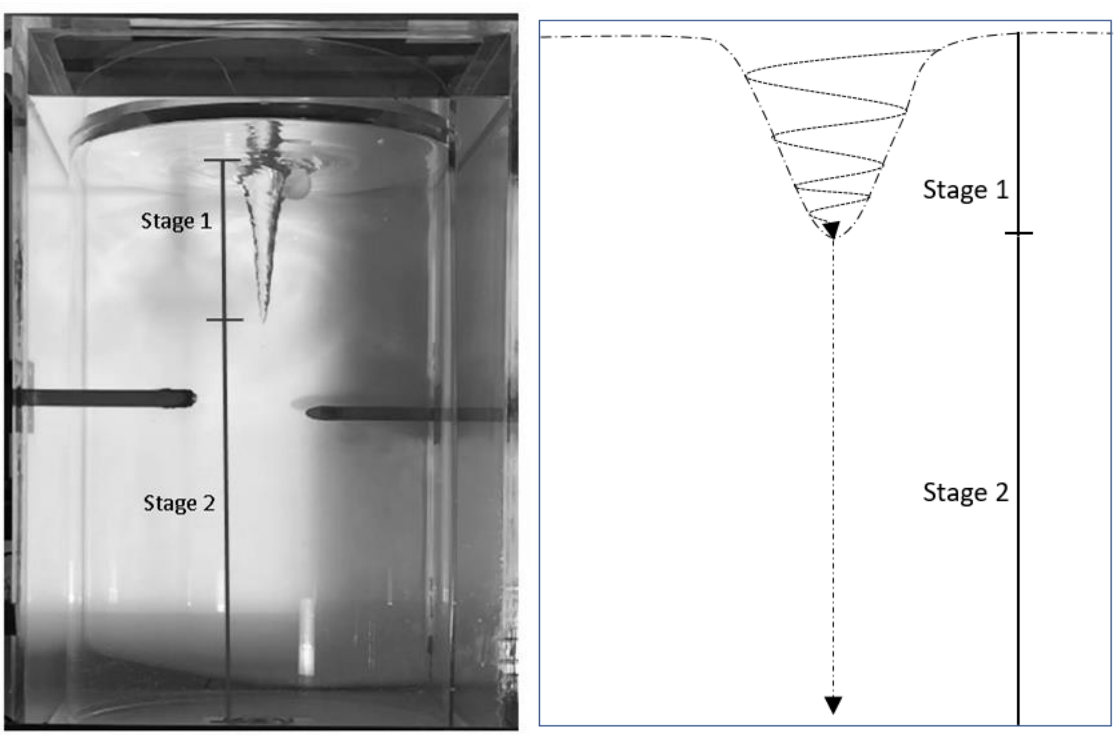

Figure 4 - Definition of stage one and stage two transport

$$\rho_p \chi \frac{\partial U_z}{\partial t} = F_B + F_D + F_{A,M} \tag{2.10}$$

In which U_z is the vertical component of the particle velocity in m/s and χ is the particle volume in m^3. The left-hand side of the equation represents inertia of the particle and the terms on the right-hand side are the external forces that act on the particle. The first term on the right-hand side is the buoyant force, the second term the drag force and the last term is the force induced by fluid accelerations which is defined as:

$$F_{A,M} = C_A \rho_f \chi \left(\frac{DV_z}{Dt} - \frac{\partial U_z}{\partial t} \right) \tag{2.11}$$

Where:

$$\frac{DV_z}{Dt} = \frac{\partial V_z}{\partial t} + V_r \frac{\partial V_z}{\partial r} + \frac{V_\theta}{r} \frac{\partial V_z}{\partial \theta} + V_z \frac{\partial V_z}{\partial z} \tag{2.12}$$

And C_A is the added mass coefficient and V_z is the vertical component of the water velocity in m/s.

$$\begin{aligned} &\left(\rho_p + C_A \rho_f \right) \chi \left(\frac{\partial U_z}{\partial t} + U_z \frac{\partial U_z}{\partial z} + U_r \frac{\partial U_z}{\partial r} + \frac{U_\theta}{r} \frac{\partial U_z}{\partial \theta} \right) = \\ &\rho_f C_A \chi \left(\frac{\partial V_z}{\partial t} + V_z \frac{\partial V_z}{\partial z} + V_r \frac{\partial V_z}{\partial r} + \frac{V_\theta}{r} \frac{\partial V_z}{\partial \theta} \right) + F_D + F_B \end{aligned} \tag{2.13}$$

We assume that the vertical flow is stationary ($\partial V_z / \partial t = 0$) and axisymmetric ($\partial V_z / \partial \theta = 0$). We can then reduce the EOM to the following expression:

$$\left(\rho_p + C_A \rho_f \right) \chi \frac{\partial U_z}{\partial t} = F_D + F_B + \rho_f C_A \chi \left(V_r \frac{\partial V_z}{\partial r} + V_z \frac{\partial V_z}{\partial z} \right) \tag{2.14}$$

The inertial forces are very small compared to the buoyant and drag forces. This was confirmed by a calculation using some characteristic experimentally obtained values. Effectively, at the onset of motion, there is a balance between the drag and the buoyant forces with the buoyant force defined as:

$$F_B = (\rho_f - \rho_p) g \chi \tag{2.15}$$

2.3.2 Taylor-Proudman theorem and Taylor column

For highly rotating flows, the conventional drag formulae seems not applicable as experimentally confirmed by Taylor (1922). When the fluid is highly rotational, this leads to high Taylor numbers (analogous to low Ekman numbers) meaning that the Coriolis forces, represented by the solid body rotation Ω dominate viscous forces characterised by the kinematic viscosity ν :

$$T_a = \frac{\Omega r_p^{\ 2}}{\nu} = E_k^{\ -1} \gg 1 \tag{2.16}$$

Here, r_p is the particle radius. Moreover, the high particle rotation in relation the vertical particle velocity U_z leads to a low Rossby number, meaning that the inertial forces are negligible compared to the Coriolis forces:

$$R_o = \frac{U_z}{\Omega r_p} = \frac{2}{N} \ll 1 \tag{2.17}$$

In some studies, the parameter N is used instead of the Rossby number and is also defined in equation (2.17). The above conditions together with the assumption of a hydrostatic pressure distribution and an incompressible fluid gives us the Taylor-Proudman theorem (when the curl is taken of the simplified Navier-Stokes equations) (Taylor, 1922):

$$\Omega_x \frac{\partial \mathbf{V}}{\partial x} + \Omega_y \frac{\partial \mathbf{V}}{\partial y} + \Omega_z \frac{\partial \mathbf{V}}{\partial z} = 0 \tag{2.18}$$

When there is only rotation in the vertical direction ($\Omega_x = \Omega_y = 0, \Omega_z \neq 0$) this leads to:

$$\frac{\partial \mathbf{V}}{\partial z} = 0 \tag{2.19}$$

Meaning that all velocity components are uniform along the vertical axis. When a particle is present in the vortex, cylinders of fluid are believed to exists *above and below* the particle extents where the flow is purely two-dimensional as we see from the Taylor theorem. This phenomenon is called a Taylor-Proudman column. It could be observed in the flow field by measuring identical velocity vectors (at the same radial position) at any vertical position in the water column above or below the particle.

2.3.3 Taylor column induced drag

The Taylor column is believed to be responsible for the increased drag on the particle (Maxworthy, 1970; Moore & Saffman, 1968). This theory has only been confirmed for buoyant particles in solid-body rotation flows in a closed container. Using the Taylor-Proudman theorem, the drag formula (2.14) can now be simplified to:

$$\left(\rho_p + C_A \rho_f\right) \chi \frac{\partial U_z}{\partial t} = F_D + F_B + \rho_f C_A \chi \left(V_r \frac{\partial V_z}{\partial r} \right) \tag{2.20}$$

As the axial flow bounded by the Taylor-Proudman column (it cannot radially diverge) encounters the rigid surface of the particle, it is pushed into a thin Ekman layer present on the particle surface (Moore & Saffman, 1968). As the flow diverges around the particle through the Ekman layer, it moves parallel in the plane of rotation and the Coriolis force deflects it in the direction opposing the rotation of the Taylor column. On the bottom of the particle, the reverse effect takes place, where the deflection of the streamlines increases the tangential velocities below the particle. As the tangential velocity above the particle decreases, a smaller radial pressure gradient is present. This can be seen from the geostrophic balance, which is the result of the simplified Navier-Stokes equations (applying the assumptions used for the Taylor theorem (Maxworthy, 1970)):

$$\frac{\partial \tilde{p}}{\partial r} = 2\Omega \rho \tilde{V}_\theta + \rho \frac{\tilde{V}_\theta \left| \tilde{V}_\theta \right|}{r} \tag{2.21}$$

Where $\tilde{p}$ is the modified pressure and $\tilde{V}_\theta$ is the disturbed tangential velocity relative to the undisturbed situation. As the presence of a Taylor column has only been confirmed for a solid-body rotation flow and not for a free-surface vortex, we must measure the disturbed tangential velocities above and below the particle to confirm the presence of a Taylor column for the case with a free-surface vortex flow. The geostrophic balance must then be rewritten as:

$$\frac{\partial \tilde{p}}{\partial r} = 2\Omega \rho \left(V_{\theta,top} - V_{\theta,bottom} \right) + \rho \frac{\left(V_{\theta,top} - V_{\theta,bottom} \right)\left(\left| V_{\theta,top} - V_{\theta,bottom} \right| \right)}{r} \tag{2.22}$$

As the pressure outside the Taylor-Proudman column is fixed, an *increase* of pressure is expected above the particle. The increased tangential velocity below the particle requires a higher radial pressure gradient and thus a *lower* pressure below the particle (Moore & Saffman, 1968). Both these pressure perturbations lead to a nett *downward* force on the particle:

$$F_{D,Taylor} = \int_0^{r_p} \tilde{p}(r) 2\pi r dr \qquad (2.23)$$

Figure 5 shows a graphical schematization to aid our intuition on the problem. Next to the Taylor column driven drag force, we also expect a skin friction induced drag on the particle and a stagnation pressure drag force. The total drag on the particle can be written as:

$$F_D = F_{D,Taylor} + F_{D,Skin} + F_{D,Stagnation} \qquad (2.24)$$

In this research, we make an attempt to measure the tangential and axial velocity profiles above and below the particle, so that we can actually determine the pressure perturbation and Taylor column induced drag on the particle as presented in equation (2.22), which to the authors knowledge has not been measured/published before.

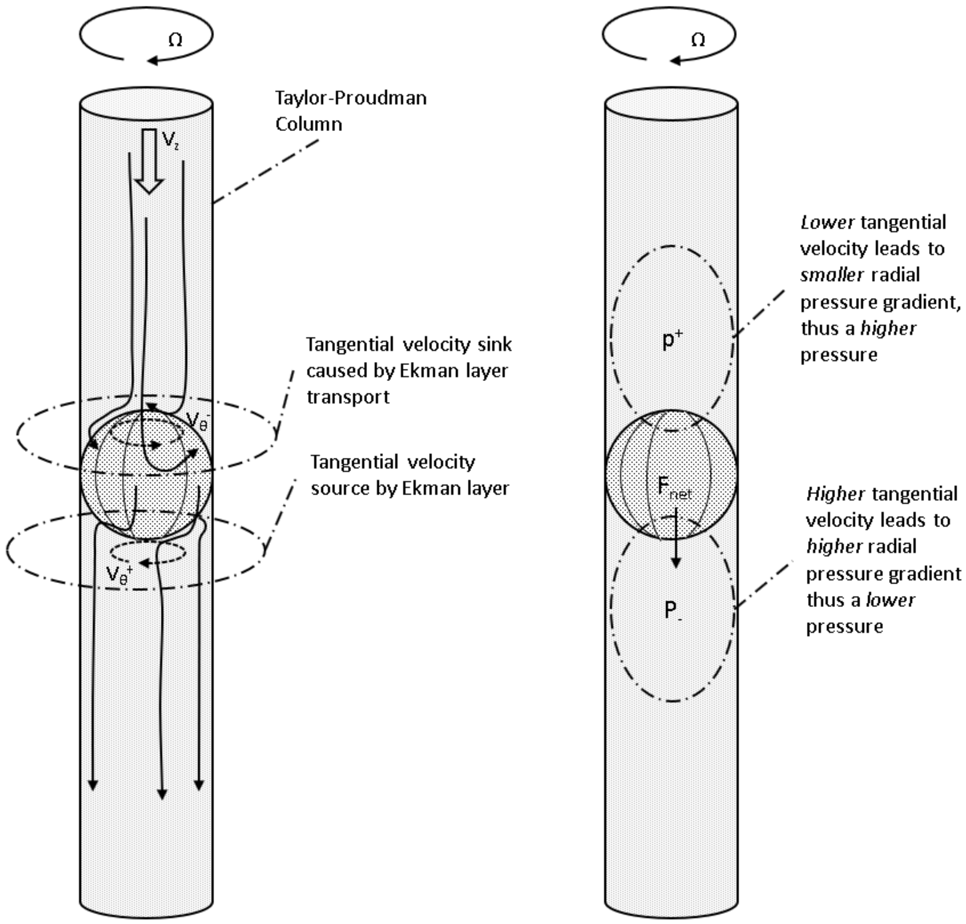

Figure 5 - Schematization of the mechanism, increasing the drag force on the particle.

2.4 DRAG FORCE FROM PREVIOUS RESEARCH

Several studies were already performed on the drag force on a particle in a rotating flow. A general format of presenting the drag force is via the bulk drag coefficient C_d which is often empirically determined:

$$F_D = \frac{1}{2}\pi C_d \rho_f \left(V_z - U_p\right)\left(\left|V_z - U_p\right|\right) r_p^{\ 2} \tag{2.25}$$

In the upcoming sections, three propositions from several authors are presented for this bulk drag coefficient in a rotating flow. The main difference with this thesis is that these authors all consider a solid-body rotation, where this is only partly representative for this study as part of the vortex core $\left(r < \tfrac{3}{4} r_c\right)$ consists of a solid-body rotating fluid and the rest of irrotational flow (see Figure 3). Thus when a particle radius is larger than the core radius, it extends into the irrotational regime. No literature is available on particle drag in vortex flow which is both rotational and irrotational. One should also note that the bulk drag coefficient is an empirical replacement for all the separate drag terms presented in equation (2.24).

2.4.1 Drag coefficient by Moore and Saffman I

Moore & Saffman (1968) made a mathematical model for the drag on an axisymmetric body rising through a rotating fluid in a container of finite length. They did this with a fully closed container and a container with a free surface. For the detailed derivation of this theoretical drag model, one refers to (Moore & Saffman, 1968). The final drag coefficient of a body in a rotating flow with a free surface is given by:

$$C_d = \frac{353}{315} \frac{\Omega^{1\frac{1}{2}} r_p^{\ 2}}{U_p \nu^{\frac{1}{2}}} - \frac{86}{210} \frac{\Omega_\varepsilon^2 r_p^{\ 2}}{U_p^2} \tag{2.26}$$

Note that Ω_ε on the right side of the equation represents the rotation relative to the general rotation Ω.

2.4.2 Drag coefficient by Moore and Saffman II

Later studies of Moore & Saffman (1969) showed that for an unbounded solid-body rotating fluid, for any arbitrary particle shape, provided its characteristic length is not of the same magnitude as r_p / E_k, the drag coefficient can be described by:

$$C_d = 5.33N \tag{2.27}$$

The definition of N can be found in equation (2.17). Note that this is for an unbounded flow, so no influence of top and bottom boundaries exists. The case of the vortex tank can also be partly described by unbounded flow, as the rotational character of the flow does not end at the bottom of the tank but extends further down the outlet. Unlike the previous drag coefficient, this drag coefficient is independent of viscosity.

2.4.3 Drag coefficient by Maxworthy

The two previously discussed drag conditions described above are based on mathematic approximations, Maxworthy (1970) conducted extensive experiments on the drag and shows a drag coefficient of approximately half that of Moore & Saffman (1969):

$$C_d = \left(2.60 \pm 0.05\right) N^{1 \pm 0.01} \tag{2.28}$$

Provided large N and T_a. Keeping in mind that this is value was determined with an enclosed volume, without free surface.

2.5 TURBULENCE

The Burgers vortex model, based on conservation of vorticity (equation (2.4)), describes an increase of vorticity towards the vortex centre. As it cannot grow infinite as the radius goes to zero, viscous dissipation starts to play an increasing role towards the centre, and this is where turbulence is created. Turbulence and vortex stretching are the processes that transfer kinetic energy from the large-scale flow to increasingly smaller scales where the energy is finally dissipated into heat by viscous diffusion. As the dissipation increases towards the core, more energy needs to be transferred to the smaller scales and it is expected that the turbulent energy, represented by energy containing eddies of a wide range of sizes, will also increase. It is relevant for our study to have an estimate on the magnitude of the turbulent energy allowing to make a distinction during our measurements between measurement noise and physical processes like the turbulent fluctuations.

Some of the benefits of LDV (Laser Doppler Velocimetry) measurements are the high sampling rate, relatively small measuring volume and the non-invasive nature of the method making it suitable to measure some turbulent properties of the flow.

For a full turbulent description, one should measure all three velocity components, which is often unfeasible. Instead of the full energy spectrum, one-dimensional energy spectra can be created. These spectra give information on the turbulent energy in a certain direction.

The first step is to apply the Reynolds decomposition to the measured time series, where a measured instantaneous velocity component is split up in an average and fluctuating part:

$$V(t) = \bar{V} + V'(t) \tag{2.29}$$

In which the time average of the series is defined as:

$$\bar{V} = \frac{1}{N_T}\sum_{i=1}^{N_T} V(t_i) \tag{2.30}$$

The variance of the dataset is then as follows:

$$\overline{V'^2} = \frac{1}{N_T - 1}\sum_{i=1}^{N_T}\left(V(t_i) - \bar{V}\right)^2 \tag{2.31}$$

When the assumption is made that the flow is statistically stationary, meaning that the turbulent statistics do not change (significantly) over time, the energy per length scale can be found, when the FFT (Fast Fourier Transformation) of the time correlation function of two velocity fluctuation signals:

$$S(\omega) = \frac{1}{2\pi}\int_{-\infty}^{\infty} e^{-i\omega t} R(\tau)\, d\tau \tag{2.32}$$

With the correlation function defined as:

$$R(\tau) = \overline{V'(t_1)V'(t_2)} = \overline{V'^2}\rho(\tau) \tag{2.33}$$

From the correlation function we can also find some properties of the larger scale turbulent structures. When the time shift is zero, the correlation should be 100%, $\rho(0) = 1$. And when the shift becomes larger, the correlation between the signals is slowly lost. The rate at which the correlation is lost tells us something about the time scale of the largest eddies. We thus need to find the period that it takes for the correlation to become zero: $\rho(\tau) \to 0\ for: \tau \to t_{end}$. In which t_{end} is the time when the correlation becomes negative. The integral time scale, T_0, is defined as:

$$T_0 = \int_0^{t_{end}} \rho(\tau) d\tau \tag{2.34}$$

The large eddies are of course also defined with an integral velocity scale and an integral length scale, respectively u_0 and l_0. The integral velocity scale is defined as the Root-Mean-Square (RMS) of the velocity fluctuations:

$$V_o = \sqrt{\overline{V'^2}} \tag{2.35}$$

The integral length scale is then the product of the velocity scale and the time scale:

$$l_0 = T_0 V_o \tag{2.36}$$

3 MATERIALS AND METHODS

For this research, several experimental techniques were applied to answer the research question. This chapter describes the experimental framework, the experimental set-up, the experimental flow measuring techniques and, finally, the motion tracking techniques.

3.1 EXPERIMENTAL SET-UP

The experimental set-up consists of a circular Perspex transparent tank with an inner diameter of 0.60 m and a height of 1 meter. The tank is enclosed by another square (0.7 x 0.7 x1.0 m) Perspex container and the space between the two containers is filled with water to compensate for too strong light refraction which otherwise would be causing a significant reduction of field of view when recording images. Water is circulated through the system by a 400-watt centrifugal pump. Water leaves the inner tank (referred to as the “vortex tank”) through an outlet in the centre of the bottom of the tank after which the water flows through a separation tank of 0.3 x 0.3 x 0.4 m where solid particles are separated out of the flow. From the separation tank, water flows through the pump, a flow meter and a control valve, back into the vortex tank through 2 horizontal Ø25.9 x 1.9 mm (outside Ø x wall-thickness) inlet pipes. A detailed drawing of the vortex tank can be found in Appendix A -Detailed drawing of experimental set-up.

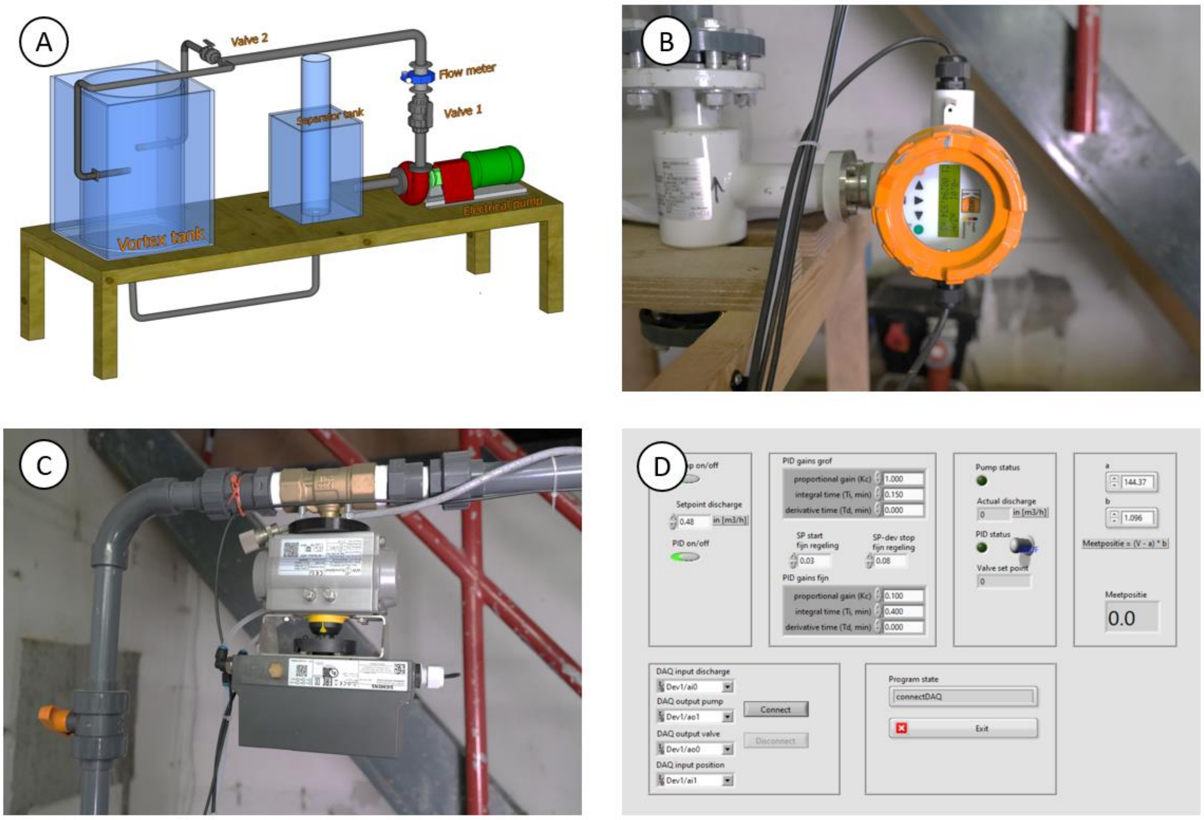

Figure 6 - Experimental set-up present at Deltares. (A) Overview of the experimental set-up. (B) Kobold flow meter. (C) Fast-acting pneumatically actuated ball valve. (D) Front panel of the system control interface.

The discharge through the system is controlled digitally by the means of a PID (Proportional Integral Derivative) control system designed in LabView®. The flowrate is measured with a magnetic-inductive flow meter (Kobold, DMH) which feeds the flow data to the PID controller, which corrects the flow rate (when necessary) by controlling a fast-acting pneumatically actuated ball valve. This setup enables us to maintain the desired discharge with a maximum deviation of ±5%.

The experimental particle is a 3D-printed sphere made of PLA (Poly Lactose Acid) with a 25mm diameter and a density of 0.766g/cm^3 and a measured particle volume of 8.402 cm^3.

The particle is inserted into the vortex tank centre by a remotely-operated device referred to as 'The ball dropper'. It consists of a vertical 3D-printed tube in which the experimental sphere is held in place by the means of a retractable pin actuated with a linear solenoid. When the solenoid is energized, it retracts the pin and the sphere drops in the centre of the vortex, where it stabilizes and gets transported downward. Figure 7 gives the overview of the several components of 'The Ball dropper'. The device aids the repeatability of the experiments but more importantly, it removes the air pocket often present underneath the sphere when it is inserted manually in the tank. The Ball dropper drops the sphere from just enough height to 'push' the air pocket out of the way as found by trial and error.

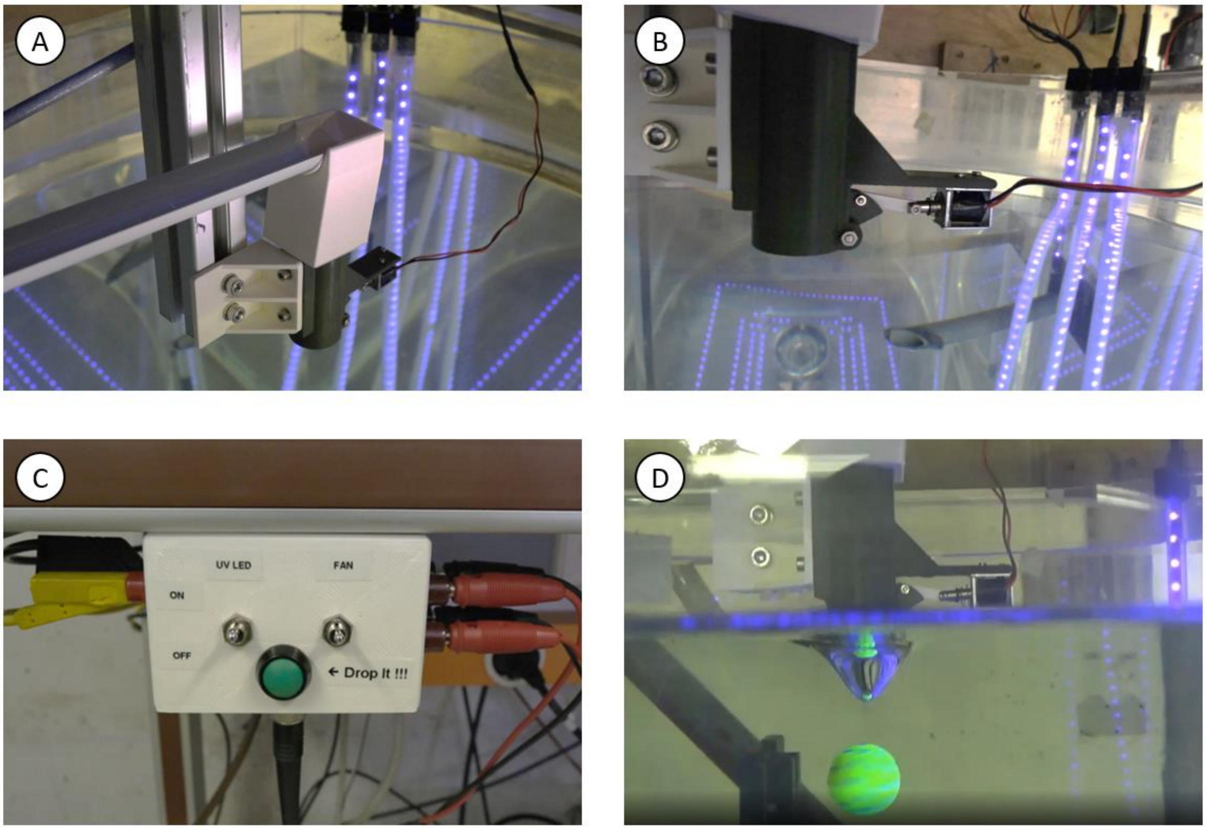

Figure 7 – The ball dropper device. (A) Sphere guide leading to the shaft. (B) Linear solenoid that retracts the locking pin from the shaft to drop the sphere. (C) Drop control box. (D) Snapshot after the sphere is just released.

The experimental particle used in the experiments is spray-painted with fluorescent paint and illuminated by UV light during the experiments to facilitate the post-processing of the camera footage. The particles are only emitting a narrow colour spectrum which can easily be filtered out of the complete frame with an HSV threshold filter, another reason for using a narrow spectrum is to avoid chromatic aberration.

The coordinate system used in this research is displayed in Figure 8. The position of the LDV and its measuring volume is coupled to the general coordinate system via a calibration, so that one knows where in the vortex tank the velocity components are measured. During this research, the LDV is normally traversed along the x-axis, however one experiment is conducted with the traversing direction along the y-axis. It should be noted that the *tangential* component is in that case no longer measured as one measures the *radial* component. The LDV technique is explained in detail in 3.2.

PTV post-processing software written by F.H.L.R. Clemens resolves the 3D position, rotation and rotation axis. By simply differentiating the position of the particle, its velocity can be resolved. The position of the particle is also referenced to the general coordinate system through the calibration of the cameras. The PTV system is explained in greater detail in section 3.3.

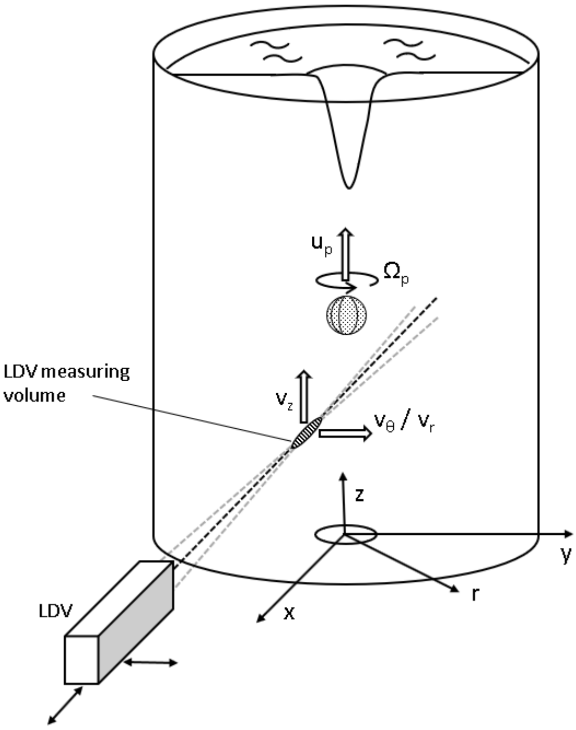

Figure 8 - Schematic of the coordinate system used. The centre of the outlet is defined as the origin. The LDV measurement volume position and particle location are linked to this coordinate system. The LDV is normally traversed over the x-axis and will then measure the tangential and axial velocity components. In one rare occasion, the LDV is traversed over the y-axis, it will then measure the radial and axial velocities.

3.2 EXPERIMENTAL TECHNIQUES FOR FLOW VELOCITY QUANTIFICATION

In order to *quantify* the flow structure in the vicinity of the buoyant particle in the vortex core, Laser Doppler Velocimetry (LDV) is used to determine the tangential and axial velocities and in one rare occasion, the radial velocity, see Figure 8.

3.2.1 Laser Doppler Velocimetry (LDV)

LDV is used to make velocity vector measurements through the vortex core. LDV is a point measurement technique which utilizes laser light to determine the direction and magnitude of the water flow. LDV is also very useful for quantifying turbulence levels due to its small spatial and temporal characteristics. The LDV is made available by Deltares.

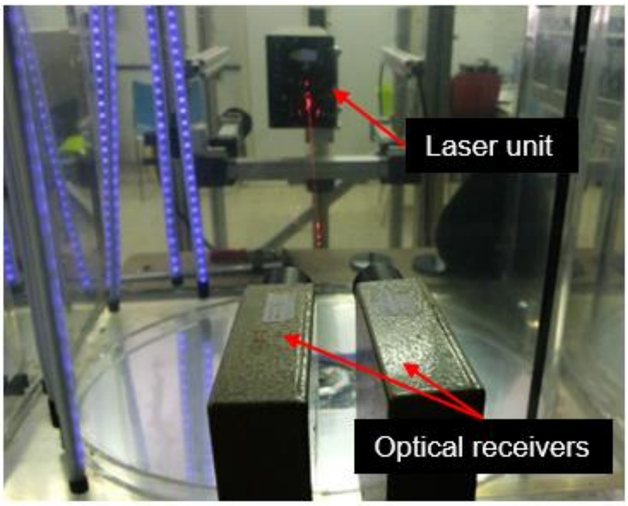

Figure 9 - LDV laser beams cross the vortex tank towards the optical receivers.

3.2.2 Basic working principle of LDV

LDV determines the velocity of *particles* suspended in the flow by measuring the doppler shift of light scattered by these particles.

The LDV used at Deltares is a Double-Reference Beam (DRB) LDV. This type of LDV is somewhat uncommon, where the (backscatter) differential beating doppler technique is more widely applied, as the signal to noise ratio of this type is better (Drain, 1980). Nonetheless, the DRB technique has other benefits like a significantly lower required power output of the laser, which makes this technique much safer to utilize (e.g., a Nortek backscatter LDV system utilizes two 5W lasers where the DRB LDV only utilizes a single 5mW laser).

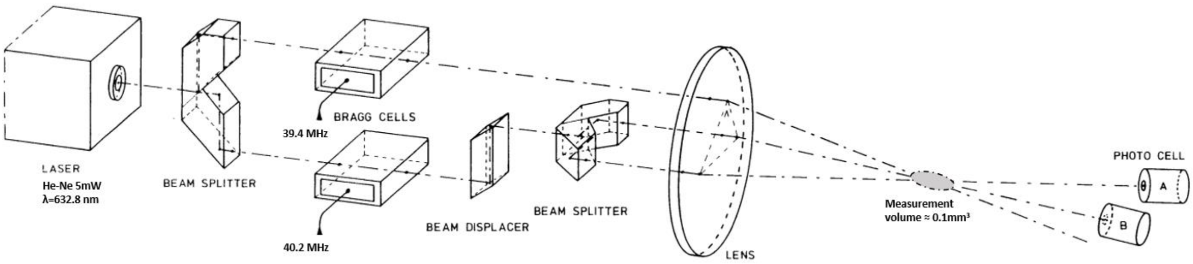

Figure 10 - Schematic of DRB LDV system.

The DRB LDV system consists of a 5mW (optical power) Helium-Neon laser with a constant wavelength of 632.8 nm (red light). Directly after the laser, the laser beam is split into two beams - the main beam and a reference beam. The main beam maintains 80% of the intensity and the reference beam 20%. Furthermore, both beams are directed through two Bragg cells. These are acoustic optical modulation devices, which use HF sound waves to shift the frequency of the light passing through them. For further reading on Bragg cells, the reader is referred to Drain (1980) or Durst (1976). The frequency of the main beam is shifted with 38.4MHz and the frequency of the reference beam with 40.2MHz. The necessity of the frequency shift will become apparent later. After the Bragg cell, the reference beam is split into two beams of equal intensity (10% of the total power each). Together with the main beam, the reference beams are passed through the main lens, which focuses all beams to intersect in a single point: the measurement volume. This volume can be as small as 0.1 mm^3 for a properly aligned set-up. The reference beams are aimed at optical receivers, which measure light intensity. When a particle is suspended in the measurement volume, it will scatter light from the main beam in all directions, but mostly forwardly biased (Mie, 1908). A fraction of this scattered light will end up at the optical receivers. Here, the scattered light from the main beam interferes with the light from the reference beam. As the frequencies of both light beams are unequal, because of the frequency shift by the Bragg-cells, optical beating occurs. Where the frequency of light itself is too high to measure even with the most advanced technology (order of 10^{14} Hz), the optical beating can be measured. In Figure 11 this effect is graphically illustrated.

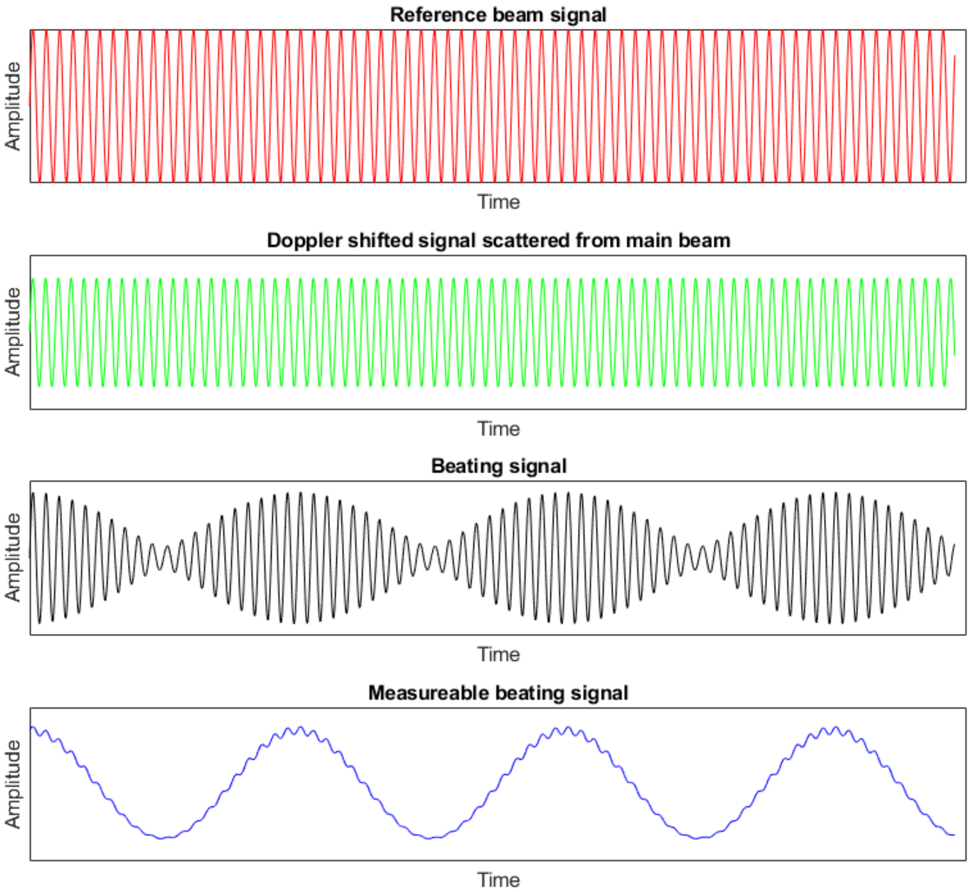

Figure 11 - Example of the frequency beating of two signals

This is the case for a stationary suspended particle that emits light with the same frequency as it receives. The beating frequency is then purely the difference in frequency between the two light bundles. This frequency shift was defined by the Bragg cell frequencies. The beating frequency is defined as:

$$f_{beating} = f_{reference} - f_{main} = 40MHz - 39.4MHz = 800KHz \tag{3.1}$$

Thus, when a frequency of 800Khz is observed at the photodetector, one can determine that the particle, and thus the flow, is stagnant.

In a flowing medium, a Doppler shift occurs on the frequency of the scattered light from the main beam. The Doppler shift is given by the following formula (Drain, 1980):

$$\Delta f = \frac{2V}{\lambda}\cos(\beta)\sin(\alpha) \tag{3.2}$$

In which Δf is the frequency change, V is the particle velocity, λ is the wavelength (fixed at 632.8 nm), α is the angle between the main beam and the observer Q. $\beta=(\theta_1 - \theta_2)/2$, this is the angle between the velocity vector and the bisector of the angle between SP and PQ (See also Figure 12). For the full derivation of (3.2) see (Drain, 1980, para. 3.4).

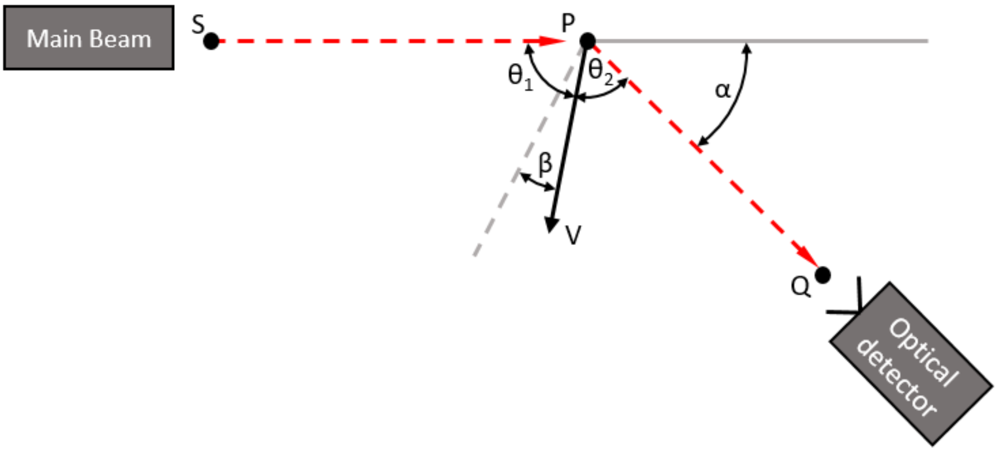

Figure 12 - Schematic of the reference beam LDV. The main beam is emitted from source S, scattering from a moving particle P with is moving with velocity V. The scattered light is observed in the optical detector Q.

Including the Doppler shift, the beating frequency is now given by:

$$f_{beating} = f_{reference} - \left(f_{main} - \Delta f \right) = 800 - \Delta f \, [KHz] \tag{3.3}$$

The optical receivers used in the Deltares DRB-LDV system have a working range of 600-1000 KHz. Depending on the direction of the motion of the particle, the doppler shift can thus be either plus or minus 200 KHz. As the optical receivers have a resonance frequency of 1200 KHz, the output frequency of the receivers is given by the beating frequency minus the resonance frequency. This leads to a range of 600-200 KHz. In an electronic signal processing unit, these frequencies are translated to an analogue voltage as follows:

f_{out} [KHz]	U_{out} [Volts]
200	10
400	0
600	-10

The actual velocity range that can be measured depends on the main lens used to focus the 3 beams to the measuring point. This can be seen in Figure 12, where the angle α can be in- or decreased by switching lenses with different focal lengths. When angle α is decreased, the doppler shift for a certain velocity will be smaller, thus a higher velocity can be measured before the limit of the optical receiver is reached. For example, with a lens having a focal length (F) of 400mm, a velocity range of ± 2m/s can be covered. With a reference beam-main beam pair, one can only measure the velocity component of the flow in the direction of the bisector between the lines SP-PQ. There are however two of these pairs, so that the full velocity vector can be determined by combining the signals from both optical detectors. A calibration is required to determine the angles of the laser beams and to determine the velocity components.

3.2.3 LDV calibration

The goal of the LDV calibration is to convert the two analogue voltage outputs from the LDV unit to a two-dimensional velocity vector in the cartesian coordinate system (x, y and z-components).

The Deltares LDV laser unit comes calibrated with known angles between the laser beams. Unfortunately, due to the refraction of the laser beams with the multitude of material transitions of the vortex tank set-up, the displacement of the laser unit does not lead to an equal displacement of the measuring point. An additional calibration to correct this difference is therefore necessary.

3.2.4 LDV position calibration

A traversing unit with digital position indication is mounted on top of the vortex tank in the x-direction. To this traversing unit, a levelling needle is attached. The idea is to have the crossing of the laser beams, thus the measurement point, aligned on the needle point. The level needle is then traversed by a certain distance and the laser is traversed until the laser beams intersect the needle again and both new positions are recorded. This is repeated until the radius of the inner tank has been stepped and this measurement was conducted twice. The results of this measurement can be found below in Figure 13. This procedure was only applied in the x-direction as traversing in the y-direction introduces asymmetric refraction of the laser beams as they would cross the circular inner tank at different angles.

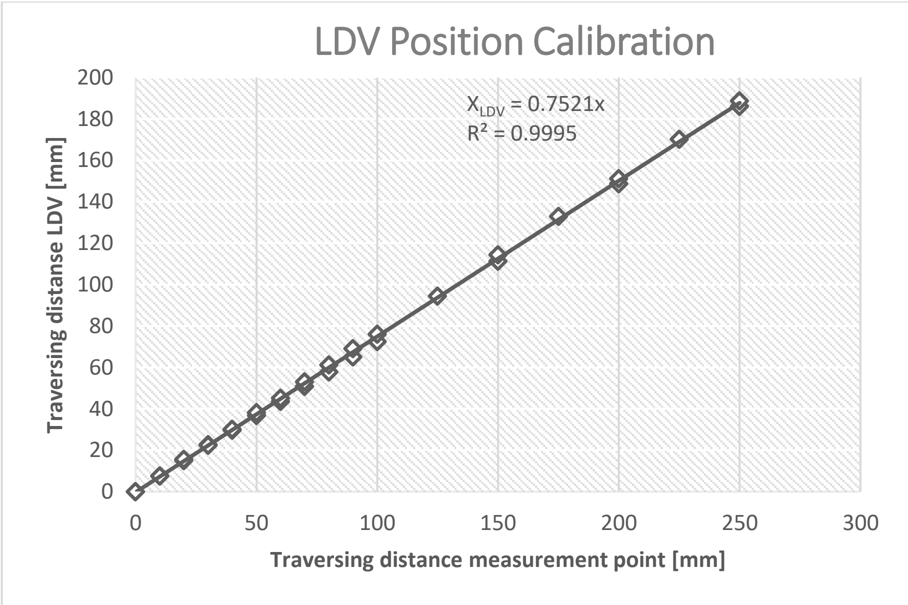

Figure 13 - LDV position calibration data. Linear fit is made on the data of two calibrations.

$$X_{LDA,Measured} = 0.7521x \tag{3.4}$$

A mathematical calculation is performed by the means of ray tracing to check the results of the calibration. The calculation can be found in Appendix C -LDV position calibration. The result is displayed below in Figure 14.

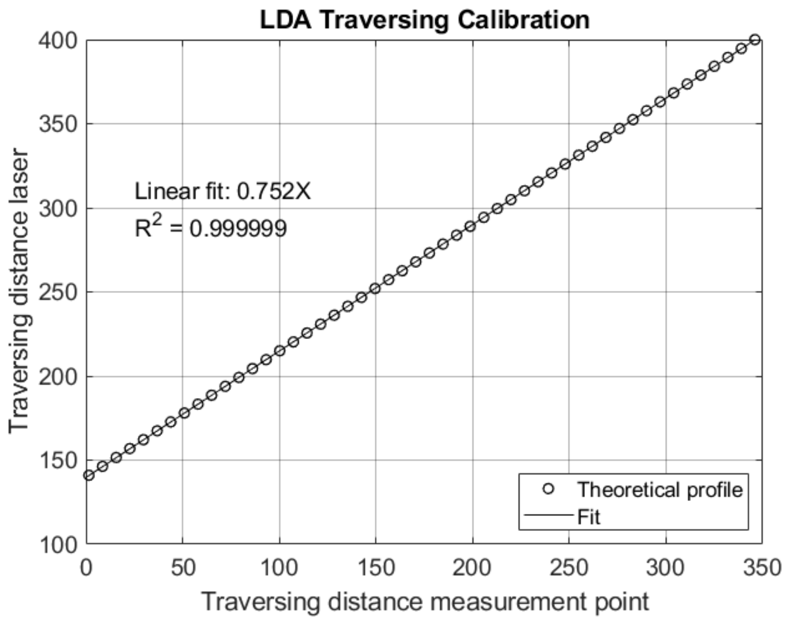

Figure 14 - Mathematical relation between the traversing outside and inside the vortex tank.

$$X_{LDA,theoretical} = 0.7519x \quad (3.5)$$

It is striking how alike the theoretical and actual relations are, with only 0.026% difference. This is an indicator that the geometry of the vortex tank is dimensionally accurate to the design and the refraction indices of air, water and PMMA are correctly implemented in the calculations.

3.2.5 LDV potentiometer calibration

A linear potentiometer is attached to the LDV traversing mechanism so that the position readout is recorded together with the LDV signal. The potentiometer is calibrated in a similar way as the LDV, the potentiometer output voltage was recorded while making 10mm steps with the LDV traverser. The data of this calibration is found in Figure 15.

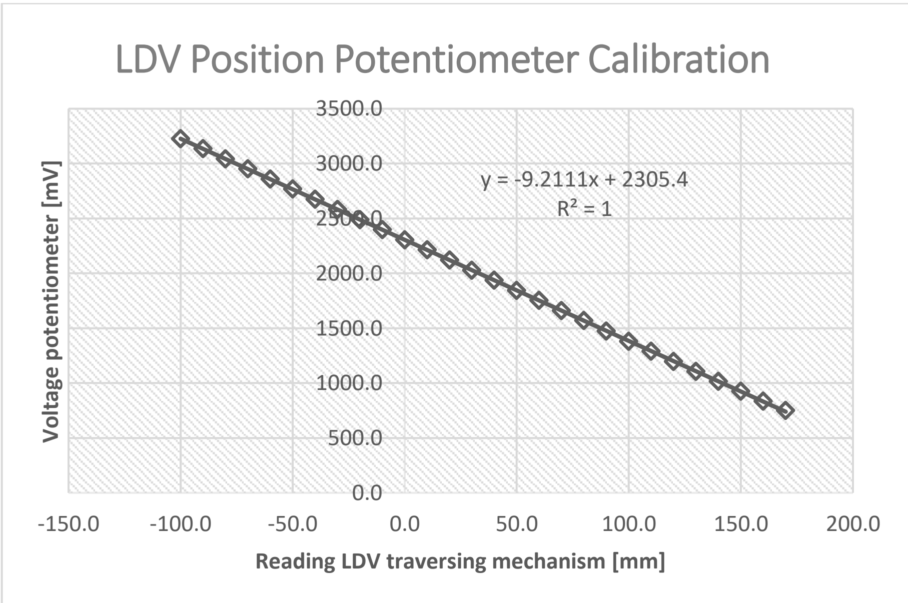

Figure 15 - LDV traversing potentiometer calibration.

The linear relation between the traverser reading and the potentiometer output voltage is:

$$U_{pot} = 9.2111 X_{LDA} \quad (3.6)$$

We can now relate the measurement location within the vortex tank to the potentiometer reading:

$$x = 0.1444(U_{pot} + A) \quad (3.7)$$

The constant *A* in above formula is determined to be -1096 mV by reading the voltage when the measurement location is in the centre of the vortex.

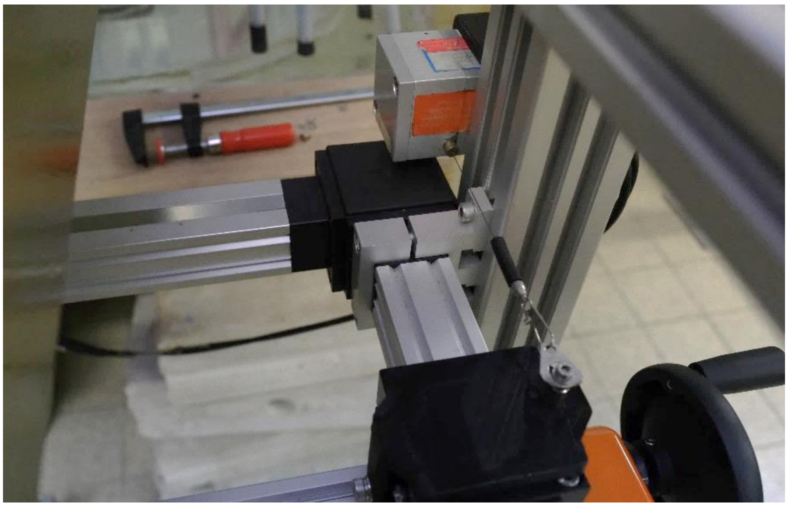

Figure 16 - Linear potentiometer is connected to the x-axis traversing mechanism of the LDV laser unit to record the location of the laser. Through a calibration, the location of the LDV measurement volume within the tank can be determined accurately.

3.2.6 LDV velocity signal deconvolution

The LDV measurements are subject to convolution of multiple sources. First, the vortex core centre location, (*r=0),* is non-stationary and is subject to the so-called "vortex wandering". This leads to spatial averaging of the measured velocity profiles as the measurement location is stationary. Secondly, the measurement volume of the LDV is cigar-shaped in the radial direction. Unfortunately, the velocity gradients are the largest in this direction leading to smoothing of the measured velocity profiles. Both convolutions are illustrated in Figure 17.

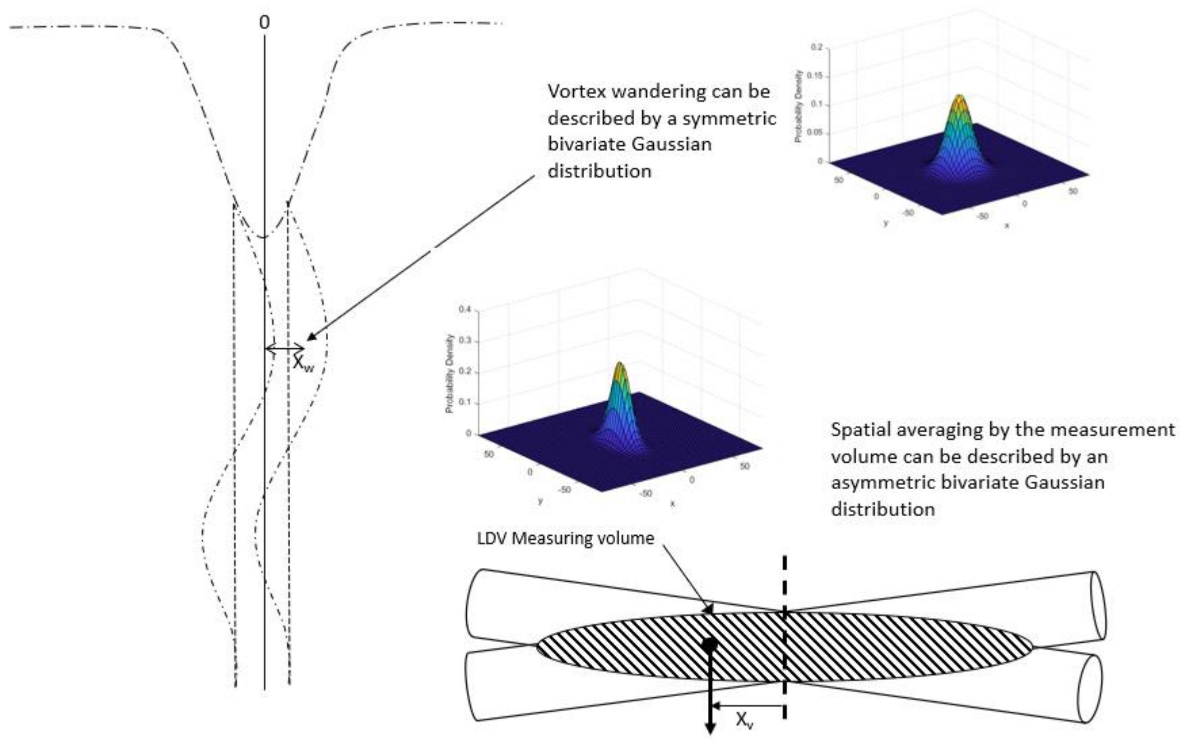

Figure 17 - Convolution of a fixed point LDV measurement. Note that this is a 2D simplification.

The method of deconvolution described in this section is mainly based on the work of Devenport (1996) and Pasche (2014) which also included the measurement volume smearing effect introduced by the LDV as Devenport (1996) only looked at wandering as he used hot wire velocimetry. We start by describing (assumed) the vortex wandering by a bivariate probability density function:

$$P_w(x_c, y_c) = \frac{1}{2\pi\sigma_w^{\ 2}} \exp\left(-\frac{x_c^{\ 2} + y_c^{\ 2}}{2\sigma_w^{\ 2}}\right) \tag{3.8}$$

In which x_c and y_c represent the wandering core location relative to the time averaged core location and σ_w is the wandering amplitude. A similar expression can be found for the measuring volume:

$$P_v(x_v, y_v) = \frac{1}{2\pi\sigma_{x,v}\sigma_{y,v}} \exp\left(-\frac{1}{2}\left(\frac{x_v^{\ 2}}{\sigma_{x,v}^{\ 2}} + \frac{y_v^{\ 2}}{\sigma_{y,v}^{\ 2}}\right)\right) \tag{3.9}$$

Where x_v and y_v are the deviations from an infinitesimal point in the centre of the measurement volume. Unlike the wandering amplitude for which we still need to find a suitable estimate, the variances of the focussed beam waist in the radial and tangential direction are known properties of the hardware. Several studies, e.g. (Wada et al., 2022) define the length and diameter (l_m and d_m) of the LDV measuring volume as follows:

$$\begin{aligned} d_m &= d_e / \cos(\alpha) \\ l_m &= d_e / \sin(\alpha) \end{aligned} \tag{3.10}$$

Where d_e is the beam waist diameter at the focal point for a gaussian distributed beam and given by:

$$d_e = \frac{4F\lambda}{\pi d_b} \tag{3.11}$$

The half-angle between the reference beams α , focal length F and wavelength λ were discussed in section 3.2.2. The laser beam waist width for the used system (d_b) is 1mm. This value was obtained from a previously performed calibration of which the result can be found in Appendix B -LDV beam diameter calibration. Since the beam waist is defined as the diameter where 95% of the energy exists, we can find the variance by just dividing by 4 ($0.95 = \pm 2\sigma$). Table 1 gives an overview of the corresponding measurement volume sizes and variances:

Table 1 - Measurement volume properties

Size of the measurement volume	**[mm]**
Measurement volume length	l_m = 6.8
Measurement volume diameter	d_m = 0.32
Variance of the bivariate probability density components	**[mm]**
Length	$\sigma_{v,x}$ = 1.7
Diameter	$\sigma_{v,y}$ = 0.08

The average velocity field is now described by the following convolution function:

$$V_m(x_c, y_c) = \int_{-\infty}^{\infty} P_v\left(x_c - x_p, y_c - y_p\right)\left[\int_{-\infty}^{\infty} P_w\left(x_v, y_v\right) V\left(x_p - x_v, y_p - y_v\right) dx_v dy_v\right] dx_p dy_p \tag{3.12}$$

Following the procedure as proposed by Pasche (2014), this expression can be rewritten as:

$$V_m = P * V \tag{3.13}$$

With:

$$P(x,y) = \frac{1}{2\pi\sqrt{\sigma_w{}^2 + \sigma_{v,x}{}^2}\sqrt{\sigma_w{}^2 + \sigma_{v,y}{}^2}} \exp\left(-\frac{1}{2}\left(\frac{x^2}{\sigma_w{}^2 + \sigma_{v,x}{}^2} + \frac{y^2}{\sigma_w{}^2 + \sigma_{v,y}{}^2}\right)\right) \tag{3.14}$$

Combining both the wandering and measurement volume variances, the only unknown variable at this point is the wandering variance. Devenport (1996) proposed a simple but effective expression to make an estimate of this value. He divides the root mean square tangential velocity measured in the vortex centre (which is assumed to be only caused by wandering) by the tangential velocity gradient:

$$\sigma_w \approx \frac{\sqrt{\overline{V_{\theta,m}^2(0,0)}}}{dV_{\theta,m} / dr} \tag{3.15}$$

In our case we found a value of σ_w in the order of 1.2 mm when using LDV data of a preliminary measurement re-enacting a measurement performed by Duinmeijer (2020). Re-evaluation of the PIV-measurement data obtained by Duinmeijer gave a wandering variance in the order of 1-2 mm, which increases the confidence in the estimated value.

Let us assume the following axial (Duinmeijer, 2020) and tangential (Burgers, 1948) velocity profiles:

$$V_z(x,y) = V_{z,\max} \exp\left[-\left(\frac{\sqrt{x^2+y^2} - r_c}{\alpha r_c} \right)^2 \right] \tag{3.16}$$

$$V_\theta(x,y) = \frac{\Gamma_\infty}{2\pi r}\left[1 - \exp\left(-\frac{x^2+y^2}{r_c{}^2} \right) \right] \tag{3.17}$$

When applying these velocity distributions in equation (3.13), we obtain a model of the convolution. Figure 18 shows the results of a discretized simulation using this model. The simulation was based on the hydraulic conditions ‘Series 2’ as described in (Duinmeijer, 2020) at a height of 29cm above the vortex tank bottom, using one inlet pipe, a discharge of $0.69 m^3/h$, an outlet diameter of 0.03m and a circulation or $0.08 m^2/s$.

Our main objective is to reverse the convolution by the wandering and measurement volume smearing. Devenport (1996) proposed a way of doing so analytically. First equations (3.16) and (3.17) are simplified by the following families of Gaussian distributions which represent the ‘true’ velocity profiles:

$$V_z(z,y) = \sum_{i=1}^{n} A_i \exp\left(-\frac{x^2+y^2}{a_i^2} \right) \tag{3.18}$$

$$V_\theta(x,y) = \sum_{i=1}^{n} \frac{B_i}{r}\left[1 - \exp\left(\frac{x^2+y^2}{a_i} \right) \right] \tag{3.19}$$

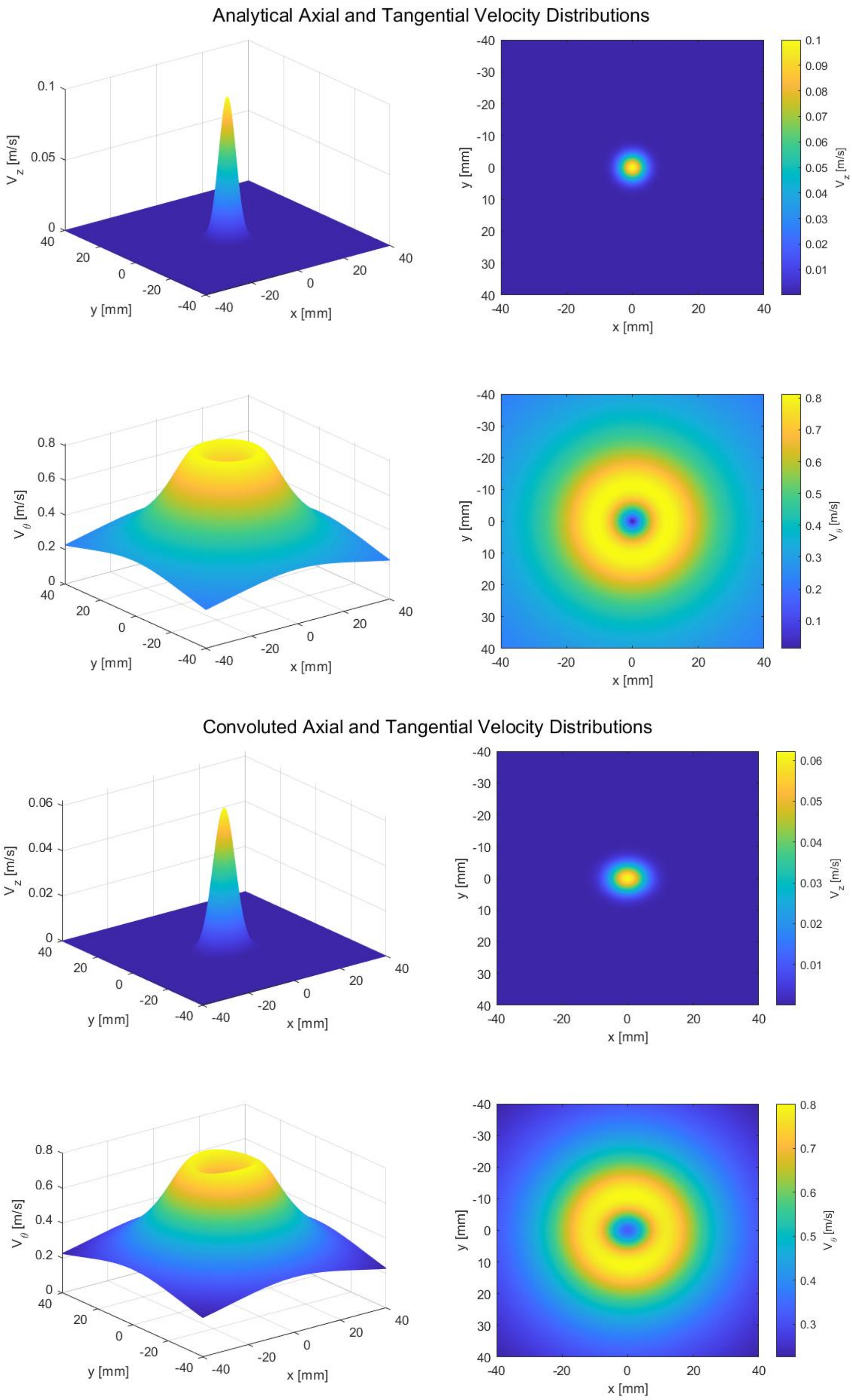

Figure 18 - The four upper figures show the undisturbed theoretical velocity distributions modelled in 2D. The four lower figures display the same distributions only now convoluted with both vortex wandering and measurement volume smearing. Note that the gradients have become less steep and the maxima have become smaller. Also, an asymmetry has appeared after convolution as the cigar-shaped LDV measurement volume mostly smears the gradients in the x-direction (radial direction)

Where $B_i = A_i a_i / 2$. When equation (3.18) and (3.14) are substituted into equation (3.13) and analytical integration is performed, the following expression for the convoluted axial velocity distribution is found along a cut through the middle of the distribution along the x-axis (radial direction):

$$V_{z,m}(x_p, 0) = \sum_{i=1}^{n} \frac{A_i a_i^2}{E_i^{1/2}} \exp\left(-x_p^2 \left[2\sigma_y^2 + a_i^2\right] / E_i\right) = \sum_{i=1}^{n} C_i \exp\left(-x_p^2 / c_i^2\right) \tag{3.20}$$

Where $E_i = \left(2\sigma_x^2 + a_i^2\right)\left(2\sigma_y^2 + a_i^2\right)$. In the case of the axial velocity, the coefficients C_i and c_i are determined by fitting the measured data. Devenport (1996) proposed the following transfer functions to obtain the coefficients for the 'true' profile:

$$\begin{aligned} a_i^2 &= \frac{1}{2}c_i^2 - \sigma_x^2 - \sigma_y^2 + \frac{1}{2}\left[(2\sigma_x^2 + 2\sigma_y^2 - c_i^2)^2 - 16\sigma_x^2\sigma_y^2 + 8\sigma_y^2 c_i^2\right]^{1/2} \\ A_i &= C_i E_i^{1/2} / a_i^2 \end{aligned} \tag{3.21}$$

Which can be substituted in equation (3.18) to acquire the deconvoluted profile. A similar approach can be used for the tangential velocity profile. First one fits the measured velocity profile to the following family of Gaussian distributions:

$$V_{\theta,m}(x_p, 0) = \sum_{i=1}^{n} \frac{D_i}{x_p}\left[1 - \exp\left(\frac{-x_p^2}{c_i^2}\right)\right] \tag{3.22}$$

With the following transfer function, the coefficients for the 'true' profile are obtained:

$$B_i = D_i\left(2\sigma_x^2 + a_i^2\right) / E_i^{1/2} \tag{3.23}$$

The coefficients c_i represent the radial scales of the families of fitted Gaussian distributions. These are chosen to be linearly spaced with the smallest value given by $c_i > \sqrt{2\sigma_x^2}$ and the largest value given by the farthest measurement point from the centre. The number of Gaussians (*n)* should not exceed half of the total number of measurement points.

3.3 Techniques for motion tracking of solid particles

In this section, the measurement technique that is applied to quantitatively obtain the dynamics of the experimental particle is discussed. With the particle dynamics known, the equation of motion of the particle can be completed and the drag on the particle can be obtained.

3.3.1 Particle Tracking Velocimetry (PTV)

PTV is applied to track the experimental solid particle within the vortex tank. Scripts for post-processing of the PTV images are developed and tested on its accuracy and applicability. A desktop PC with dedicated hardware for image acquisition of high-speed cameras is made available by the TU Delft. Image acquisition software (StreamPix) and three FLIR ORYX cameras were made available by Deltares. The FLIR ethernet cameras have RGB chips and use a colour depth of 8 bit and are hardware triggered at 60Hz. They are outfitted with 12.5 mm Fujinon C-mount lenses and manually focussed on the face of the vortex tank. The cameras have a maximum sensor size of 3208 × 2200 pixels, but only 640 x 2304 pixels are acquired during the experiments to reduce the amount of data.

Figure 19 - One of three PTV cameras. After calibration, the cameras should not be moved even the slightest, hence the sign.

A script was developed by F. Clemens to determine the position and orientation of solid bodies in the vortex tank. Clemens uses a method of perspective bundle confinement to obtain the position and orientation of the particle. For any solid body shapes that is not point symmetric (non-spherical), it would be possible to determine the orientation and thus rotation by perspective bundle confinement only. As the particle studied in this thesis is a sphere, we must resort to placing markers on the particle surface, in this case randomly placed dots.

3.4 TIME SYNCHRONIZATION OF MEASUREMENT TECHNIQUES

Analog measurement signals are acquired by the Deltares Delft Measure (version 1.6.5.2) software and 16-bit AD converter from National Instruments. The data acquisition unit used was equipped with a TTL pulse output port such that the PTV image acquisition software (StreamPix) can be triggered to start recording images, so that both the start of the measurements in Delft Measure and that of the PTV measurements are synchronized. Furthermore, the image acquisition software triggers all three cameras to capture the images simultaneously. This trigger is also looped back into the analog signal acquisition module so the moments of image capture can be linked to the instantaneous water velocity measurement by the LDV. The AD converter acquires 10 channels at a sample frequency of 2kHz as the maximum measurement frequency of the LDV system is 1kHz (we use double the measurement frequency to avoid aliasing).

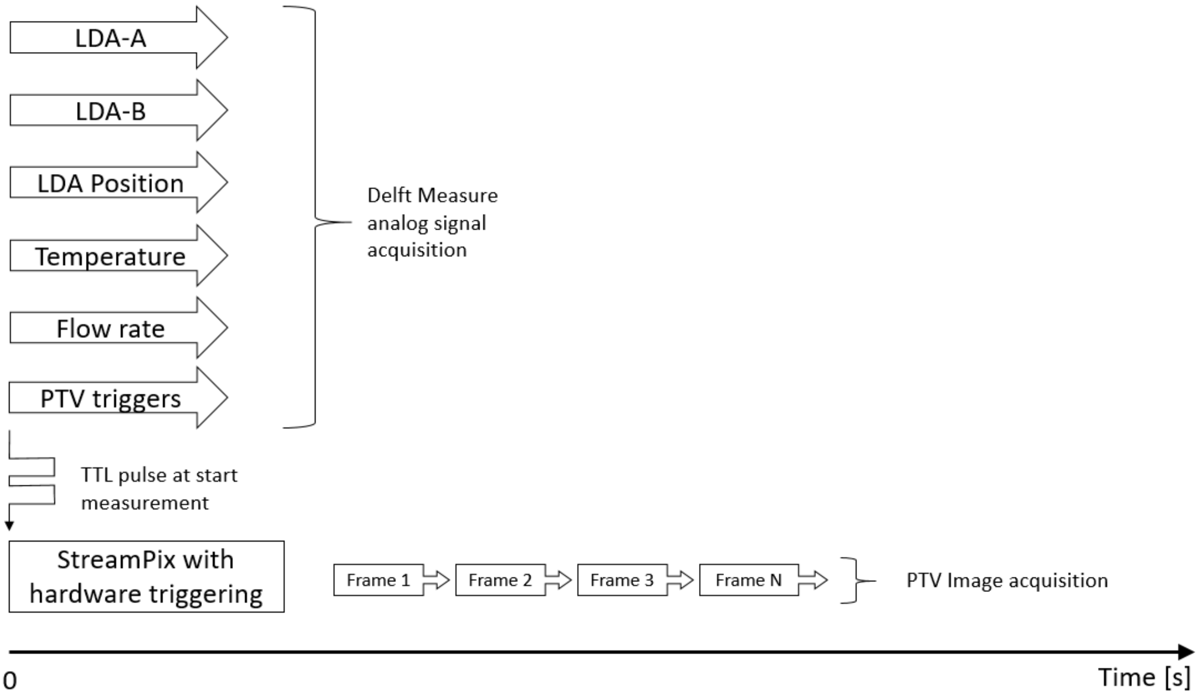

Figure 20 - Schematic of the synchronization of the analog data acquisition with the image acquisition hardware.

4 EXPERIMENTAL PROGRAM

4.1 EXPERIMENTAL FRAMEWORK

An experimental framework is presented here to prevent this research from diverging from the goal and to limit the number of input variables leading to an unrealistic number of experiments.

4.1.1 Buoyant particle

As a buoyant particle, a 3D printed Poly Lactose Acid (PLA) sphere with a diameter of 25mm will be used. This sphere has a density of 766 ± 8 kg/m^3.

4.1.2 Hydraulic conditions

Two flow conditions will be used: A flow condition chosen the same as 'series 2' from the dissertation of Duinmeijer (2020) to enable comparison of the results, hereafter referred to as H2.

A second flow condition is chosen specifically for this study. We meant to find the flow conditions for which the smallest downward motion of the experimental particle is observed. This allows for low velocity transport along the vortex core thus maximizing the measuring time. This flow condition is the basis for the subsequent experiments. During this experiment, the discharge was slowly increased while the EP is in the surface dimple of the vortex. By trial and error, a value of 0.48m^3/h was found to satisfy this purpose. Table 2 gives an overview of the hydraulic conditions:

Table 2 - Overview of the hydraulic conditions

Hydraulic condition	Discharge (Q)	Circulation (Γ_∞)	number of inlets	Outlet diameter
ID.	[m^3/s]	[m^2/s]	[#]	[m]
H1	0.48	0.049 ± 0.001	2	0.03
H2	0.69	0.08 ± 0.00	1	0.03

4.1.3 Region of interest

All (except one) LDV experiments were performed on a fixed line parallel to the x-axis intersecting the vortex axis (see Figure 8) which is referred to as D1 (Direction 1). One single experiment was performed on a line parallel to the y-axis, intersecting the vortex axis and is denoted as D2. All experiments were performed at a height of z=29cm from the bottom of the vortex tank, allowing for comparison with data from previous studies (Duinmeijer et al., 2020) who used the same plane height to perform PIV measurements. The benefit of this vertical measuring location is also the limited vortex wandering, as it is closest to the bottom where the vortex location is 'bound' to the outlet.

4.2 EXPERIMENTAL MATRIX

Three sets of experimental series were proposed:

4.2.1 Series 1 - Benchmark experiment

One benchmark experiment was performed to test the performance of the LDV. The H2 hydraulic condition from Duinmeijer was re-created for validation against earlier obtained data by PIV. It consists of a transect (a multitude of individual point-measurements along a line) through the vortex core.

4.2.2 Series 2 - Velocity profiles in the absence of a particle

LDV transects though the vortex core were executed with hydraulic condition number one to quantify the core radii and axial velocity profiles in absence of an experimental particle. It is also expected that these experiments provide more information on the turbulent characteristics of the vortex flow.

4.2.3 Series 3 - Velocity profiles in the presence of a particle

In these experiments PTV and LDV were deployed simultaneously. During each individual point measurement on the transect, the EP was released and transported along the vortex axis. After some waiting period to allow the flow to normalise, the LDV was traversed and the measurement repeated.

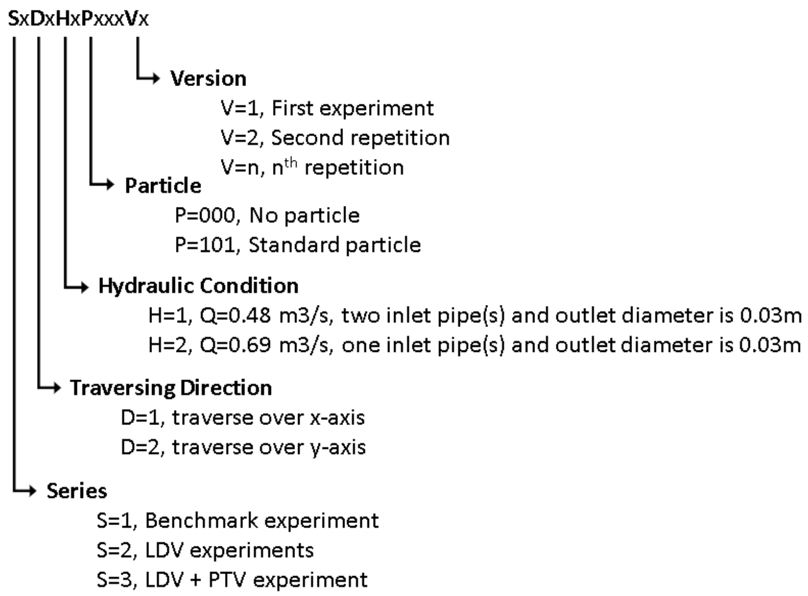

Figure 21 - Schematic showing the coding of the experiment's names.

Table 3 gives an overview of all the performed experiments, including unsuccessful ones (given in grey). These are not presented in the results sections.

Table 3 – Experiment overview (unsuccessful experiments depicted in grey)

Experiment ID.	**Remarks**
Series 1	
S1D1H2P000V1	Two-sided LDV transect re-enacting 'series 2' from Duinmeijer
Series 2	
S2D1H1P000V1	One-sided LDV transect over longer radial distance
S2D1H1P000V2	*Two-sided LDV transect (bad measurement as zero y-location was off)*
S2D1H1P000V3	Two-sided LDV transect
S2D2H1P000V1	*Two-sided LDV transect over y-axis (bad measurement as zero x-location was off)*
S2D2H1P000V2	Two-sided LDV transect along y-axis
S2D1H1P000V1_M	Moving LDV transect along the x-axis
S2D0H1P000V1_D	Die contrast experiment, only footage was obtained during this experiment
Series 3	
S3D1H1P101V1	Two-sided transect deploying LDV and PTV simultaneously

5 RESULTS

5.1 RESULTS - VELOCITY PROFILES IN ABSENCE OF A PARTICLE

This section presents the results of the first two series of experiments, the benchmark measurement and the velocity profile measurements in absence of a particle.

5.1.1 Comparison with previous work

Experiment (S1D1H2P000V1) is a two sided transect through the core using the hydraulic conditions of Duinmeijer (2020). The transect consists of sixty individual time averaged point measurements (measuring time of 180s at 2kHz). The spatial resolution is approx. 0.6 mm between the point measurements in the vicinity of the centre and 2.4 mm further outside the core. Figure 22 shows the axial and tangential LDV velocity profiles and the deconvoluted profiles. Furthermore, it shows the tangential and axial velocity profiles based on the PIV data collected by Duinmeijer. The theoretical Burgers tangential velocity profile is also displayed.

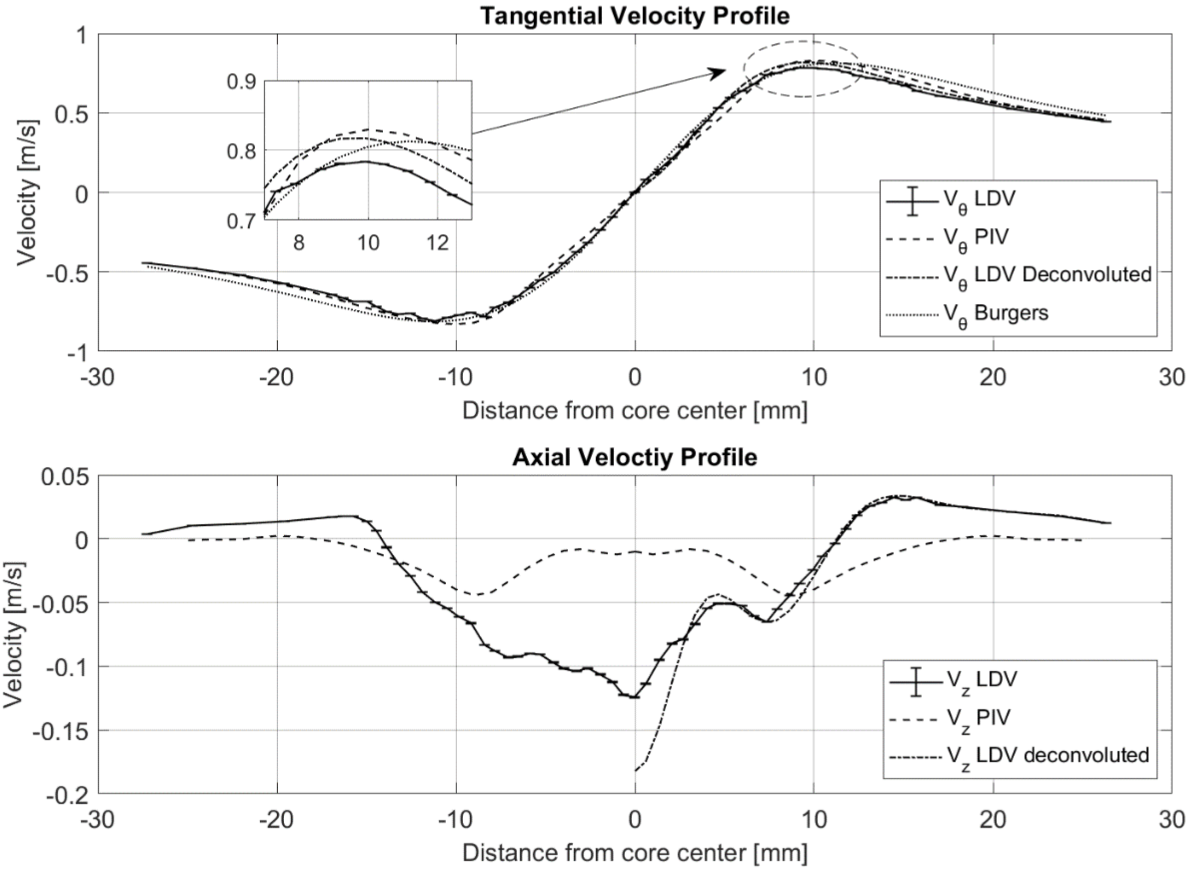

Figure 22 – Measurement S1D1H2P000V1 showing the tangential (Top) and axial velocity profiles (Bottom) including the 95% confidence intervals (which are very narrow). The deconvoluted profiles are depicted with the dash-dotted lines. The figure also shows the 'series 2' condition PIV data from Duinmeijer and the Burgers tangential velocity profile.

The measured LDV tangential velocity is in accordance with the PIV data from Duinmeijer: The locations of the maximum tangential velocities overlap perfectly, and the magnitude of these maxima differ by 5% at most, with the PIV data showing slightly higher values. The deconvoluted velocity profiles are also depicted in the same figure, these show an increase in magnitude of both tangential and axial velocity and make the velocity gradients steeper. The deconvolution is based on a vortex wandering amplitude of 1.15 mm calculated via equation (3.15) and a measurement volume smearing with a variance of 1.7mm as given in Table 1. This leads to a spatial averaging effect over a radial domain of approximately

2 mm. The deconvolution corrects for this effect. Deconvoluting the LDV measurement decreases the difference with the PIV data to at most 1.5%. The difference between the maxima of the deconvoluted LDV profile and the theoretical tangential Burgers profile, which is also depicted in the same figure, is only 0.6%. It is unlikely that this is within the accuracy range of the deconvolution procedure as it is dependent on the vortex wandering amplitude and the measurement volume which are difficult to quantify exactly. The radial locations of the peaks seem to differ by 1 mm where the Burgers profile is slightly wider.

The axial velocity profile shows a rather different image: Duinmeijer measured the maximum axial velocities near the core radius, where this study shows the maximum axial velocity in the centre and a second local maximum at approximately 70% of the core radius.

5.1.2 Standard transects

This is the second series of measurements where the velocity profiles in absence of the EP with hydraulic condition H1 are determined.

In the first measurement (S2D1H1P000V1), a core traverse is performed along the x-axis with a step size of 0.5mm in the vicinity of the centre and larger steps (up to 2mm) further away from the core where the velocity gradients are smaller. This measurement took place over two days, a small discontinuity in the velocity profiles is the result of the continuation of the experiment on the second day. The result of this measurement can be found in Figure 23.

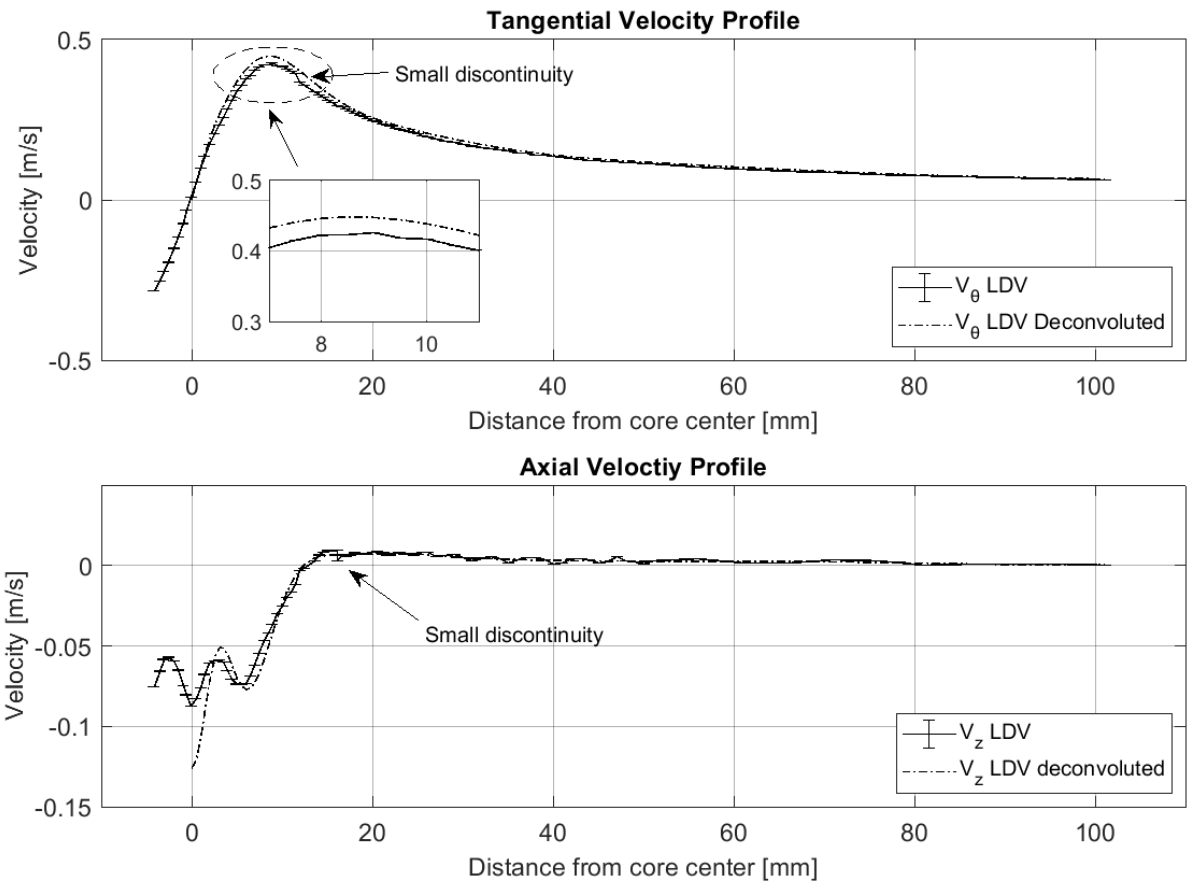

Figure 23 - Measurement S2D1H1P000V1.This measurement shows the one-sided tangential (top) and axial (bottom) velocity profiles including the 95% confidence intervals and the deconvoluted profiles. Note the small discontinuity of the measurement at r=15mm where the measurement was continued on the second day. The axial profile shows small 'waves' from r=20 onwards.

The measurement yields smooth axial and tangential velocity profiles. The wave-like structure around the zero-velocity line in the axial velocity profile is interesting, this may suggest the presence of secondary flows as multiple authors have observed before for example: (Mulligan et al., 2018) and (Andersen et al., 2003). The deconvoluted tangential and axial profiles show an increase of respectively 5% and 45% of the maximum velocities. The axial profile is amplified more severely than the tangential profile as the gradients are steeper and the width of the peaks have a width which is similar as the spatial smearing size. The peak location of the raw tangential profile and the deconvoluted profile coincide, where the deconvoluted axial profile shows a slight outward shift.

A second measurement (S2D1H1P000V3) was performed along the same axis but going in both directions from the core centre to test the symmetry of the velocity profiles. The result can be seen in Figure 24. The symmetry in the tangential velocity profile is strong but the axial velocity profile shows some asymmetry in the ‘double peak’ profile. This is not the first time that such asymmetry is observed in the axial velocity profile, (Duinmeijer et al., 2020) also observed asymmetries in most of the axial velocity measurements. The deconvoluted profiles show an increase of the tangential velocity of 6% and an increase of 90% for the axial velocity. The original and deconvoluted profiles of the tangential velocities for both experiments S2D1H1P000V1 and S2D1H1P000V3 coincide well. The axial velocities (raw profiles and deconvoluted) show some differences in the magnitude of the peaks: The latter experiment shows a larger axial velocity in the vortex core. This explains the stronger amplification of the deconvoluted profile.

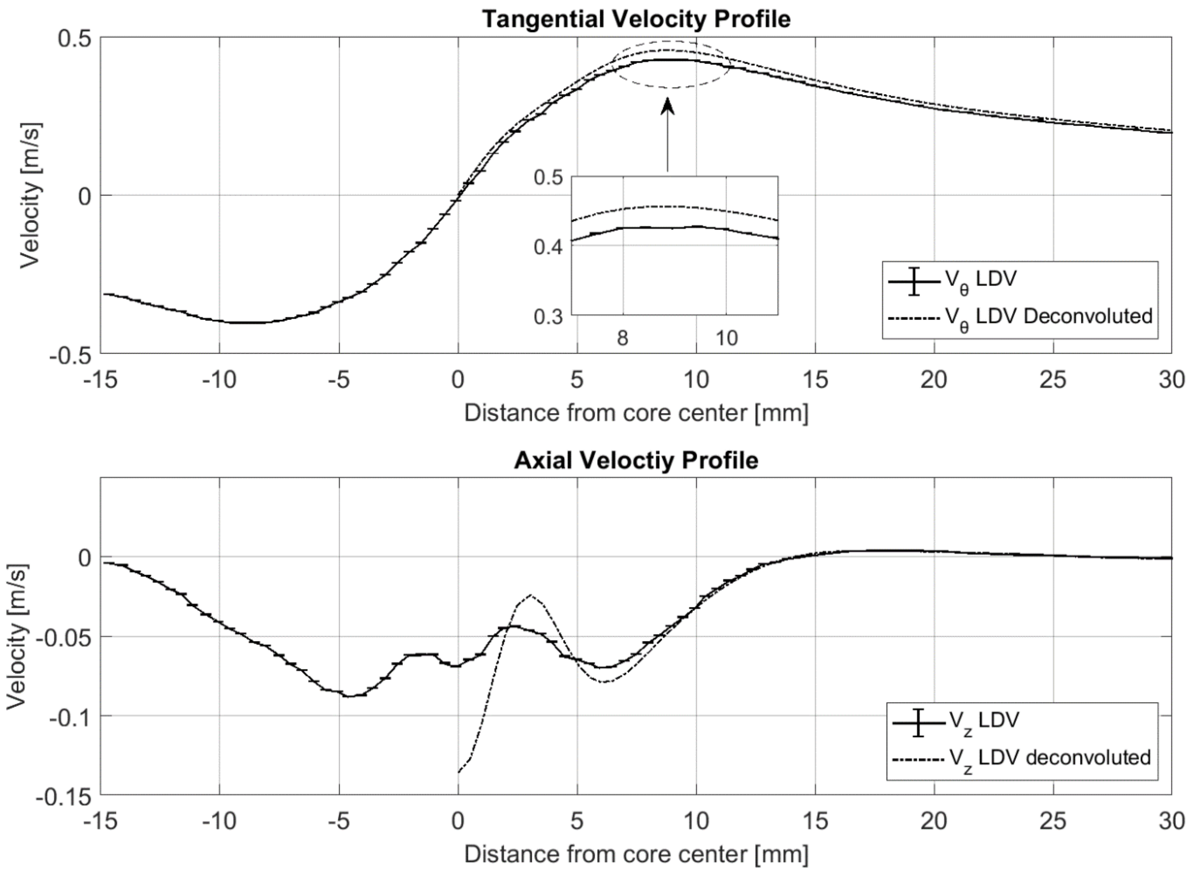

Figure 24 - Measurement S2D1H1P000V3.This figure shows the results of a two-sided measurement through the vortex core along the x-axis including the 95% confidence interval. The ‘double peak’ profile can be observed well in this measurement. Notable is the large asymmetry in the axial profile.

5.1.3 Alternative transect

During the PIV measurements of Duinmeijer (2020), the “double peak” in the axial velocity profile (see Figure 22), as seen in our measurements, was not observed. To test if this profile is the result of convolution by measurement volume smearing, we can partly exclude this effect by performing a measurement along the y-axis. In this way, the measurement volume has its short axis parallel with the strong gradients that are found in the vicinity of the core, thus not spatially averaging them out. In this configuration the LDV does not measure the tangential velocity but the radial velocity, see Figure 8. In the centre of the vortex, the measurement is the same as for the x-traversing direction. However, when moving further away from the core, the velocity gradients quickly align with the measurement volume. When moving circa 1.7mm away from the centre (one LDV measurement volume radius) the volumetric smearing of the gradients has already became significantly less. The disadvantage of measuring in this manner is that the optical receivers of the LDV must be occasionally moved, which is not preferred as it gives rise to differences in signal strength between measurements. Another issue is that the LDV reference beams start to misalign when moving further from the centre. They cross the inner circular Perspex tank at different angles and thus refract differently. The result of this measurement can be seen in Figure 25. It is obvious that the velocity profiles are less "smooth" than for the measurements along the x-axis, probably by the lack of measurement volume smoothing but possibly also by measurement errors arising from repositioning the optical receivers and possible misalignment of the beams. The profile must therefore be interpreted in a more qualitative sense as the magnitudes might not be accurate. When we investigate the shape, it seems that the shape of the axial flow profile is not changing significantly in comparison with the profiles measured over the x-axis and that a local maximum of the axial velocity in the centre of the vortex still exists (double peak profile).

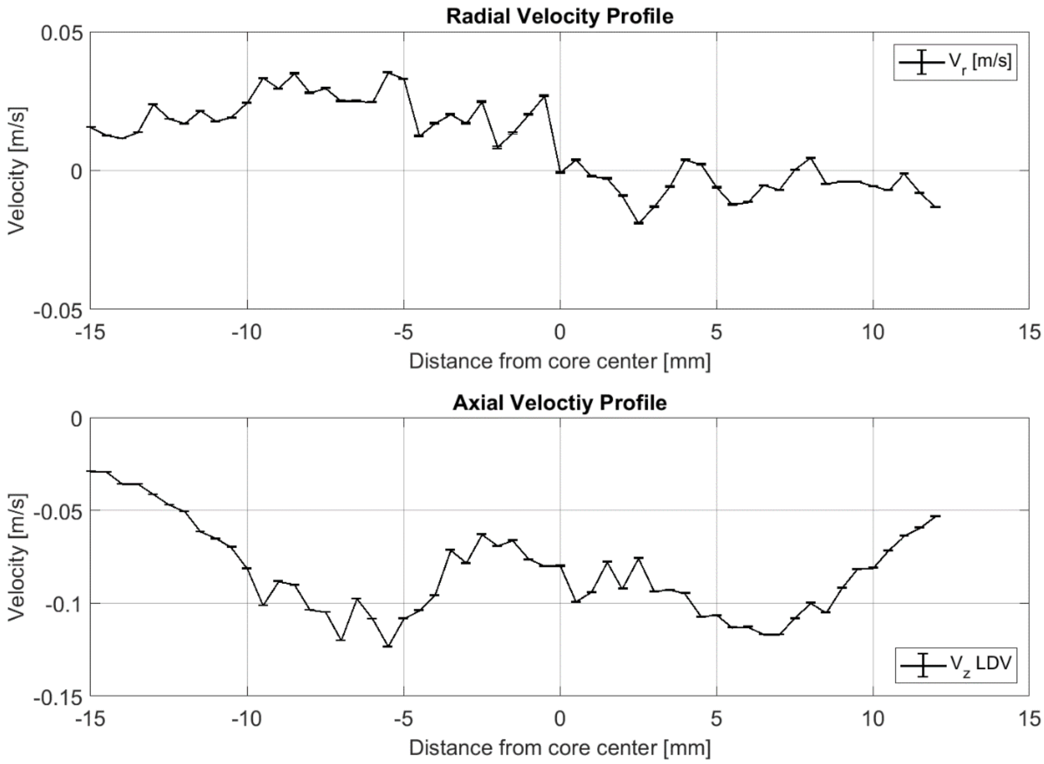

Figure 25 - Measurement S2D2H1P000V2. This measurement was performed through the vortex core along the y-axis. It shows the radial and axial velocity profiles. Note that this measurement is less smooth than the ones performed along the x-axis. The double peak profile is still observed.

5.1.4 Intermezzo – Slow vortex wandering

During the previous measurements it was sometimes visually observed that the vortex was wandering in a circular motion with a very low frequency, in the order of 30 seconds per cycle. A possible hypothesis is that this slow wandering is responsible for the local maxima. Duinmeijer (2020) introduced a Gaussian function to approximate the PIV obtained values. When this Gaussian function is translated around the origin with an amplitude of the same order of magnitude as the radius where the maximum axial velocity occurs, we get a new peak in the centre of the vortex. This effect is illustrated in Figure 26. By the wandering, the centre 'sees' both peaks passing by, thus leading to a local maximum and smoothing out the peaks where they normally are.

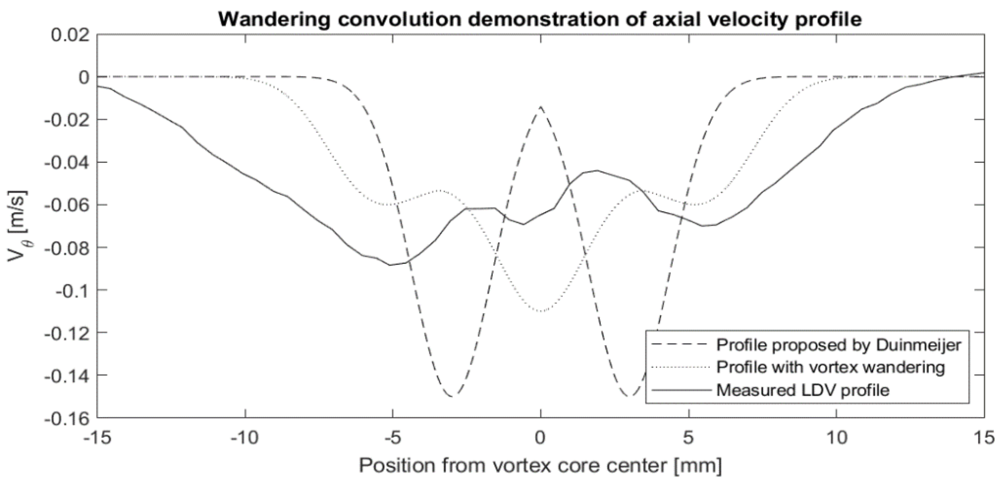

Figure 26 - Illustration of the convolution by vortex wandering. The wandering amplitude is set equal to the radius of maximum axial velocity (3mm). These values are not realistic but resemble the measured profile best.

To get the convoluted profile as described in Figure 26, a wandering amplitude in the order of the core radius is required which was not observed visually and quantitatively when applying equation (3.15).

5.1.5 Moving transect

One more experiment was proposed to test the effect of vortex wandering on the shape of the velocity profiles. Real-time LDV position measurement enabled us to perform a "moving transect", meaning that the LDV probing volume is moved through the vortex in a continuous motion instead of performing a series of point measurements. The benefit of such measurement is that the wandering of the vortex is not time averaged. During each transect, the LDV was manually moved through the core at a speed in the order of 2mm per second. Hydraulic condition number one (H1) was used. The result of ten of such 'moving transects' along with the average of these transects is shown in Figure 27.

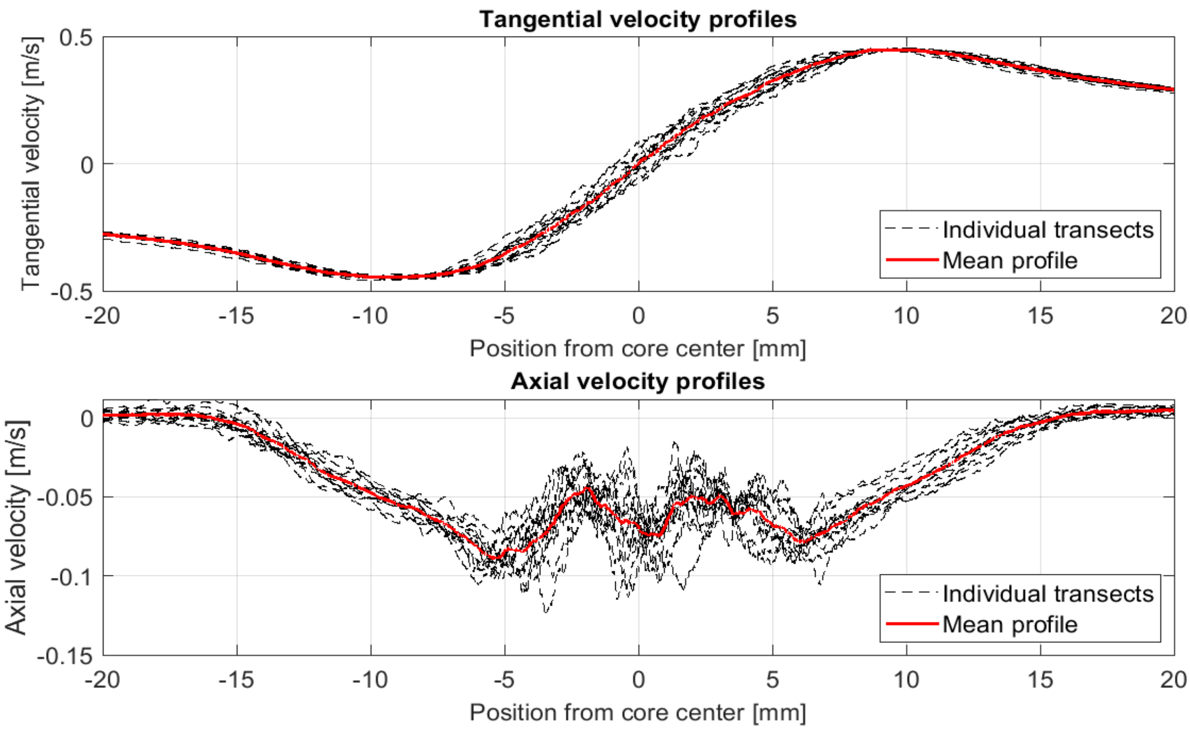

Figure 27 - Measurement S2D1H1P000V1_M. This figure shows the result of 10 moving transects through the vortex core including the average profile. Note that even without the time averaging effect, the 'double peak' profile is still visible.

From the individual axial velocity profiles, we observe that each profile has the ‘double peak’ profile. Some spread exists where the maximum velocities occur, but the individual profiles show strong similarity in general. Another clear observation is that the spread becomes larger towards the core: Apparently, the flow is much more time dependent (unsteady) there. This was observed earlier during the point measurement transects. Furthermore, in some transects, the middle peak is of a larger magnitude where in other transects the outer peaks show the largest axial velocities. The results also confirm that the amplitude of the vortex wandering is in the order of 1-2 mm. This can be observed from the spread of the individual tangential velocity profiles around the zero crossing.

5.1.6 Die contrast experiment

A simple qualitative die-contrast experiment, following the colorant front over time as it moves downward, confirms the unsteady character of the axial velocity profile in the vortex centre. At two moments in time, both a high contrast area leading at the core radius and in the centre of the vortex core can be observed (see Figure 28) alternatingly ‘overtaking’ each other. Sometimes the centre filament propagates quicker where sometimes the fluid at the core radius leads. When we time average this behaviour, we get the double peak profile as seen in all the transects. For this experiment the same hydraulic condition (H1) is used as for the standard transects.

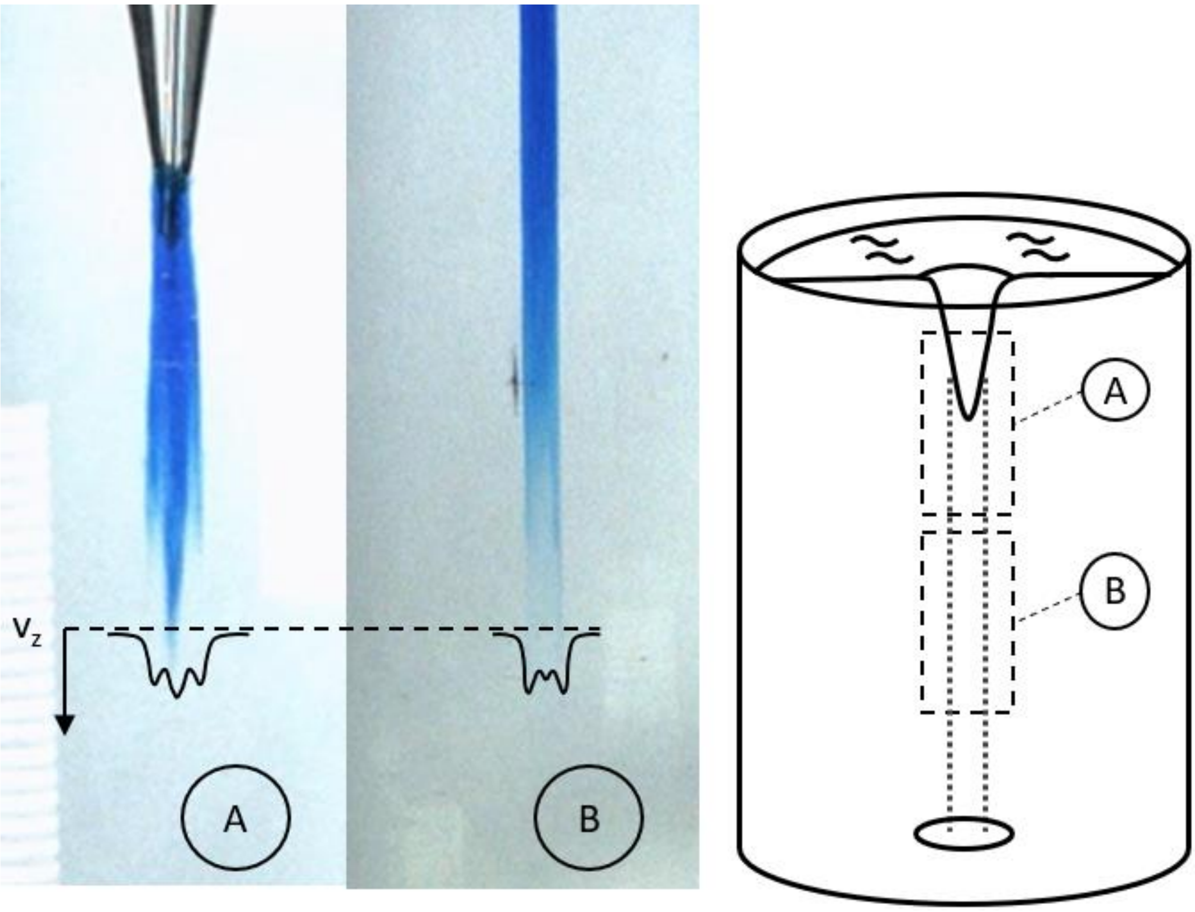

Figure 28 - Colour die experiment (S2D0H1P000V1_D) showing the variability of the axial velocity. Left: a string of die in the centre of the vortex seems to propagate quicker than the colorant surrounding it. Right: the die at the core radius seems to extend further down, thus propagating quicker than the filament of die in the centre. The depicted velocity profiles are a crude schematization of the measured axial velocity profiles.

5.1.7 Turbulence properties

Following the process described in section 2.5, we can determine the one-dimensional turbulent energy spectra for some measurement points along the two-sided transect S2D1H1P000V3. Figure 29 depicts these energy spectra for both the tangential and axial direction.

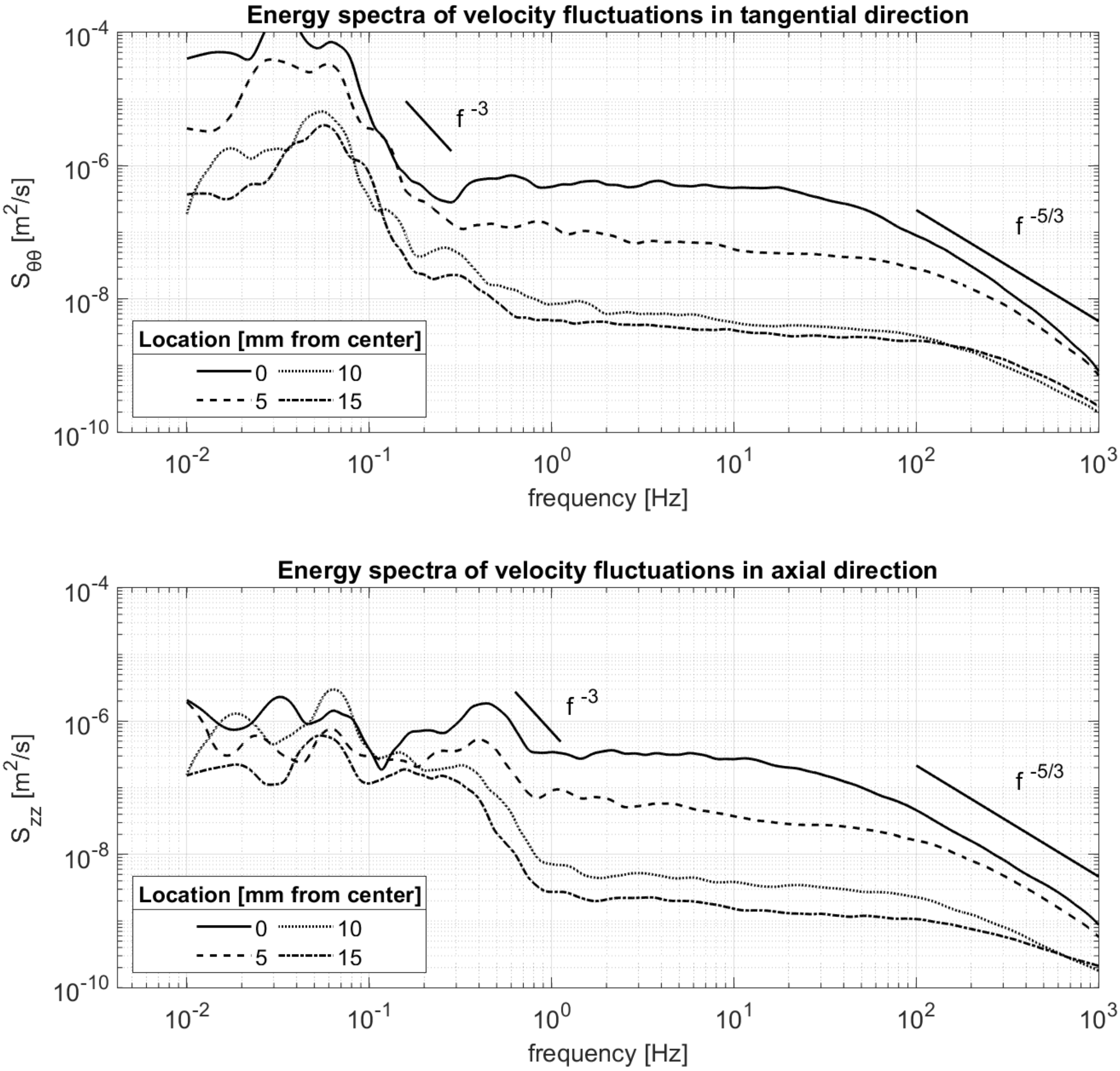

Figure 29 – One-dimensional turbulent energy distributions from experiment (S2D1H1P000V3). This figure shows the turbulent energy present in a range of frequencies. The energy distributions were determined for several radial locations along a transect through the vortex. There is a significant difference (order 500) in turbulent energy between the location in the vortex centre and the locations further outside the core.

These spectra confirm our expectation that the turbulent kinetic energy increases towards the vortex centre, see section 2.5. There is approximately 500 times more turbulent energy present in the vortex centre than 15 mm further outwards. The energy cascade in the inertial subrange seems to follow the $f^{-5/3}$ rule quite well (Nieuwstadt et al., 2016), only the spectrum measured in the core appears to be steeper. The rate of breakdown of the macro-scales somewhat follows a f^{-3} slope.

The increase of turbulent kinetic energy towards the vortex core might be illustrated more clearly when displaying the integral velocity scales, see equation (2.35), with the tangential and axial velocity profiles. Figure 30 shows that the turbulent fluctuations in the vortex centre are of a significantly higher magnitude than at higher radial locations. In the axial direction, these fluctuations are even of the same order of magnitude as the mean flow.

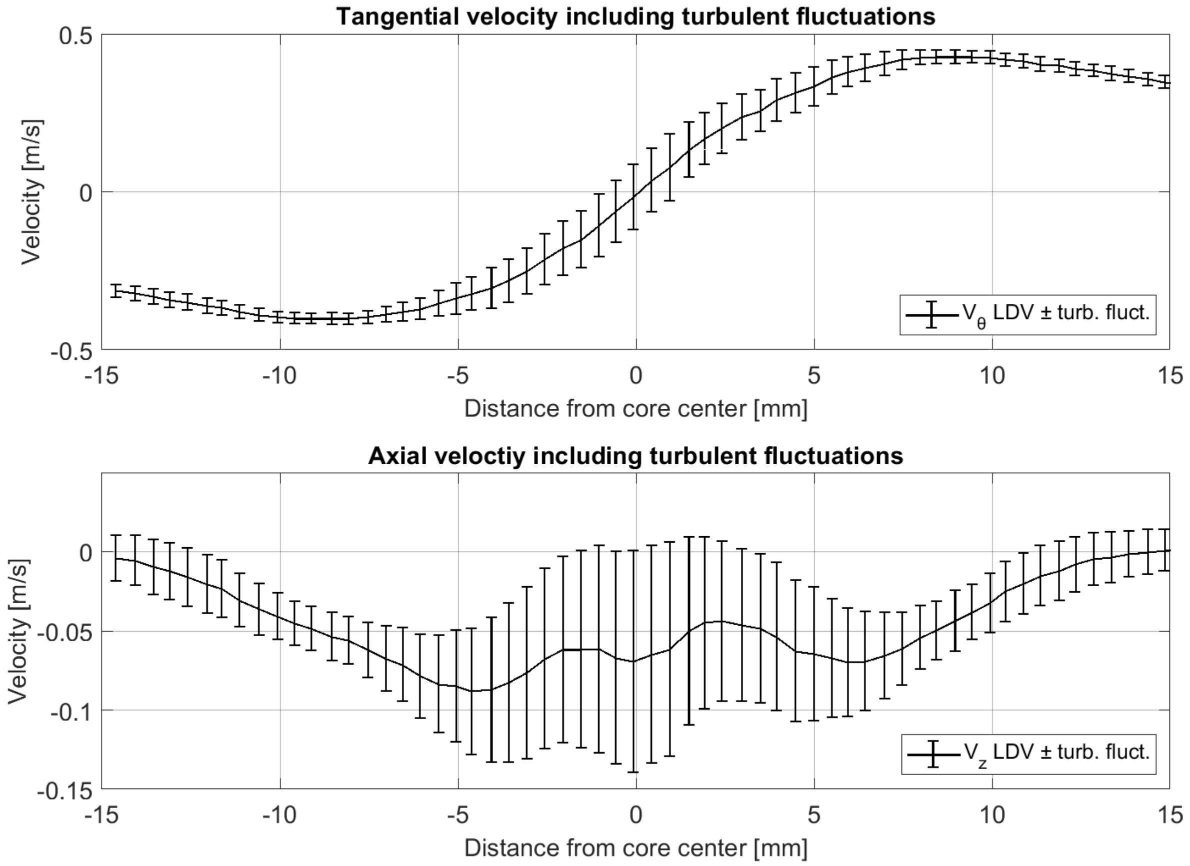

Figure 30 - Tangential and axial velocity profiles including the integral velocity scales per radial location

5.2 RESULTS – VELOCITY PROFILES IN PRESENCE OF A BUOYANT PARTICLE

This section presents the results of the third measurement series, the simultaneous PTV and LDV experiment where we determine the tangential and axial velocity profiles in the presence of the sphere.

5.2.1 Simultaneous experiments

After post-processing the PTV data (resolving the EP position), we remain with a time-synchronized dataset of instant water velocities and sphere positions. The vertical position of the sphere for all measurements is displayed in Figure 31. They are time synchronized on the moment that the centre of the sphere crosses the LDV transect to enable comparison.

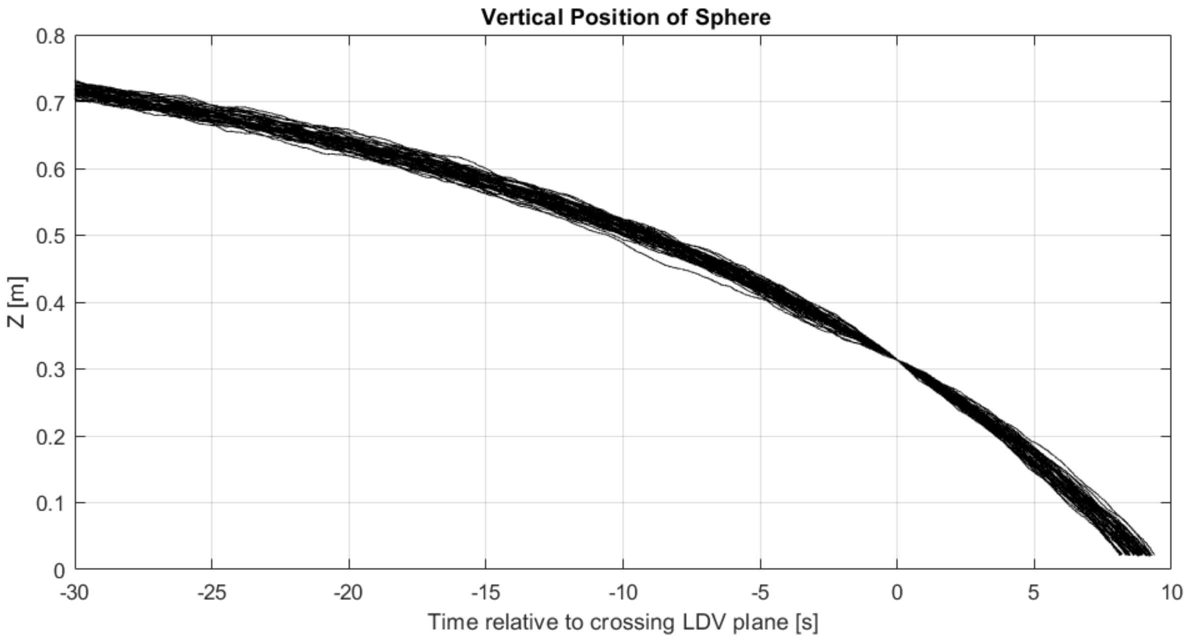

Figure 31 – Measurement S3D1H1P101V1. PTV sphere position for all forty-six point-measurements which the transect contains of. The measurements are synchronized at the moment that the sphere passed the LDV measurement plane (Z=0.29m). The transport of the sphere progresses quite similar for each experiment.

Given the sphere's locations and the location of the LDV transect, we can determine the water velocities as a function of the distance relative to the sphere: First, the times are determined at which the centre of the sphere passes (for example) 30mm above and 30mm below the transect. Then, the two-sided averages of the instantaneous velocity signal are taken around these timestamps. Since the sphere travels with a velocity of around 3cm/sec when crossing the transect, we can average over one second (half a second before and after the timestamps) without including the 'dead signal' in our average. This is the timeframe when the sphere is blocking the laser beams and thus where we measure nothing (see Figure 32). In Figure 33, the above process is graphically illustrated by the means of an instantaneous velocity measurement of the tangential velocity. Naturally, above method can also be applied to obtain the axial velocity profiles relative to the particle position.

In Figure 34, the resulting tangential and axial velocity profiles are shown. The most obvious feature of the tangential velocity profiles is the difference in tangential velocities above and below the particle. Above it, the velocities are clearly (0.1m/s) smaller than below. This is in accordance with the theory as described in section 2.3. The tangential velocity profiles, depicted in Figure 34, are average profiles taken from 3 measurements at different relative vertical distances from the sphere centre. The error bars in the figure give us the maximum spread of these individual measurements. From this spread it becomes obvious that the tangential velocity surplus/deficit is not that dependent on the distance from the particle. Another observation is the wider core radius (the radius where the maximum tangential velocities occur) in comparison with the case without a particle. It can be determined from the graphs that the core radii of the velocity profiles above and below the particle are respectively 10 and 11 mm. Where, for the same flow condition without a particle, the core radius is 9mm. It is not expected that this difference is the result of inaccuracy (by for example vortex wandering) as this trend is observed on both sides of the vortex which are independent measurements.

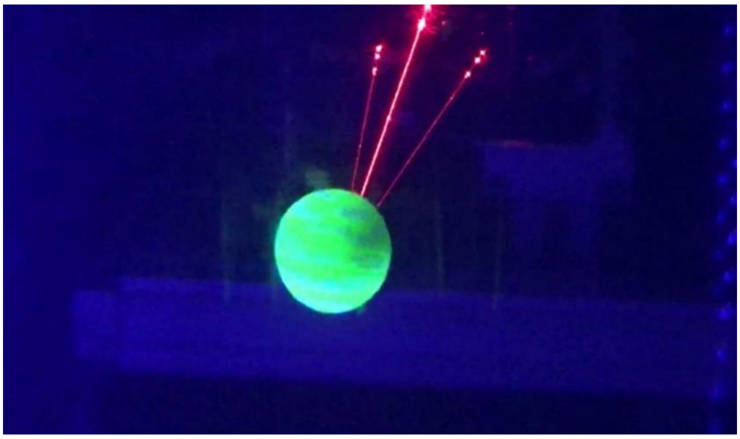

Figure 32 - Sphere blocks the laser beams when it is passing through the transect.

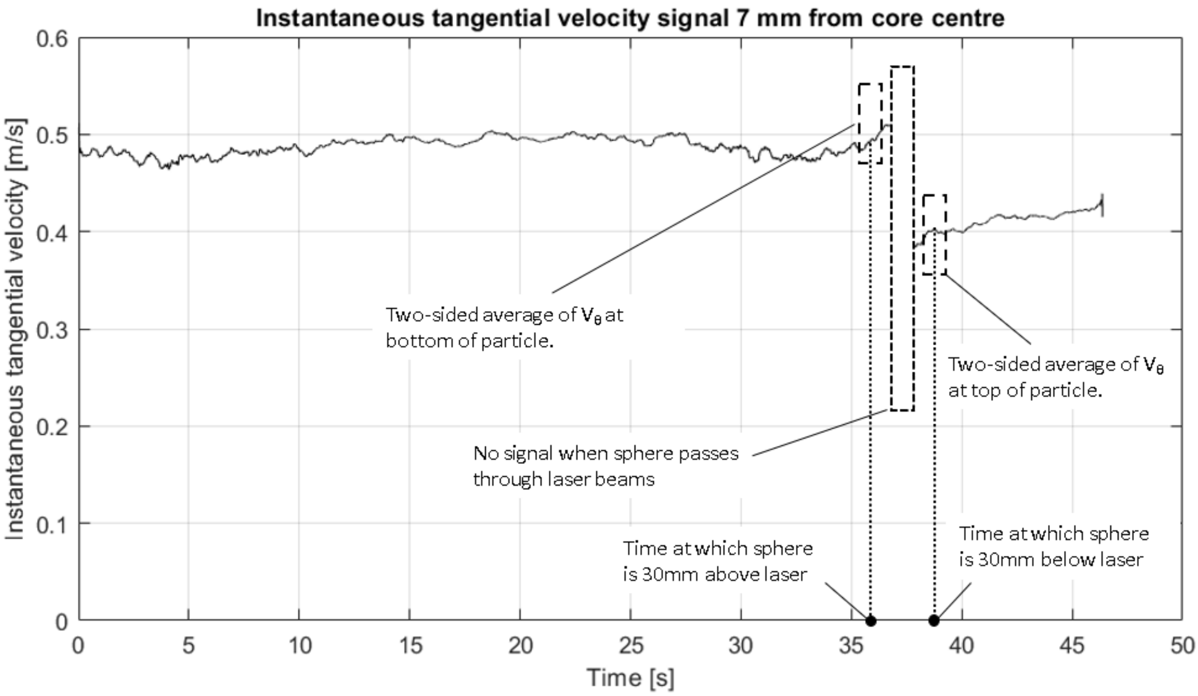

Figure 33 – Instantaneous tangential velocity signal from a single point measurement out of measurement S3D1H1P101V1 at approximately 7mm from the core centre. The gap in the graph around 37 seconds is where the sphere passes through the laser beams and the signal is lost. As the sphere approaches the LDV measurement point from above, the tangential velocity below the particle is measured first and after the signal is regained the velocity above the particle.

The axial velocity profiles in Figure 34 show some difference in velocity above and below the particle. It seems that the axial velocity at the outer peaks is higher underneath the sphere than above. In the vortex centre the velocities are of the same magnitude. The shape of the profiles is generally in agreement with the shape determined in the case without a particle. The profiles are however less smooth. This is most likely caused by the small number of samples that the measurement consists of: 2000 samples instead of 360,000 samples for a standard transect in the case of the velocity profile without a particle. As the sampling period is short, fluctuations in the flow can more easily influence the measurement.

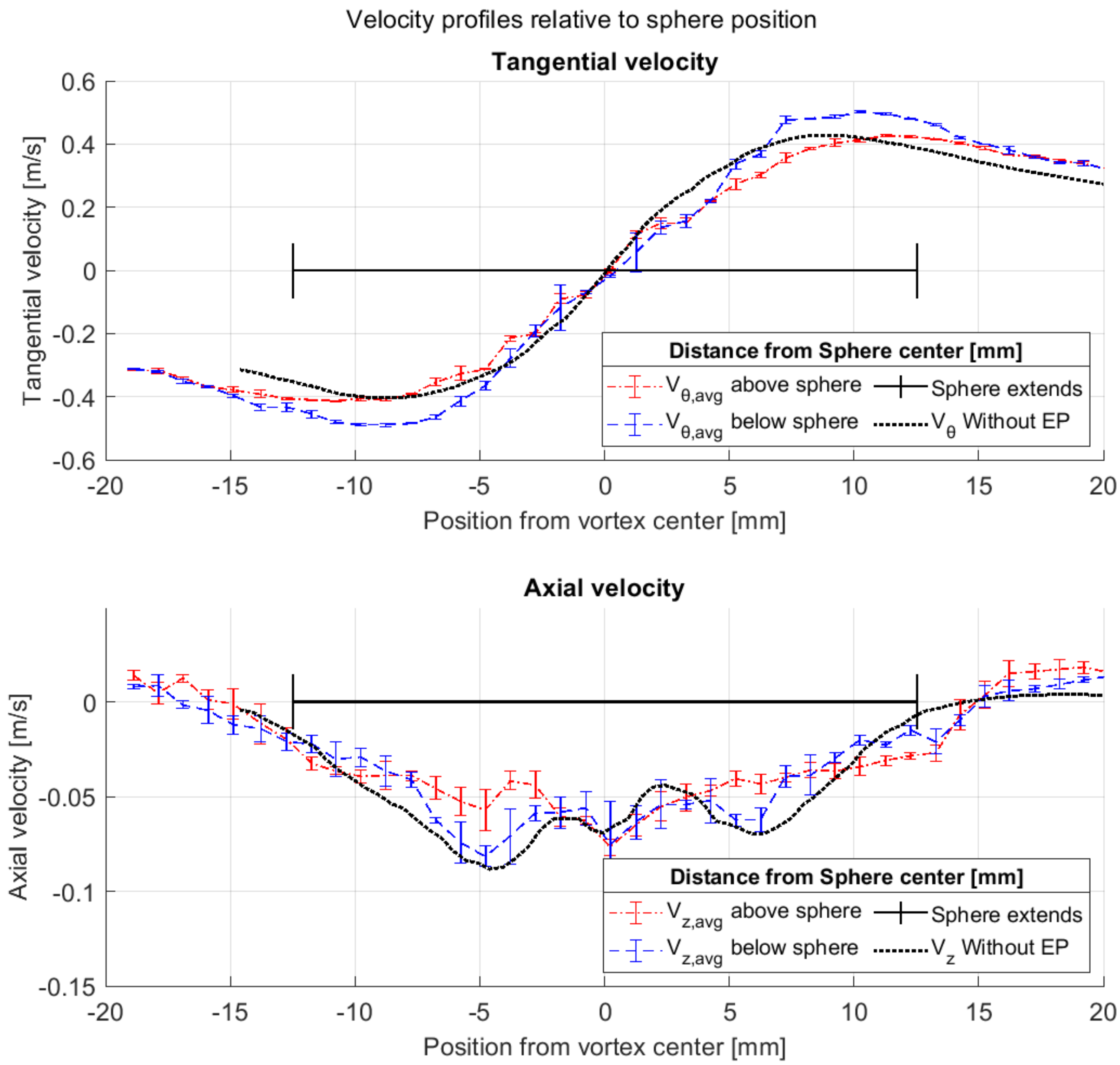

Figure 34 – Averaged tangential (top) and axial (bottom) velocity profiles measured above (red) and below (blue) the sphere. Each average velocity profile consists of 3 measurements (3, 10 and 20mm above/below the sphere centre). The spread represents the bandwidth of these separate measurements.

5.3 RESULTS - TAYLOR COLUMN DRIVEN MOTION

In this chapter, an attempt is made to quantify the downward force on the experimental particle. It is expected that the main driving force is the pressure difference present between top and bottom of the particle caused by the perturbated tangential velocities, as was described in detail in section 2.3.

We are probably in the unique position to have experimental data on the perturbated tangential velocity profiles thus, we may attempt to determine the downward force via the modified geostrophic balance which is fundamental to the problem. These results are presented in section 5.3.1. Furthermore, some existing drag coefficients were tested against our measurement data, these results can be found in sections 5.3.2 to 5.3.4.

5.3.1 Pressure perturbation calculation

As we have the perturbed tangential velocity profile available from section 5.2.1, we can fill in the modified geostrophic balance equation (2.22). The modified geostrophic balance formula was originally designed for a full-body rotating flow (Moore & Saffman, 1968). As the vortex flow is a combination between full body rotation in the core region and irrotational flow further from the centre, the rotation Ω is not a constant but is dependent on the radius. It should therefore be written as $\overline{V}_\theta(r)/r$. The modified geostrophic balance can now be resolved with the measurement data available. Figure 35 shows this modified pressure gradient over the extents of the particle using the perturbed tangential velocities 30mm above and 30mm below the sphere. When the perturbed pressure gradient is integrated, one finds the pressure difference distribution over the extents of the sphere. This distribution is depicted in the bottom plot of Figure 35. From the modified pressure distributions above and below the particle we can calculate the resulting force by integrating the pressures over the projected area of the sphere. As we have a discrete dataset, this is done numerically:

$$F_{D,Taylor} = \int_0^{r_p} P(r) 2\pi r dr = \sum_{i=1}^{n} P(r_i) 2\pi r_i \Delta r \tag{5.1}$$

This results in a downwards force of 14.4±3.3 mN (milli Newton). During all calculation and integration steps, the law of propagation of uncertainties (Bertrand-Krajewski et al., 2021) was applied to find the 95% confidence interval of the Taylor column induced drag force.

We can now complete the EOM presented in section 2.3:

$$\left(\rho_p + C_A \rho_f\right) \chi \frac{\partial U_z}{\partial t} = F_{D,Taylor} + F_{D,Skin} + F_{D,Stagnation} + F_B + \rho_f C_A \chi \left(V_r \frac{\partial V_z}{\partial r} \right) \tag{5.2}$$

The buoyance of the sphere is easily calculated using Archimedes law via equation (2.15). Using the particle density of 0.766g/cm^3 and the measured particle volume of 8.402 cm^3, we find a buoyant force of 19.3 ± 0.4 mN. The inertial and advective terms can be estimated using characteristic values found during the experiments. The added mass coefficient C_A is determined 0.5 for a fully submerged particle. The EOM can then be completed:

$$\begin{aligned}
&\left(765 + 0.5 \cdot 10^3\right) 8.402 \cdot 10^{-6} \cdot \frac{0.01}{5} = -\left(14.4 \pm 3.3\right) \cdot 10^{-3} - F_{D,skin} - F_{D,Stagnation} \\
&+ \left(19.33 \pm 0.4\right) E^{-3} + 10^3 \cdot 0.5 \cdot 8.402 \cdot 10^{-6} \left(0.02 \cdot \frac{0.01}{0.1} \right) \Leftrightarrow \\
&F_{D,Skin} + F_{D,Stagnation} = 4.9 \pm 3.7 mN
\end{aligned} \tag{5.3}$$

The inertial and advective terms are respectively two and three orders of magnitude smaller than the buoyant and drag forces and can therefore be neglected. As the Taylor induced drag force is insufficiently large to counteract the buoyant force, the skin friction and stagnation pressure induced forces are expected to be non-zero to close the balance.

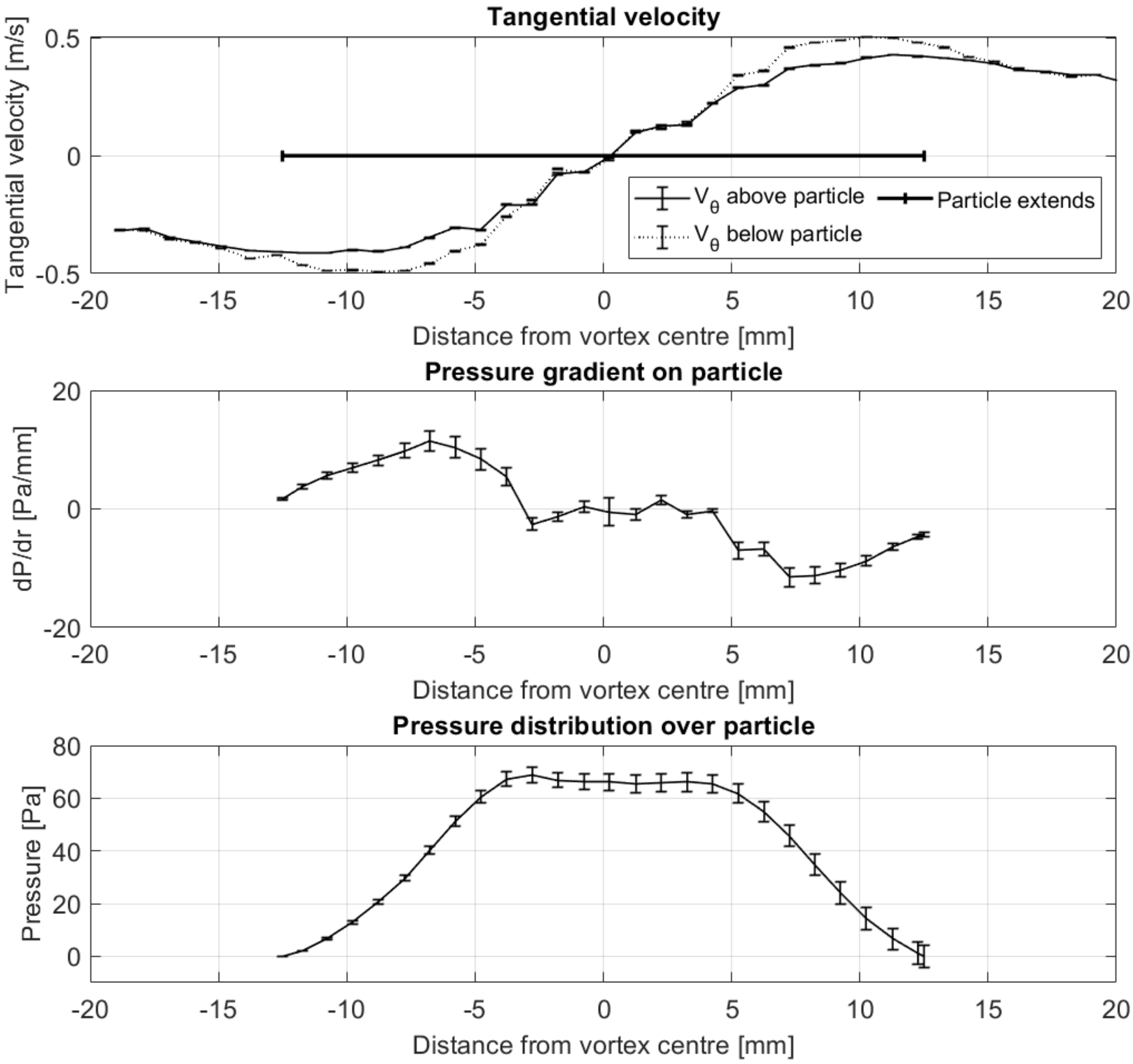

Figure 35 - Top: Tangential velocity profile measured 30 mm above and below the sphere centre. Middle: Pressure gradient determined by the tangential velocity perturbation. Bottom: Pressure distribution over particle resulting from integrating the pressure gradient. Each figure includes the 95% confidence interval.

5.3.2 Drag coefficient by Moore & Saffman I

The drag coefficient introduced in section 2.4.1 by Moore & Saffman (1968) can be tested with our experimental data after applying the correct averaging procedures:

$$C_d = \frac{353}{315}\frac{\Omega^{1\frac{1}{2}} r_p^{\ 2}}{U_p \nu^{\frac{1}{2}}} - \frac{86}{210}\frac{\Omega_\varepsilon^2 r_p^{\ 2}}{U_p^2} = 1.12\frac{\bar{\Omega}^{1\frac{1}{2}} r_p^{\ 2}}{(\bar{U}_p - \bar{V}_z)\nu^{\frac{1}{2}}} - 0.41\frac{\Omega_\varepsilon^2 r_p^{\ 2}}{(\bar{U}_p - \bar{V}_z)^2} \tag{5.4}$$

Moore and Saffman considered a solid body rotation with a constant Ω and we have the angular velocity as a function of the radius. We therefore determined the average rotation over the sphere's projected area. This was done numerically as we have a discrete dataset:

$$\bar{\Omega} = \frac{1}{A_p}\int_0^{r_p} \Omega(r) 2\pi r dr = \frac{2}{r_p^{\ 2}}\sum_{i=1}^{n} \Omega(r_i) r_i \Delta r \tag{5.5}$$

We also require the radially uniform axial velocity profile to determine the slip-velocity $(\bar{U}_p - \bar{V}_z)$. This is defined as the velocity difference (slip) between the radially uniform axial velocity and the particle velocity. The radial uniform axial velocity is determined numerically by:

$$\bar{V}_z = \frac{1}{A_p}\int_0^{r_p} V_z(r) 2\pi r dr = \frac{2}{r_p^{\;2}}\sum_{i=1}^{n} V_z(r_i) r_i \Delta r \qquad (5.6)$$

The average velocity of the experimental particle, $\bar{U}_p$ was determined by averaging all 46 instantaneous particle velocities (obtained by PTV) at the time where the sphere centre crosses the measurement transect:

$$\bar{U}_p = \frac{1}{N}\sum_{i=1}^{n} U_p(t)_i \qquad (5.7)$$
$$t = T_{z=0.29m}$$

The last unknown value for equation (5.4) is the relative rotation of the particle in respect to the rotation of the solid body Ω_ε. In our case this could be rewritten as:

$$\Omega_\varepsilon = \bar{\Omega} - \Omega_p \qquad (5.8)$$

Where Ω_p is the angular velocity of the particle. The PTV software was unfortunately unable to resolve the rotation rate of the particle. Alternatively, an estimate was made by visually reviewing the PTV footage in slow-motion and counting the revolutions manually. A value of approximately 50 rad/s was found. Applying above averaging procedures and filling in formula (5.4) yields a C_d value of 2636. Using this C_d value to determine the drag force via formula (2.25) results in a drag force of 390 mN. This value is twentyfold larger than the buoyant force, making it a significant overestimation.

5.3.3 Drag coefficient by Moore & Saffman II

A simpler formulation of the drag coefficient was proposed by the same authors in a later publication (Moore & Saffman, 1969) which was introduced in section 2.4.2. Using the simplifications proposed in section 5.3.2 we can reformulate the drag coefficient as:

$$C_d = 5.33N = 5.33\frac{2\bar{\Omega} r_p^{\;2}}{(\bar{U}_p - \bar{V}_z)} \qquad (5.9)$$

Using our particle velocity, the radial uniform axial fluid velocity and the angular fluid velocity resolved at the moment the sphere crosses the measurement transect, we find a value for C_d of 280 which results in a drag force of 41.5 mN. This is approximately double the buoyant force, thus still overestimating the drag.

5.3.4 Drag coefficient by Maxworthy

The last formulation of the drag coefficient is the one proposed by Maxworthy (1970) as described in section 2.4.3. It has the same format as the coefficient proposed by Moore & Saffman (1969) but uses a smaller constant:

$$C_d = (2.60 \pm 0.05) N^{1\pm0.01} = (2.6 \pm 0.05)\left(\frac{2\bar{\Omega} r_p^{\;2}}{(\bar{U}_p - \bar{V}_z)}\right)^{1\pm0.01} \qquad (5.10)$$

Completing the formula with our data yields a drag coefficient of 137±3 resulting in a drag force of 20.03±0.04 mN. This is only 4% more than the buoyant force and therefore a very realistic estimate. Duinmeijer (2021) also found reasonable results when applying the Maxworthy drag coefficient.

6 DISCUSSION

The discussion chapter is structured according to the results chapter and discusses the results related to each research question.

6.1 VELOCITY PROFILES IN ABSENCE OF A BUOYANT PARTICLE

The tangential velocity profiles measured by LDV resemble the PIV measurements by Duinmeijer (2020) well. After applying deconvolution, the differences between the velocity profiles reduced even further: 1.5% difference in the magnitude of the peaks and the locations of the peak velocities overlap. This gives confidence in the performance of the deconvolution procedure. We can also compare the LDV tangential velocity results with the theoretical Burgers profile. The difference in maximum tangential velocities of the deconvoluted LDV and the Burgers tangential velocity profile differ only 0.6%, although the location of the maximum tangential velocity (the core radius) is 1mm wider for the Burgers profile. This can possibly be since the Burgers profile is based on an infinite radial domain, whereas we have a tank with boundaries that slow the tangential flow down, moving the profile slightly inwards.

The axial velocity profiles show large differences between the LDV and PIV measurements, including the double peak which is not observed in the PIV measurements. Several reasons were proposed that can explain this difference, for example, the shape of the LDV measurement volume that introduces spatial averaging, altering the shape of the axial velocity profile. To rule out this effect, an alternative transect along the y-axis was performed. In the centre of the vortex, there is still measurement volume smearing, but when one moves half an LDV measurement volume length (0.85mm) away from the centre, the volume smearing is already reduced with approximately 60%. The results of this test still showed the ‘double peak’ profile, ruling out measurement volume smearing as a reason for the differences. Vortex wandering, provided there is a large enough wandering amplitude, has the potential to create an ‘artificial’ peak in the vortex centre. A simple numerical simulation showed that this would require a wandering amplitude of the same magnitude as the core radius. The determined wandering amplitude is however much smaller, making it unlikely that wandering is responsible for the change of the shape. To test the time averaging effect of the vortex wandering even further, moving transects were made which give an indication of the quasi-instantaneous velocity profiles. These moving averages gave an almost equal axial velocity shape as the standard transects, also including the ‘double peak’. They as well confirmed that the wandering amplitude is in the order of 1.2 mm. Moreover, they showed that the magnitude of the maximum axial velocity in the centre is very time dependent: At some moment in time, the axial velocity in the middle of the core can be of a higher magnitude than the second peak around the core radius when at another moment this can be the other way around. A die-contrast experiment gave more confidence in this theory as the same time dependent behaviour of the vortex centre axial velocity was observed. Exclusion of both measurement volume smearing and vortex wandering as causes for the 'double peak profile’ increases our confidence that this is the ‘true’ axial velocity profile.

One other possibility for the large difference between the PIV and LDV data would be that there is a systematic error in the LDV measurement or that the signal processing of the LDV system is faulty. This is however unlikely: The axial and tangential velocities are acquired simultaneously from the same analogue signal and the tangential velocity seems to be in good accordance with the theory and previous experimental data, meaning that the quality of the axial velocity component must also be sufficient.

It is also a possibility that the axial PIV-data from Duinmeijer (2020) is slightly inaccurate (in the close vicinity of the vortex axis for Duinmeijers series 1 and 2). A possible issue during these stereo-PIV measurements could be the accumulation of seeding material in the core of the vortex, leading to the possible rejection of velocity-vectors in the core region. Contour averaging over a larger angular domain was used on the axial flow field then for the azimuthal flow field, as there seems to be a large asymmetry in the axial vector image flow field. This may have led to some smearing of the axial velocity field. Another possible issue when measuring the axial velocities with the stereo-PIV set-up used by Duinmeijer (2020), is the possible projection error when reconstructing the 3D velocity vector from both velocity vectors as measured using the two PIV cameras. This reprojection error on spatial scales in the order of magnitude of the laser sheet thickness. In Duinmeijers (2020) paper the vortex core radius was determined both by measuring the location of the maximum tangential velocity and by determining it via the Burgers model. In Duinmeijers series 1 and series 2 (the smallest hydraulic conditions), a discrepancy exists between the measured value and the theoretical value of the core radius (Duinmeijer et al., 2020, fig. 10). The theoretical value depends on the vertical axial velocity gradient which was derived from the PIV measurements. As it turns out, when this gradient is underestimated, we find an overestimation of the theoretical vortex radius. This is also what Duinmeijer found, indicating that the PIV underestimates the axial velocity values in series one and two. For a better analysis, we should also perform LDV measurements with a stronger hydraulic condition, for example with Duinmeijers series 5 condition where the discrepancy between the theoretical core radius and the measured one is minimal. This was unfortunately not possible due to time limitations but is recommended for follow up research to find closure on the discrepancy between the LDV and PIV axial velocity profiles.

One final remarkable observation in the axial velocity profiles that was seen both during the PIV measurements of Duinmeijer and in this research is the asymmetry of the peaks of the axial profile (see for example Figure 24). No clear explanation was found for this phenomenon yet. The fact that this asymmetry is observed with two completely independent non-intrusive measurement techniques would suggest that there is some secondary flow that causes this asymmetry.

6.2 VELOCITY PROFILES IN PRESENCE OF A BUOYANT PARTICLE

Due to physical limitations of the experimental setup and the dynamic behaviour of the sphere, it is not possible to measure (and average) over long periods of time. This led to relatively fluctuating velocity profiles compared to the velocity profiles without a particle. The obvious solution to overcome this problem would be to repeat these measurements numerous times to obtain more data and converge to a smoother velocity profile. As the computational load of the PTV software is very high, it takes one day to resolve the sphere position for one single point measurement. Given that transect S3D1H1P101V1 consists of 46 individual point measurements, one can imagine the time required to process the full experiment. It was not feasible to repeat the experiment several times given the timeframe of this thesis. Despite the relatively fluctuating velocity profiles, we could still distinguish very interesting features of which the strong tangential velocity difference between the top and bottom of the sphere is the most striking. This velocity difference was predicted by Maxworthy and Moore & Saffman (1970; 1968) for a solid-body rotation but never measured in a free-surface vortex. Another clear observation is the similarity of the velocity profiles measured at different vertical distances from the sphere centre. This suggests that the Taylor-Proudman column spans the whole water column. Maxworthy (1970) suggests that the Taylor column length (he describes it as ‘slug length’) is linearly proportional with the Taylor number given large values of *N* by:

$$L_{TaylorColumn} = \frac{r_p T_a}{17} \tag{6.1}$$

Using some characteristic experimental values leaves us a Taylor column length of about 17 meters. This increases the confidence that the Taylor column spans the whole water column and explains the fact that there is no significant difference between the tangential velocity profiles at different relative vertical distances from the particle centre.

The deconvolution procedure that was used for the velocity profiles in absence of the sphere assumes a fully convoluted signal. As the averaging period of the velocity profiles in presence of the sphere is very short and of the same duration or even shorter than a vortex wandering period, it is not expected that the vortex wandering is fully convoluted into the signal. Moreover, due to the rough shape of the velocity profiles, the Gaussian fitting step in the deconvolution procedure is not as robust as for the smoother velocity profiles in absence of the particle. The error introduced by using the deconvolution is therefore expected to be of the same magnitude as the error that the convolution causes. It was therefore decided not to use it in this part of the research. We should therefore keep in mind that the velocity profiles are slightly steeper, an increase of 3% would be a good estimate which was found to be the increase of the maximum tangential velocities when deconvoluting the velocity profiles in absence of the buoyant sphere.

6.3 TAYLOR COLUMN DRIVEN MOTION

Given the conditions used in this thesis, the Taylor induced drag force found from the modified geostrophic balance accounts for about 75±17% of the total drag force, counteracting the buoyant force. As there is a velocity difference between the radially uniform axial flow velocity and the vertical particle velocity, water must pass around the sphere in a thin viscous layer as the Taylor-column suppresses radial outward motion. Maxworthy (1970) describes this as a thin high velocity sheet of water. It is therefore expected that this causes shear on the particle surface area, especially around the equator of the sphere where the sphere surface is aligned with the flow. A very crude estimation for this value can be found in Appendix E - Skin friction estimation. Moreover, we expect a stagnation pressure induced drag on the particle. The estimation of this term seems however difficult to approximate. Normally one can make an estimate of the form drag by using the relation with the particle-Reynolds number. But due to the strong rotating character of the flow, which possibly suppresses the separation of the flow behind the particle, this relation is unlikely to be correct. This analysis is also outside the scope of the thesis.

It might be the case that the Taylor induced drag has an even larger share of the total drag on the particle than measured. The deconvolution was not applied on the perturbated tangential velocity profiles as they have a short time averaging period of only one second: This is too short to capture the vortex wandering motion thus the deconvolution process is not valid for this case. Measurement volume smearing is however still playing a role and it can therefore be expected that the perturbated tangential velocity profiles are (slightly) larger than measured. This would lead to a higher estimate of the Taylor column induced drag force.

6.4 GENERAL DISCUSSION

The obtained results apply to the specific combination of the experimental particle and the hydraulic conditions used in this thesis. Unfortunately, due to time limitations of this thesis period, no additional conditions were tested. Using different particle shapes could be an additional research parameter and has already been studied by Duinmeijer (2021). In Duinmeijers thesis, three particle shapes were studied: a sphere, a cube and an ellipsoid. Duinmeijer found that using the same flow condition and particle volume and density, the sphere proved the most difficult to transport. Moore and Saffman (1969) proposed that a Taylor column forms around the largest extends of a particle. When considering the three particle shapes with an equal volume, a sphere has the smallest extent, deflects less water and produces the smallest Taylor column leading to less Taylor column induced drag. Another important variable would be the relation of the vortex core radius and the characteristic particle length. The axial vortex flow is radially non-uniform with a peak around the core radius, when the particle radius is smaller than the core radius, the main flow is not pushed in the Ekman layer and generates less tangential velocity difference between the columns above and below the particle, leading to less pressure difference and less downward force. On the other hand, when the particle is much larger than the core radius, the flow might be blocked altogether, leading to no Ekman transport on the particle surface and no Taylor column induced drag. This would also eliminate the free-surface vortex as it needs the axial flow to maintain itself. The relation of the vortex core and the particle characteristic length is important which can be seen in Figure 34. There, the tangential velocity difference becomes significant only in the regions where the maximum axial velocities are observed. In this region, probably more water is pushed into the Ekman layer and more tangential velocity difference is generated accordingly. In this thesis, the particle radius is approximately 50% larger than the core radius and most of the axial flow is thus pushed into the Ekman layer. Therefore, the particle radius being larger than the vortex core radius seems to be a strict criterion for a strong Taylor column induced drag.

7 CONCLUSIONS

The conclusions are structured according to the sub-questions and the results chapter. A final general conclusion answers the main research question.

7.1 VELOCITY PROFILES IN ABSENCE OF A BUOYANT PARTICLE

How are the axial and tangential flow profiles distributed within the vortex core in absence of a solid particle?

The LDV tangential velocity profile obtained during the comparative experiment repeating Duinmeijers flow condition, deviates 5% from the PIV measurements from Duinmeijer. Applying the deconvolution reduces the difference to 1.5%. At this point, the difference is likely in the order of the measurement accuracy of the LDV and PIV. As the differences are marginal, we expect that the deconvolution yields realistic results and works robustly.

The axial LDV velocity profile deviates strongly from the profile measured by Duinmeijer. Duinmeijer proposes that the axial velocity is zero in the vortex centre where experimental data from this research shows the contrary. Several additional experiments indicate that the axial velocity in the vortex centre, while strongly unsteady, is non-zero. While the instantaneous velocity profiles might differ, it is likely that the time averaged axial velocity profile has two local maxima of similar magnitude, one at approximately 60-70% of the core radius and one in the vortex centre.

One-dimensional energy spectra measured at several radii show a sharp increase over the complete frequency bandwidth towards the centre of the vortex. The integral velocity scales also increase towards the centre of the vortex.

7.2 VELOCITY PROFILES IN PRESENCE OF A BUOYANT PARTICLE

How are the axial and tangential flow profiles distributed within the vortex core in presence of a solid particle?

It is possible to determine the tangential and axial velocity profiles at a location relative to the vertical position of the particle centre with the method proposed in this thesis. Due to the short measuring window, the profiles are more susceptible to velocity fluctuations, especially close to the vortex centre. Nevertheless, some distinct features were observed: The maximum tangential velocity below the particle is approximately 25% higher than above it. The tangential velocity difference seems to persist when moving further away from the particle. This suggests that a Taylor-Proudman column extends from the free-surface to the bottom of the tank. The core radius above the particle seems to be larger than the core radius below the particle. Furthermore, the core radius in presence of a particle is generally larger than the core radius in absence of a particle. The axial flow profile also follows the ‘double peak’ profile with the maximum velocities concentrating more towards the outer peak underneath the particle.

7.3 TAYLOR COLUMN DRIVEN MOTION

How do the altered velocity profiles contribute to the drag force on the buoyant particles?

With the experimental set-up, hydraulic condition and particle used in this thesis, the Taylor-column induced drag force accounts for 75 ± 17% of the total drag force. It can be assumed that skin friction and stagnation pressure induced drag also have a contribution to the downward force as there is a measured vertical velocity difference between the sphere and the radially uniform axial velocity. Moreover, as deconvolution was not applied in these calculations, it is reasonable to assume that the Taylor column induced drag force is (slightly) larger as the perturbed tangential velocity profiles are in fact slightly underestimated as vortex wandering and measurement volume smearing have the tendency to flatten the tangential velocity profile.

The drag coefficient proposed by Moore and Saffman (1968) seems to overpredict the drag on the particle significantly (1900%). The second drag coefficient proposed by Moore and Saffman (1969) still overpredicts the drag by approximately 100%. Finally, the drag coefficient by Maxworthy (1970) gives a very accurate estimation of the drag on the particle with a value only 4% higher than the buoyant force. It therefore seems possible to extend the use of the Maxworthy drag coefficient from pure solid body rotating flow to use in free-surface vortices, given large Taylor numbers $T_a \gg 1$ and low Rossby numbers $R_o \ll 1$ and a particle radius of approximately 150% of the core radius.

7.4 GENERAL CONCLUSION

How does a Taylor-Proudman column contribute to the downward transport of buoyant particles in a free-surface vortex core?

The presence of a buoyant sphere in a free-surface vortex core leads to a significant tangential velocity difference above and below the particle provided the Taylor number is large $T_a \gg 1$, the Rossby number is low $R_o \ll 1$ and the particle radius is slightly larger than the vortex core radius. This leads to a pressure perturbation via the modified geostrophic balance. A higher relative pressure above and a lower relative pressure below the particle is the result. This pressure difference over the particle induces a downward force. Depending on the particle density and thus buoyancy, this Taylor column induced force can be sufficient to lead to downward transport of the particle.

8 RECOMMENDATIONS

1. An often-made suggestion was to convert the experimental set-up to a gravity driven constant head system to avoid fluctuations induced by the water pump and PID control system. Moving the pump from the base of the vortex tank to a stand-alone location would also benefit the stability of the measurements as it reduces high frequency vibrations that have the potential to create noise in the optical measurements.
2. Another way to more accurately measure pressure perturbation would be to design a sphere with a stable orientation in the vortex core equipped with pressure transducers on the top and bottom. This could be an interesting follow-up study.
3. It is recommended to perform more simultaneous PTV LDV measurements. Now each point on the transect is measured only once. More measurements would lead to a more robust perturbated tangential velocity profile. The author still has a full transect on the shelve but processing it would take another month. It would be recommended to still process this data and append it at a later moment.
4. Optimizing the PTV software code for GPU processing would lead to a significant decrease in processing time/cost as GPU computation is orders of magnitude quicker with bulky matrix calculations/ transformations than classical CPU processing.
5. The deconvolution procedure proposed in this thesis uses Gaussian fitting as a step to transform the velocity profiles. This fitting procedure requires sufficiently smooth velocity profiles for robust operation. It was found that it is less suitable for the velocity profiles in presence of the sphere as the averaging periods are too short. It is recommended to investigate other deconvolution procedures that omit this step while providing reliable results.
6. It is highly recommended to investigate the influence of the vortex core radius/particle size ratio on the Taylor column induced drag as is described in the general discussion as it seems that this ratio has a large influence on the magnitude of the Taylor column induced particle drag.

REFERENCES

Andersen, A., Bohr, T., Stenum, B., Rasmussen, J. J., & Lautrup, B. (2003). Anatomy of a Bathtub Vortex. *Physical Review Letters*, *91*(10), 104502. https://doi.org/10.1103/PhysRevLett.91.104502

Bertrand-Krajewski, J.-L., Clemens-Meyer, F., & Lepot, M. (Eds.). (2021). *Metrology in Urban Drainage and Stormwater Management: Plug and Pray*. IWA Publishing. https://doi.org/10.2166/9781789060119

Burgers, J. M. (1948). A Mathematical Model Illustrating the Theory of Turbulence. In R. Von Mises & T. Von Kármán (Eds.), *Advances in Applied Mechanics* (Vol. 1, pp. 171–199). Elsevier. https://doi.org/10.1016/S0065-2156(08)70100-5

Devenport, W. J., Rife, M. C., Liapis, S. I., & Follin, G. J. (1996). The structure and development of a wing-tip vortex. *Journal of Fluid Mechanics*, *312*, 67–106. https://doi.org/10.1017/S0022112096001929

Drain, L. E. (1980). *The Laser Doppler Technique*. J. Wiley. https://books.google.nl/books?id=-EPxAAAAMAAJ

Duinmeijer, S. P. A. (2020). *On the free-surface vortex driven motion of buoyant particles* [Doctoral thesis, Delft University of Technology]. https://doi.org/10.4233/uuid:a33fa2a9-f347-40a3-96be-51e880018974

Duinmeijer, S. P. A., & Clemens, F. H. L. R. (2021). An experimental study on the motion of buoyant particles in the free-surface vortex flow. *Journal of Hydraulic Research*, *59*(6), 947–962. https://doi.org/10.1080/00221686.2020.1845827

Duinmeijer, S. P. A., Oldenziel, G., & Clemens, F. H. L. R. (2020). Experimental study on the 3D-flow field of a free-surface vortex using stereo PIV. *Journal of Hydraulic Research*, *58*(1), 105–119. https://doi.org/10.1080/00221686.2018.1555558

Durst, F., Melling, A., Whitelaw, J. H., & Wang, C. P. (1976). *Principles and practice of laser-Doppler anemometry*.

Maxworthy, T. (1970). The flow created by a sphere moving along the axis of a rotating, slightly-viscous fluid. *Journal of Fluid Mechanics*, *40*(3), 453–479. https://doi.org/10.1017/S0022112070000265

Mie, G. (1908). Beiträge zur Optik trüber Medien, speziell kolloidaler Metallösungen. *Annalen Der Physik*, *330*(3), 377–445. https://doi.org/10.1002/andp.19083300302

Moore, D. W., & Saffman, P. G. (1968). The rise of a body through a rotating fluid in a container of finite length. *Journal of Fluid Mechanics*, *31*(4), 635–642. https://doi.org/10.1017/S0022112068000376

Moore, D. W., & Saffman, P. G. (1969). The Structure of Free Vertical Shear Layers in a Rotating Fluid and the Motion Produced by a Slowly Rising Body. *Philosophical Transactions of the Royal Society of London. Series A, Mathematical and Physical Sciences*, *264*(1156), 597–634. JSTOR.

Mulligan, S., De Cesare, G., Casserly, J., & Sherlock, R. (2018). Understanding turbulent free-surface vortex flows using a Taylor-Couette flow analogy. *Scientific Reports*, *8*(1), 824. https://doi.org/10.1038/s41598-017-16950-w

Nieuwstadt, F., Boersma, B. J., & Westerweel, J. (2016). *Turbulence: Introduction to Theory and Applications of Turbulent Flows*. Springer. https://doi.org/10.1007/978-3-319-31599-7

Pasche, S., Gallaire, F., Dreyer, M., & Farhat, M. (2014). Obstacle-induced spiral vortex breakdown. *Experiments in Fluids*, *55*. https://doi.org/10.1007/s00348-014-1784-7

Rankine, W. J. M., & Millar, W. J. (1921). *A manual of applied mechanics.* C. Griffin and company, limited. //catalog.hathitrust.org/Record/002014037

Taylor, G. I. (1922). The motion of a sphere in a rotating liquid. *Proceedings of the Royal Society of London. Series A, Containing Papers of a Mathematical and Physical Character*, *102*(715), 180–189. https://doi.org/10.1098/rspa.1922.0079

Voßwinkel, N. (2017). *Transportvermögen von Einlaufwirbeln* (Band 21) [Bergische Universität Wuppertal]. Shaker Verlag GmbH Germany.

Wada, Y., Furuichi, N., & Tsuji, Y. (2022). Correction method of measurement volume effects on time-averaged statistics for laser Doppler velocimetry. *European Journal of Mechanics - B/Fluids*, *91*, 233–243. https://doi.org/10.1016/j.euromechflu.2021.10.007

ACKNOWLEDGEMENTS

I could not have finished this thesis on my own, therefore there are some people that I would like to thank:

First, I would like to thank Wout Bakker, my daily supervisor at Deltares, for helping me get acquainted with the optical measuring equipment, for the support throughout the thesis and the Westmalle's on Thursday evenings. I would like to thank François Clemens for developing the PTV system and the support throughout the way. Thanks goes to Alex Duinmeijer for his critical thinking on the topic, he warned me that during his PhD thesis he opened Pandoras Box on this topic and I am very sure that I didn't close it. Thanks to Bas Hofland and Wim Uijttewaal from the TU Delft for their good advice and steering during our meetings. Bas his advice to "Stick to the planning rather than adjusting the planning to the research" proved very useful. I would also like to thank Gosse Oldenziel for his expert advice and many ideas, unfortunately I didn't have enough time to try them all. Then, I would like to thank the Experimental Facility Support department from Deltares for providing and helping me with the experimental equipment and especially Danko Boonstra and Wim Taal for setting up the discharge control system. Finally, a big thanks to Viktorija for being there at the other side of the often very blurry work/life balance and the patience as the thesis took 'just a bit' longer than I foresaw.

THESIS COMMITTEE

The thesis committee consists of the following persons:

Committee chair TU Delft	**Dr. Ir. B. Hofland**	**TU Delft (Coastal Structures)**
Committee member TU Delft	**Prof. Dr. Ir. W.S.J. Uijttewaal**	**TU Delft (Env. fluid mechanics)**
Day-to-day supervisor	**Ir. W. Bakker**	**Deltares (HYE)**
Advisor	**Prof. Dr. Ir. F.H.L.R. Clemens**	**Deltares (HYE) / TU Delft**
External advisor	**Dr. Ir. S.P.A. Duinmeijer**	**Municipality of Rotterdam**

The above-mentioned people where are not arbitrarily selected:

Bas Hofland was asked to chair the committee as he is a lecturer at the TU Delft and has experience with flow measuring methods and has enthusiasm in developing new experimental techniques.

Wim Uijttewaal is expert on the field of turbulence and is a TU Delft professor in fluid mechanics. He also has experience with flow measurement techniques. His advice during the thesis period was very useful.

Wout Bakker is also sharing the enthusiasm of pushing flow measurement techniques to the next level. His area of expertise is flow measuring with PIV and PTV and has extended experience with optics that proved very useful during the research.

Francois Clemens has great affinity with metrology (the science of measuring) and is always full of ideas. His advice on this thesis was very welcome.

Alex Duinmeijer recently published his PhD thesis on the topic of free-surface vortex driven motion of buoyant particles and made his experimental set-up available for this research. He has loads of experience with the topic and it was a pleasure having him in the committee.

APPENDICES

Table of contents

Appendix A - Detailed drawing of experimental set-up

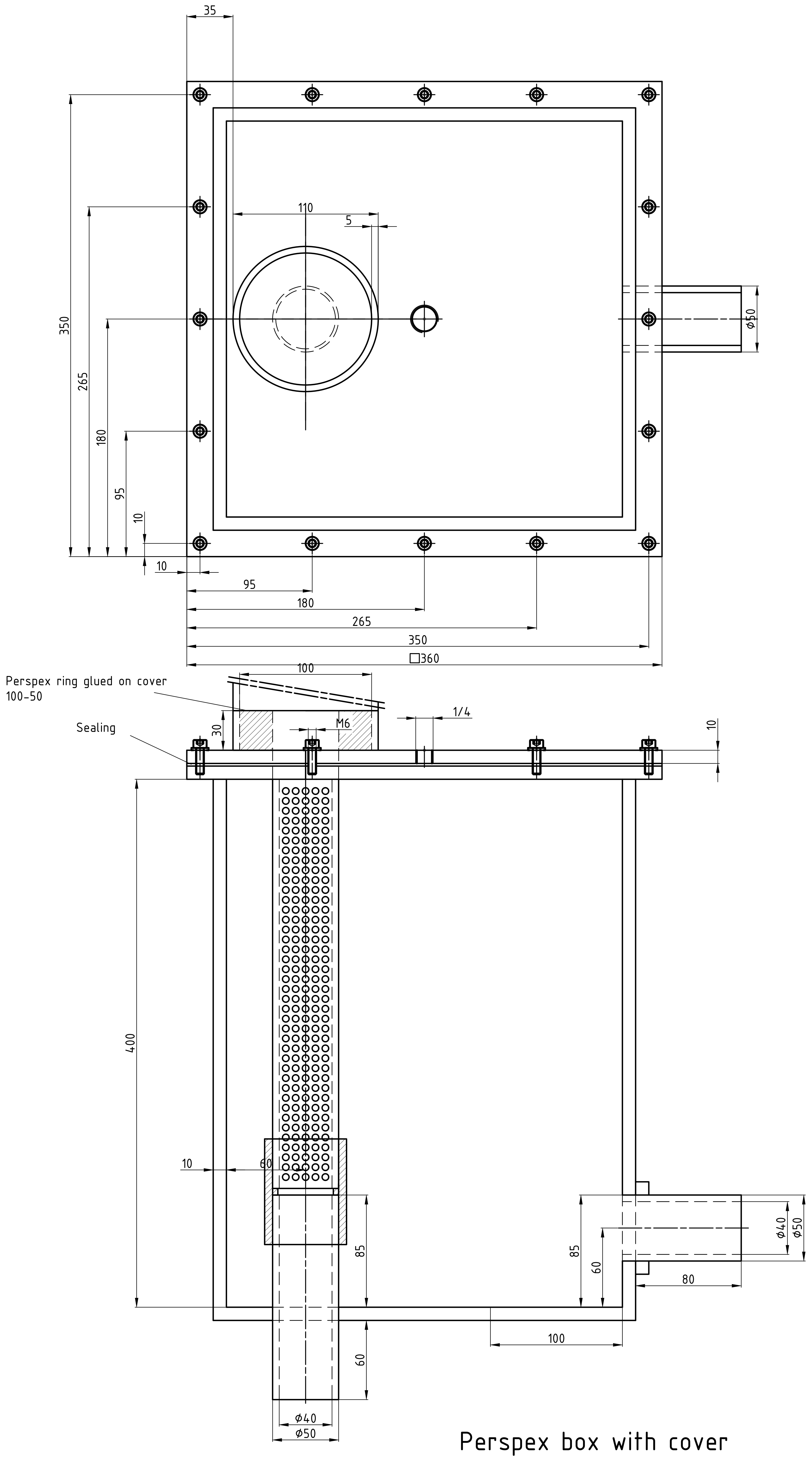

Perspex box with cover

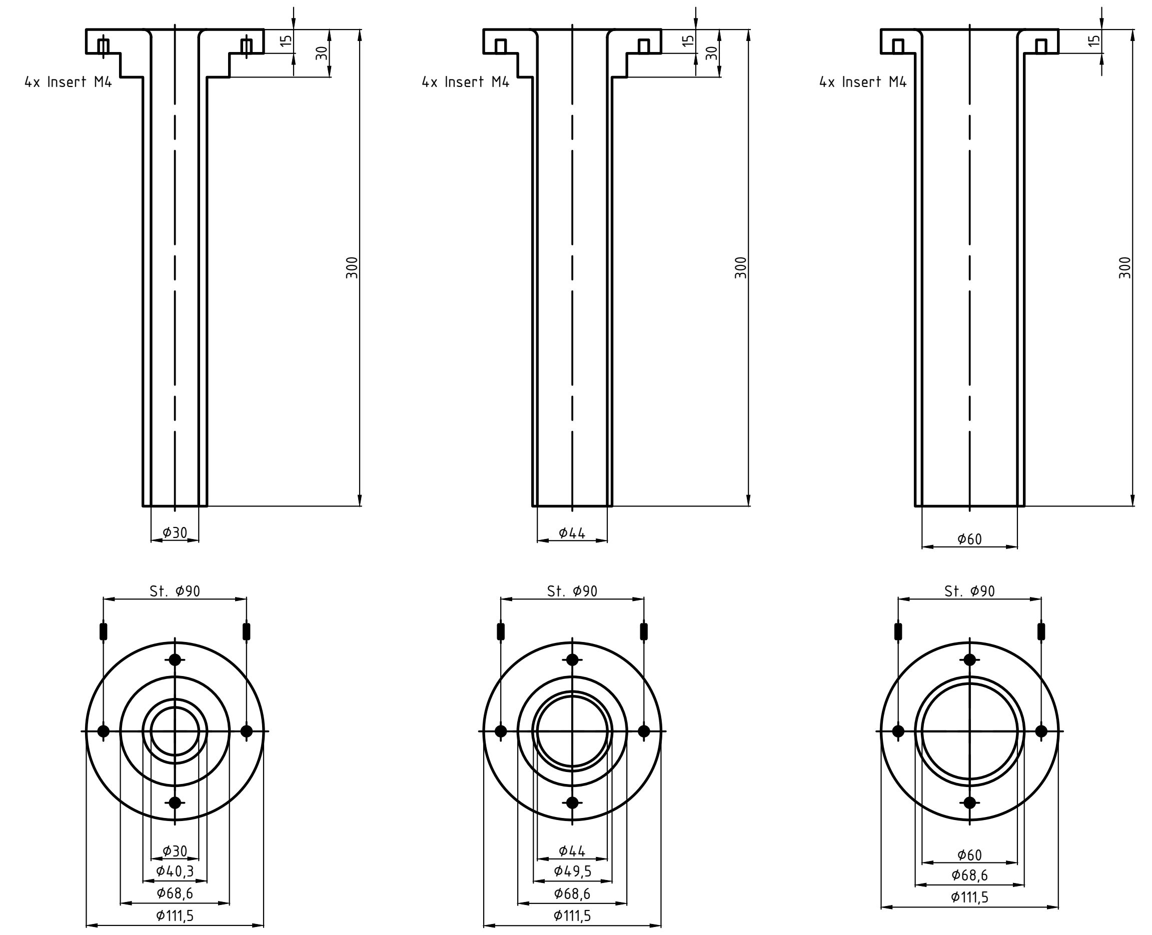

Drawingno: 1		Material: Perspex	
Filename: Vorotx_separator_tank.dwg		Projectname: 1230295	
Title: Separtion tank		American Projection, All dim. in mm	Sheet 1 / 1
Deltares Enabling Delta Life	Drawn: C.van Nieuwenhuizen	Scale: 1 : 3	A2
	Checked: A. Duinmeijer	Date: 29-05-2017	
	Approved: A. Duinmeijer	Project: 1230295	

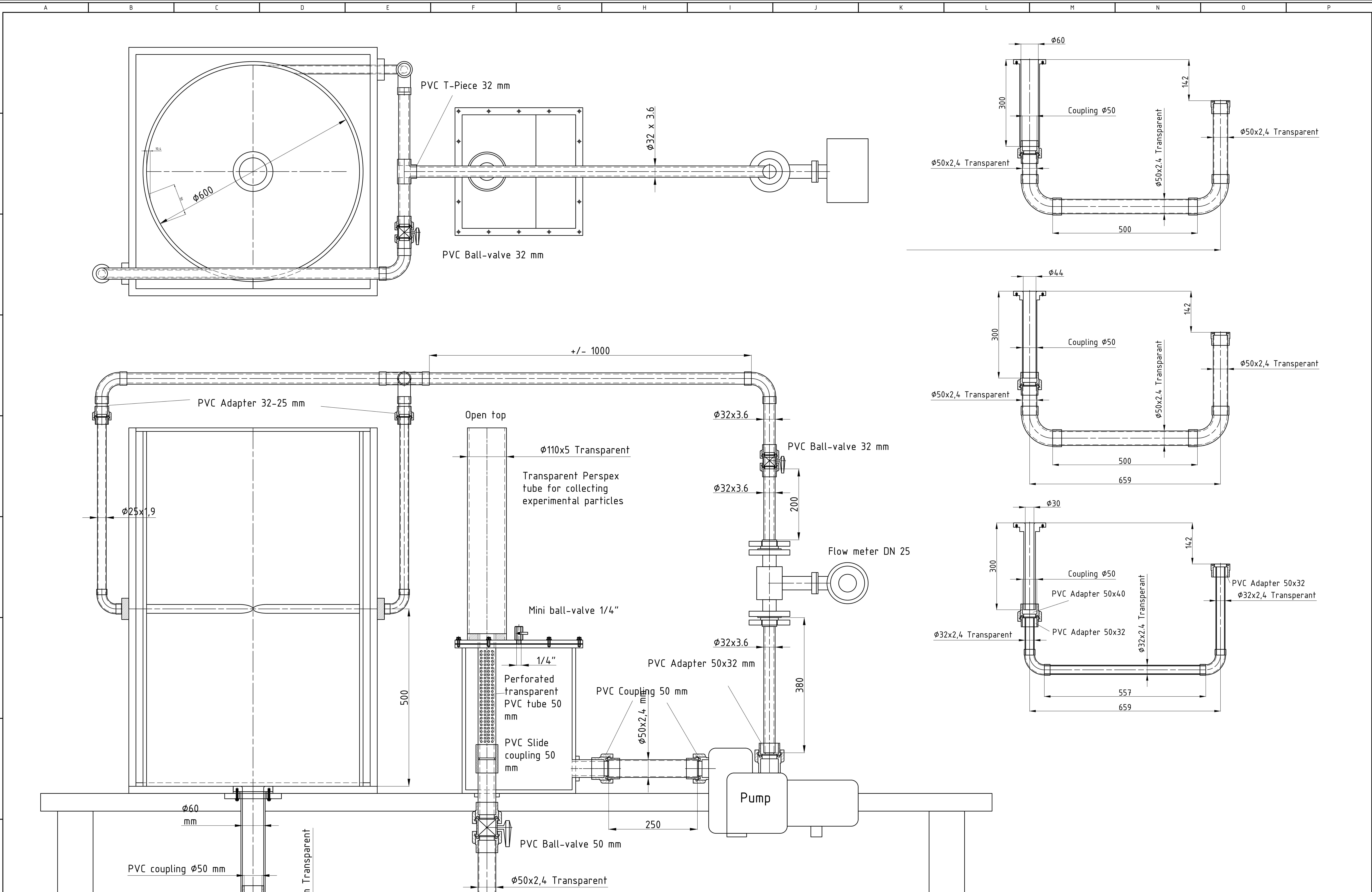

1	29-05-2017	Revison of particle separator	C.van Nieuwenhuizen
Revise	Revisedate	Description:	Name:
Drawingno: 1		Material: Perspex / PVC	
Filename: Transport_Vortex.dwg		Projectname: Vortex transport	
Title: Set-up vortex generator		American Projection / All dim. in mm	Sheet 1 / 1
Deltares Enabling Delta Life	Drawn: C. van Nieuwenhuizen	Scale: 1 : 5	
	Checked: A. Duinmeijer	Date: 28-05-2017	A2
	Approved: A. Duinmeijer	Project: 1230295	

Appendix B - LDV beam diameter calibration

This figure shows the original calibration curve of the beam intensity as a function of the position in the beam of the LDV used in this thesis.

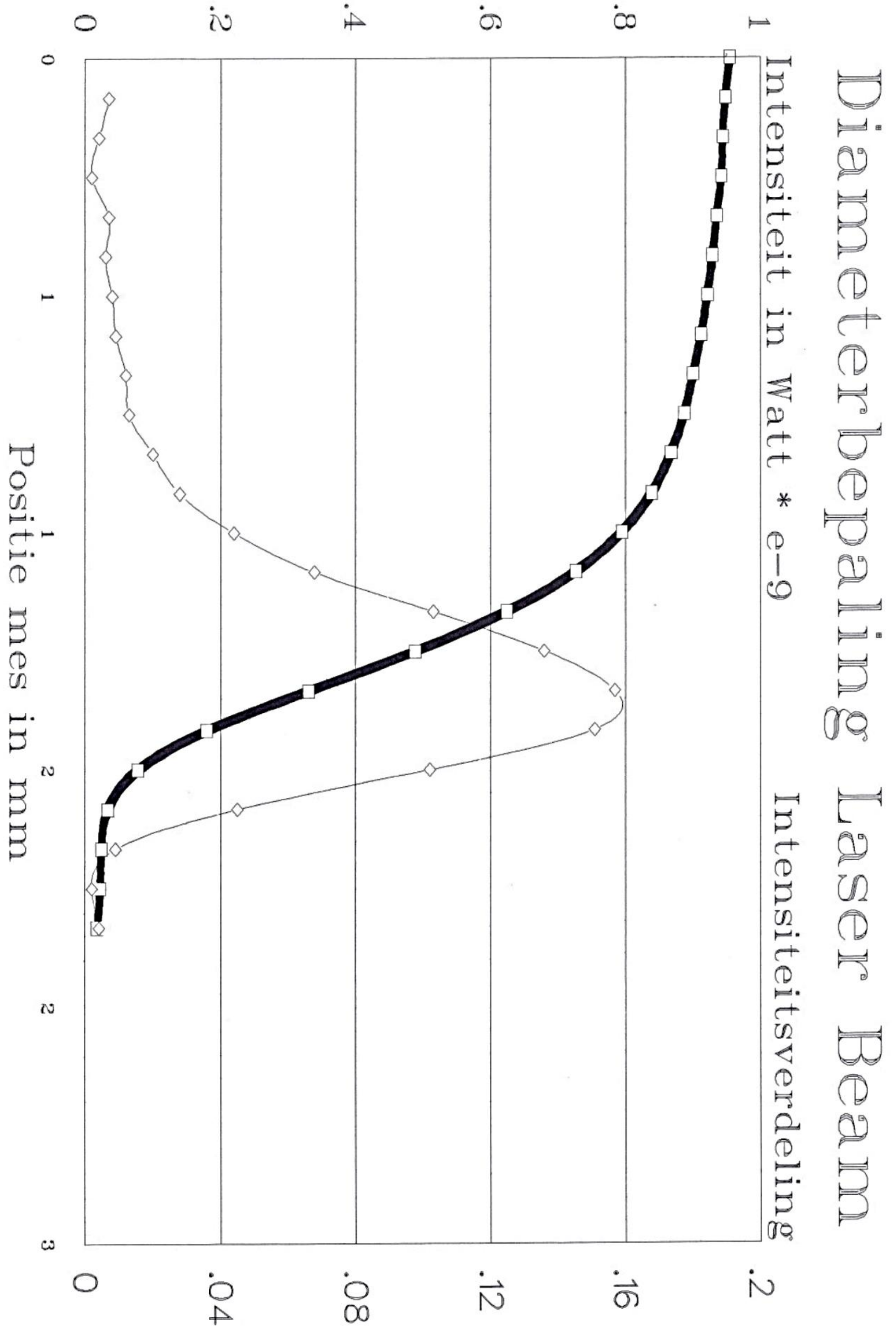

Appendix C - LDV position calibration

The figure below should be used aside the MATLAB script on the next page, as a clarification of the distances and angles.

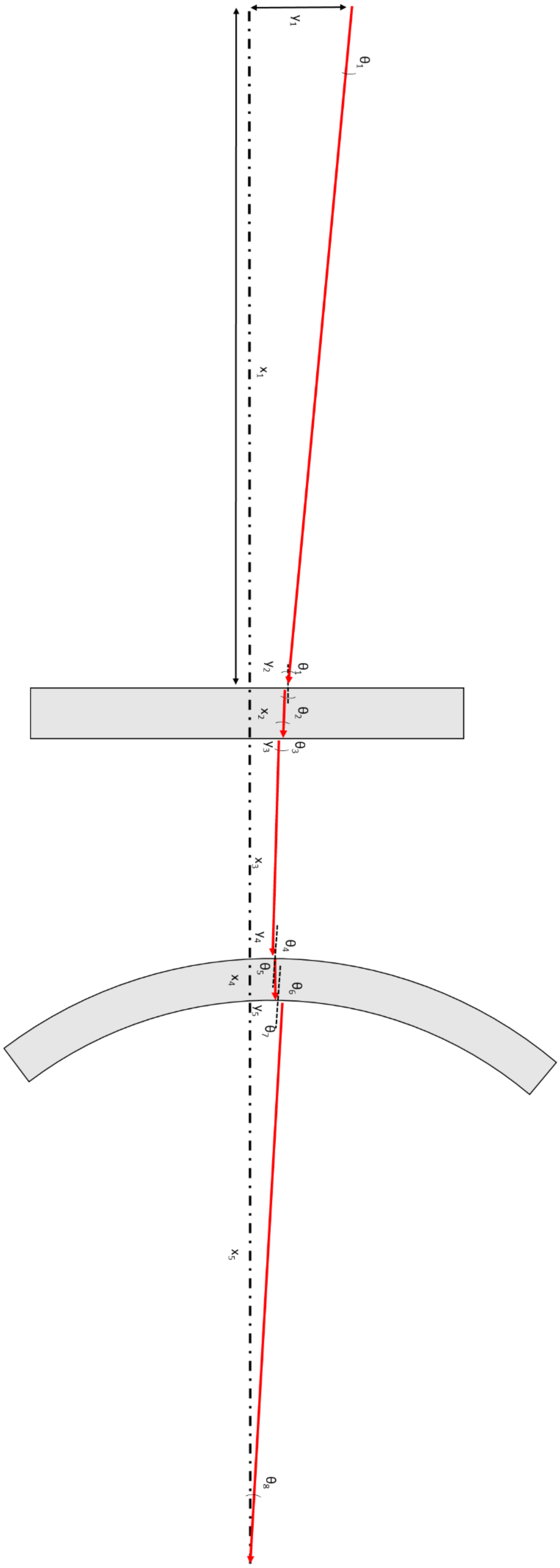

y1
θ1
x1
y2
θ1
θ2
x2
y3
θ3
x3
y4
θ4
θ5
x4
θ6
y5
θ7
x5
θ8

```
close all
clear
clc

%LDA Ray Tracing through core

%% Declare variables
% Breaking indices
n_water = 1.3319;
n_pmma  = 1.4889;
n_air   = 1.0003;


% Tank dimensions
R_in     = 304.91;    %inner radius [mm]
R_out    = 312.88;    %outer radius [mm]
T_out    = 19.29;     %thickness outer acrylate wall [mm]
T_in     = 7.97;      %thickness inner acrylate wall [mm]
L_ib     = 17.55;     %spacing between outer and inner wall [mm]
a1       = 3.5885;    %angle between reference beams and normal [deg.]

%% Calculation
X    = linspace(141,400,50);
A=zeros(length(X),15);
%
for i = 1:length(X)

y1   = 400*tand(a1);
y2   = y1*(400-X(i))/400;
a2   = asind(sind(a1)*n_air/n_pmma);
y3   = y2-tand(a2)*T_out;
a3   = asind(sind(a2)*n_pmma/n_water);
y4  = y3-tand(a3)*L_ib;
x3   = L_ib+(1-cos(asin(y4/R_out)))*R_out;
a4   = a3-asind(y4/R_out);
a5   = asind(sind(a4)*n_water/n_pmma);
y5   = y4-tand(a3-a4+a5)*T_in;
a6   = a3-a4+a5-asind(y5/R_in);
a7   = asind(sind(a6)*n_pmma/n_water);
a8   = asind(y5/R_in)+a7;
x5   = 304.25-((1-cos(asin(y5/R_in)))*R_in+y5/tand(a8));

A(i,1)  = X(i);
A(i,2)  = x3;
A(i,3)  = x5;
A(i,4)  = y1;
A(i,5)  = y2;
A(i,6)  = y3;
A(i,7)  = y4;
A(i,8)  = y5;
A(i,9)  = a2;
A(i,10)  = a3;
A(i,11)  = a4;
A(i,12)  = a5;
A(i,13)  = a6;
A(i,14)  = a7;
A(i,15)  = a8;
end

fit1=fit(A(:,3),X','poly1');
D=coeffvalues(fit1);
```

```
text1 = ['Linear fit: ',num2str(D(1)),'X '];

%% Plot and fit
g = figure;
g.Position = [100 100 700 500];
plot(A(:,3),X,'ok','linewidth',1);
hold on
plot(fit1,'k');
title('LDA Traversing Calibration','fontsize', 14);
xlabel('Traversing distance measurement point','fontsize', 14);
ylabel('Traversing distance laser','fontsize', 14);
set(gca, 'fontsize', 14);
set(gca, 'GridColor',[0 0 0]);
set(gca, 'GridAlpha',0.3);
grid on;
legend('Theoretical profile','Fit','Location','se');
xlim([0 350]);
ylim([100 400]);
```

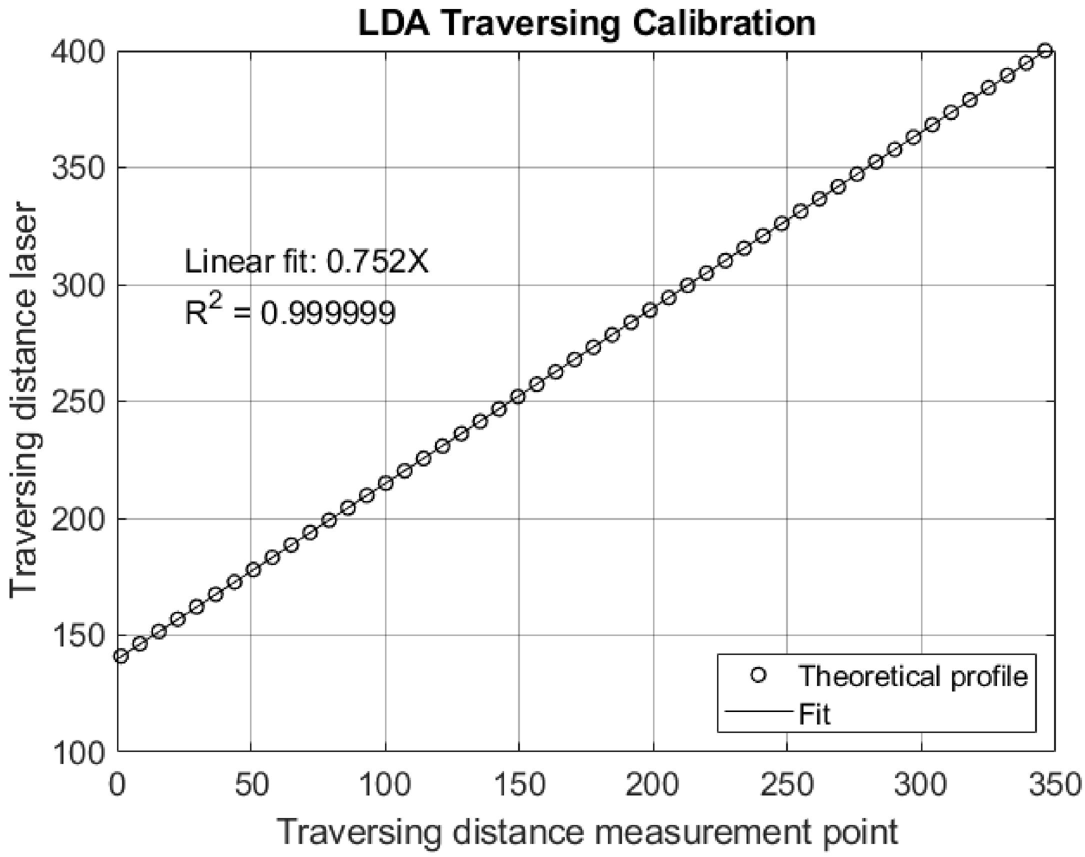

Appendix D - LDV traverse position calibration

LDA traverseer		mVolt		mVolt avg	dx	dv	mv/mm
170	747	745	756	749.33	10		
160	835	834	834	834.33	10	85.00	8.50
150	926	924	924	924.67	10	90.33	9.03
140	1016	1015	1015	1015.33	10	90.67	9.07
130	1107	1106	1106	1106.33	10	91.00	9.10
120	1198	1197	1197	1197.33	10	91.00	9.10
110	1289	1288	1288	1288.33	10	91.00	9.10
100	1380	1379	1379	1379.33	10	91.00	9.10
90	1475	1475	1474	1474.67	10	95.33	9.53
80	1569	1568	1568	1568.33	10	93.67	9.37
70	1661	1661	1661	1661.00	10	92.67	9.27
60	1752	1752	1752	1752.00	10	91.00	9.10
50	1844	1844	1844	1844.00	10	92.00	9.20
40	1936	1936	1936	1936.00	10	92.00	9.20
30	2028	2028	2028	2028.00	10	92.00	9.20
20	2122	2121	2121	2121.33	10	93.33	9.33
10	2213	2213	2213	2213.00	10	91.67	9.17
0	2304	2304	2304	2304.00	10	91.00	9.10
-10	2397	2397	2397	2397.00	10	93.00	9.30
-20	2490	2489	2489	2489.33	10	92.33	9.23
-30	2582	2582	2582	2582.00	10	92.67	9.27
-40	2675	2675	2675	2675.00	10	93.00	9.30
-50	2768	2767	2767	2767.33	10	92.33	9.23
-60	2859	2859	2859	2859.00	10	91.67	9.17
-70	2951	2951	2951	2951.00	10	92.00	9.20
-80	3043	3043	3043	3043.00	10	92.00	9.20
-90	3136	3136	3136	3136.00	10	93.00	9.30
-100	3227	3227	3226	3226.67	10	90.67	9.07

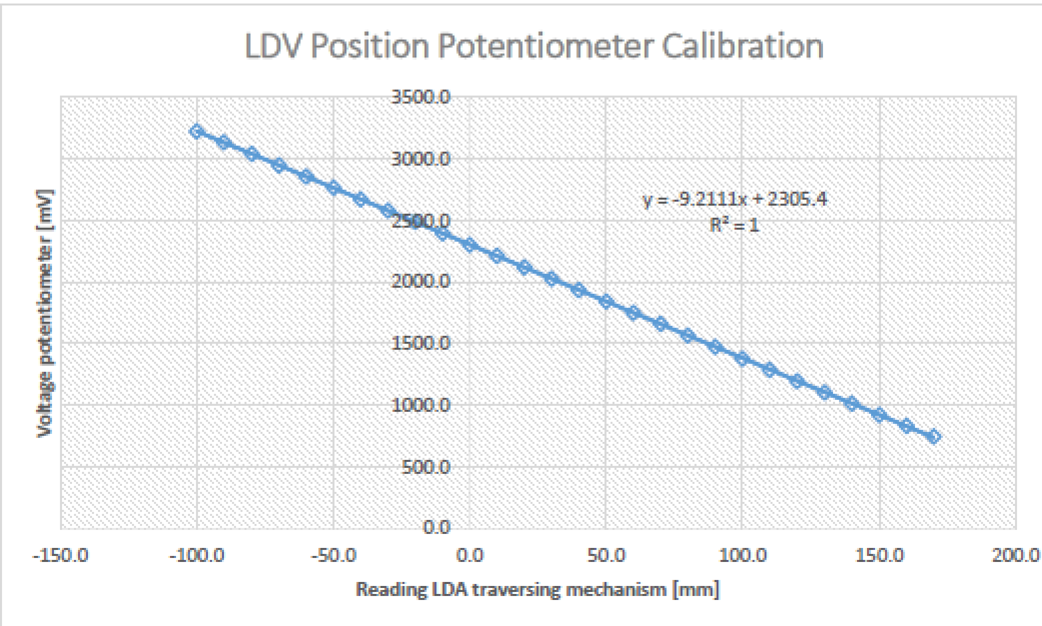

Appendix E - Skin friction estimation

A very crude estimation can be made of the skin friction by assuming that half the surface area of the sphere is aligned with the flow and contributes to the skin drag. Furthermore, we assume that the radial uniform flow in the Taylor column will be forced through a small sheet present on the particle surface

$$F_{D,Skin} = \tau \frac{A_{surface}}{2} \approx \mu \frac{\partial\left(\bar{U}_z - \bar{V}_z\right)}{\partial r} 2\pi r_p{}^2 \approx \mu \frac{\frac{A_1}{A_2}\left(\bar{U}_z - \bar{V}_z\right)}{\partial r} 2\pi r_p{}^2 \approx \frac{\mu r_p{}^4 \pi\left(\bar{U}_z - \bar{V}_z\right)}{r_p\delta^2 + \delta^3}$$

Using characteristic values from the experiments and assuming a boundary layer thickness δ of 0.5mm we find a skin friction of 1 mN.